FABRICATION AND CHARACTERIZATION OF POLYVINYLPYRROLIDONE AND POLYACRYLONITRILE ELECTROSPUN NANOCOMPOSITE FIBERS

A Dissertation by

Waseem Sabir Khan

Master of Science, Wichita State University, 2003

Bachelor of Engineering, NED University of Engineering and Technology, Pakistan, 1988

Submitted to the Department of Mechanical Engineering
and the faculty of the Graduate School of
Wichita State University
in partial fulfillment of
the requirements for the degree of
Doctor of Philosophy

December 2010

FABRICATION AND CHARACTERIZATION OF POLYVINYLPYRROLIDONE AND POLYACRYLONITRILE ELECTROSPUN NANOCOMPOSITE FIBERS

The following faculty have examined the final copy of this dissertation for form and content, and recommend that it be accepted in partial fulfillment of the requirement for the Doctor of Philosophy with a major in Mechanical Engineering.

_____
Ramazan Asmatulu, Committee Chair

_____
Hamid Lankarani, Committee Member

_____
Ikram Ahmed, Committee Member

_____
Bayram Yildirim, Committee Member

_____
Gamal Weheba, Committee Member

Accepted for the College of Engineering

_____
Zulma Toro-Ramos, Dean

Accepted for the Graduate School

_____
J. David McDonald, Dean

DEDICATION

To my mother, Mrs. Fehmida Khatoon, for her unending love, patience, and understanding, without which I could not have achieved this goal—she will always live in my heart

Success is the ability to go from one failure to another with no loss of enthusiasm.

ACKNOWLEDGEMENTS

I would like to express his sincere appreciation to my advisor, Dr. Ramazan Asmatulu, for his guidance, inspiration, suggestions, criticism, and financial support throughout this investigation. Special thanks are given to my committee members—Dr. Hamid Lankarani, Dr. Ikram Ahmed, Dr. Bayram Yildirim, and Dr. Gamal Weheba. I also thank Dr. H. Hamdeh and Dr. J. Ho for their guidance and help in carrying out Mössbauer spectroscopy and other magnetic tests and analyses.

I acknowledge Mr. Chaminda, Dr. M.M. El-Tabey, and Mr. Pravi for my training and helping me carry out experiments. I wish to thank my colleagues Shifath Ikram Khan, Heath Misak, Rajib Anwer, and Jananisri Gopu for teaching and training me during these studies.

Finally, I acknowledge my mother, sisters, and brother for their continuous support and encouragement.

ABSTRACT

Electrospun nanocomposite fibers were produced using polyvinylpyrrolidone (PVP), polyacrylonitrile (PAN), multiwall carbon nanotubes (MWCNTs), and $Ni_{0.6}Zn_{0.4}Fe_2O_4$ (NiZn ferrites) nanoparticles, and their physical properties, such as electrical, dielectrical, thermal, acoustic, and magnetic were determined. In this dissertation, various system parameters (e.g., polymers, solvents, and viscosity) and process parameters (e.g., electrical potential, pump speed, concentration, and distance) of the electrospinning process were studied in order to obtain the optimum properties of the nanocomposite fibers. MWCNTs are conductors, and NiZn-ferrite nanoparticles are semi-conductor materials; therefore, they alter the physical properties of electrospun fibers in a different way. A comparison was made between MWCNT-based fibers and NiZn ferrite-based fibers in terms of physical properties. As far as magnetic properties are concerned, only NiZn ferrite-based fibers have been used because MWCNT-based fibers do not exhibit magnetic properties. This dissertation determined to what extent the physical properties change when nanoscale inclusions are encapsulated in nanocomposite fibers.

This study may open up new possibilities of using these products in various industrial applications (e.g., filtration and separation, high frequency antennas, magnetic storage, environmental sensors, biosensors, etc.) in the near future.

TABLE OF CONTENTS

TABLE OF CONTENTS (continued)

TABLE OF CONTENTS (continued)

TABLE OF CONTENTS (continued)

Chapter Page

LIST OF TABLES

LIST OF FIGURES

LIST OF FIGURES (continued)

LIST OF FIGURES (continued)

LIST OF FIGURES (Continued)

LIST OF FIGURES (Continued)

LIST OF FIGURES (Continued)

LIST OF ABBREVATIONS

AFM	Atomic Force Microscopy
BPF	Blade Passage Frequency
CNT	Carbon Nanotube
DMAc	Dimethylacetamide
DMF	Dimethylformamide
DSC	Differential Scanning Calorimetry
EMF	Electromagnetic Field
FAA	Federal Aviation Administration
FC	Field-Cooled (Field-Cooling)
HMF	Hyperfine Magnetic Field
IS	Isomer Shift
MWCNT	Multiwall Carbon Nanotube
PAN	Polyacrylonitrile
PEEK	Polyetherether Ketone
PS	Polystyrene
PVP	Polyvinylpyrrolidone
QS	Quadrupole Splitting
SEM	Scanning Electron Microscopy
SIL	Speech Interference Level
SPL	Sound Pressure Level
SQUID	Superconducting Quantum Interface Device
SWCNT	Single-Wall Carbon Nanotube

VSM	Vibrating Sample Magnetometer
ZFC	Zero-Field-Cooled

LISTS OF SYMBOLS

r	radius of the meniscus
ε	permittivity
V	applied voltage, applied field, electrical field
H	distance between capillary and collector screen
V_C	critical voltage
e	point charge
F	force, average electric field
dv_x/d_y	rate of shear
k	consistency index,
K	thermal conductivity
n	flow behaivor index
$d\gamma/dt$	rate of strain
v	average jet velocity
R	radius of jet, Boltzmann's constant
R	recoil effect
m	mass index
ω	surface charge density
ρ	hydrostatic pressure, resistivity, density
γ	surface tension coefficient
ε_0	dielectric permeability of vacuum
Q	volume flow rate
σ_e	electrical conductivity

I	current, distance between two charges
R_0	radius of capillary tube
W_e	weber number
R_e	Reynolds number
α	a constant
t	time
G	elastic modulus
μ	viscoelastic modulus
β	cross-sectional radius of the filament
η	viscosity of polymeric solution
d	diameter of fiber, specimen thickness
L	length of capillary tube
u	drift velocity, velocity of elastic wave
μ_i	mobility of charge carrier
E	electric field
q	stored charge, field gradient
C_o	vacuum capacitance per unit area
P	polarization
dv	elemental volume
c	capacitance, velocity of light
D	electric displacement
ϵ_r	dielectric constant

E_L	local field
E_C	field due to real charge on the electrode
ΣE_D	sum of field
N	concentration of molecules
α_T	total polarization
α_e	electronic polarization
α_a	atomic polarization
α_0	dipole polarization
μ_t	mobility at temperature T (^{0}K)
E_μ	activation energy
μ_0	temperature independent constant
T_g	glass transition temperature
n_i	density of charge carrier
K_ρ	ionic conductivity
K_0	constant
J	current density
τ_i	relaxation time
ρ_0	temperature independent constant
q_x	heat flux
$\Delta t/\Delta x$	temperature gradient
Λ	constant
C_y	specific heat

LISTS OF SYMBOLS (continued)

mv	millivolts
m_B	Bohr magneton
E_0	excitation energy of the nucleus
E_r	energy of the emitted gamma rays
E_r	total recoil energy
$\hbar$	Planck's constant
$\overline{D}$	Doppler broadening
v_0	Doppler velocity
f	Debye-Walker factor
$\langle x \rangle^2$	mean square displacement of the atom in its termal vibrations about its origin
E_γ	peak of energy distribution
Γ	full width at half maximum of the emission line
H_g	hyperfine magnetic field from a single electron
Ψ	Fermi contact interaction
μ_N	nuclear magneton
g_0	g-factors for J =1/2
g_1	g-factors for J = 3/2
$\lvert\Delta\varepsilon\rvert$	energy splitting in the hyperfine magnetic field due to quadrupole moment
δ	Doppler width, distance that perturbations travel
T_B	blocking temperature

CHAPTER 1

INTRODUCTION

Electrospinning is the process of producing high surface area submicron and nanosize fibers that consist of higher physical properties (e.g., mechanical, magnetic, electrical, and thermal, etc.) than their bulk-size fibers. Electrospinning is related to the principle of spinning polymer solutions in a high electric field. Nearly all synthetic and naturally occurring polymers have been electrospun so far. In electrospinning, a high-voltage or high-electric field is used to overcome the surface tension of the polymeric solution. When the intensity of the electric field is increased beyond a certain limit, called threshold intensity, the hemispherical surface of the polymer solution at the tip of the capillary tube begins to elongate in a structure known as a Taylor cone [1]. Electrospun fibers form from the plastic stretching of a jet of polymeric solution while the solvent evaporates and the polymer solidifies at micro- and nanolevels.

The term “electrospinning” was drived from “electrostatic spinning” because an electrostatic field is used to fabricate fibers. Use of this term has increased since 1994 [2, 3]. Formhals first patented the electrospinning process in 1934 [2]. In 1969, Taylor studied the shape of the polymeric droplet at the tip of the capillary and demonstrated that a jet is ejected from the vertex of the cone [1]. Later on, most researchers around the world focused their attention on surface morphology and characterization of the electrospun nanofibers. Electrospinning is a relatively easier and direct process of fabricating a non-woven mat of polymer fibers compared to conventional methods such as melt spinning, wet spinning, extrusion molding, etc. It offers the distinct advantage of forming fibers in the micron to nano range, and it offers a high surface area-to-volume ratio compared to conventional fiber-forming techniques [4].

Electrospinning is not a new technique for manufacturing submicron size fibers. It has been in existence since the 1930s; however, it never gained substantional industrial importance in the past several decades because of low productivity. Recently, some special needs of biomedical, filtration, and military applications have reinvigorated interest [5, 6]. Electrospinning utilizes a high electric field or high electric force on the surface of a polymeric solution to overcome surface tension and produce a very slim-charged jet. A polymeric solution is held by its surface tension at the end of the capillary tube. The liquid meniscus emanating from the capillary (capillary stress) has a stress of the order of γ/r, where "γ" is the surface tension of the polymeric solution, and "r" is the radius of the meniscus. The stress induced due to an applied field (Maxwell stress) can be given by [7]

$$\sigma = (\varepsilon V^2)/H^2 \tag{1.1}$$

where "ε" is the permittivity, "V" is the applied voltage (spinning voltage), and "H" is the distance between the capillary and the collection screen. As far as other forces like inertia, viscoelastic, and hydrostatic pressure are concerned, their effects can be neglected in comparison to a high-electrostatic field. By balancing the two stresses, it is possible to estimate the critical voltage (V_C) that must be overcome to cause electrospinning [7] as

$$V_C = \sqrt{\frac{\gamma H^2}{r\varepsilon}} \tag{1.2}$$

Most polymeric solutions can be electrospun at 7–10 KV, but to produce fibers in the nano range, the applied voltage should be higher than this. When a charge is applied on the polymeric solution, mutual charge repulsion induces longitudinal stresses. As the intensity of the electrostatic field increases beyond a certain limit (V_C), the hemispherical surface of the solution at the tip of the capillary elongates to form a structure called the Taylor cone [1, 8]. The jet first extends in a straight path for some distance, which is called the jet length [9, 10], and then

instability occurs after relaxation of the jet, where the jet bends and follows a looping path [9]. The electrostatic field elongates the jet thousands of time, and it becomes very slim. Finally, the solvent evaporates, and fine submicron fibers are gathered on a collector screen placed at some distance from the capillary tube, as shown in Figure 1-1.

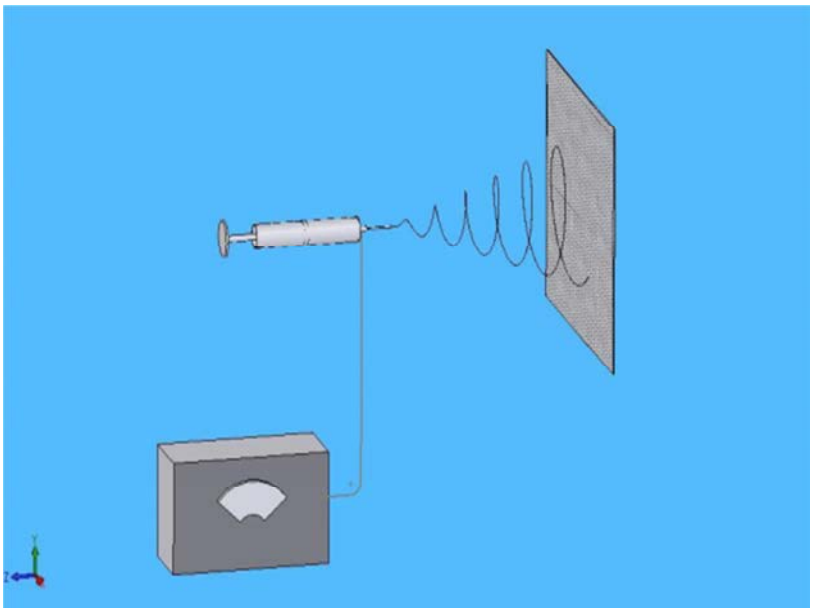

Figure 1-1. Setup of electrospinning process.

Nanofibers have diameters ranging from 500 nm to less than 100 nm. Many different polymers are electrospun into fibers with diameters from less than 100 nm to as small as 10 nm. The thinnest nanofiber produced via electrospinning had a diameter of around 3 nm. The fundamental advantage of electrospinning is its ability to produce nanofibers in a short period of time. A wide variety of shapes and sizes of electrospun fibers can be produced from various classes of polymers. Most features can be controlled by altering the process parameters and the concentration of polymer. Electrospinning involves many branches of science and technology such as chemical, mechanical, colloidal science, polymer science, electrical, fluid mechanics, and material engineering and rheology [9].

Polymer nanofibers are being used in filtration systems [11, 12], protective clothing [13], and biomedical applications, including wound dressing [14, 15], artificial blood vessels [16, 17], sutures, and drug-delivery systems [9]. Other possible applications include solar cells, light sails, photonic devices, and mirrors [9, 18]. Nanofibers offer tremendous advantages in applications like pesticides for plants, structural elements in artificial organs, scaffolds for growing cells [9, 19], supports for enzymes or catalysts that can promote chemical reactions, and reinforcement for composites [9, 20, 21]. The surface of electrospun nanofibers can be modified by coating them with many substances. Nanofibers can be used as templates for making small tubes. Ceramic or carbon nanofibers made from polymer precursors extend nanofiber applications involving high temperature such as thermophoto-voltaic generators and high-modulus composites [22, 23]. Ceramic electrospun fibers are made by electrospinning either a sol-gel mixture, or a mixture of inorganic and organometallic compounds with a guide polymer. In addition, polymeric electrospun nanofibers can be coated with solutions of inorganic metallics and organometallics. In all cases, electrospun nanofibers are heated to remove the organic substances and to convert these electrspun nanofibers into ceramic electrospun nanofibers [9].

The electrospinning process can incorporate many substances into nanofibers. Some small insoluble particles that can disperse into solution can be electrospun. Those particles can be encapsulated in dry nanofibers. Polymer nanofibers and nonwoven mats of nanofibers provide the matrix that supports such additives/inclusions. Many useful substances can be incorporated into electrospun nanofibers. Different polymers that can dissolve in the same solvent can be electrospun simultaneously, forming nanofibers with the polymer in separate phases [9].

There are many advantages of using electrospun nanofibers:

- Many flame resistant polymers, such as polyetherether ketone (PEEK), can be electrospun.
- The surface area of nanofibers is 100 to 10,000 times greater than that of conventional fibers.
- The noise-absorption rate in nanofibers is expected to be exponentially higher because of the interaction of air molecules of sound waves with the fiber surfaces.
- The overall weight of materials used for noise absorption will be lighter.
- Nanofibers can enhance the physical properties of composites.
- Nanofibers can be electrospun on both composite and metal surfaces.
- Adhesives can be added to polymers to improve the adhesion between the fiber and the surface.
- Electrospinning is an economical and technologically mature method for bulk production.

1.1 Conventional Fiber-Forming Techniques

1.1.1 Solution Spinning

In solution spinning, a polymer is dissolved in a suitable solvent and drawn through a bath of non-solvent. This system is described by a ternary phase. The initial concentration of the polymer solution is important, as it essentially determines the route of phase separation and growth or spinodal decomposition [25]. Figure 1-2 shows the schematic of a solution-spinning process [24]. As the fiber is drawn into the non-solvent, the polymer is first precipitated in the form of a gel at the surface. After this process, the fiber is stretched by rotating on drums. During stretching, the fiber molecules orient themselves, and the solvent separates out [25].

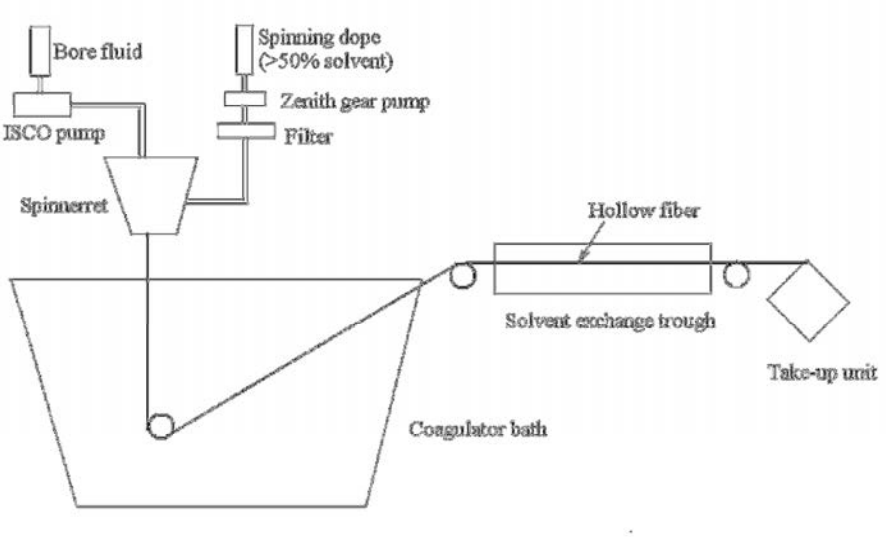

Figure 1-2. Schematic of solution-spinning process [24].

1.1.2 Wet Spinning

In wet spinning, the fiber-forming substances are dissolved in a solvent (Figure 1-3). The spinnerets are submerged in a chemical bath, and as fibers come out of the bath, they precipitate from the solution and solidify. Since the solution is extruded directly from the precipitating liquid, this method is called wet spinning and is used for making acrylic, rayon, and modacrylic and spandex fibers [25].

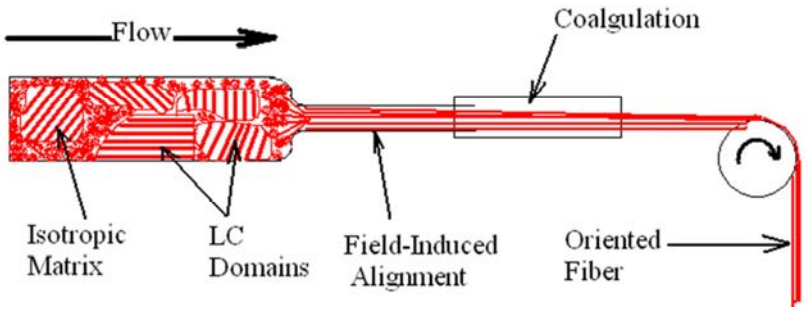

Figure 1-3 Schematic of wet-spinning process [26].

1.1.3 Dry Spinning

In dry spinning, fibers are formed by solution methods, similar to the wet-spinning process, but instead of precipitating the solvent by chemical reaction, solidification is achieved by evaporating the solvent in a stream of air or inert gas (Figure 1-4). The filaments are not exposed to the precipitating liquid, thus making it easier for fiber formation as well as solvent recovery. Acetate, triacetate, acrylic, modacrylic, polybenzimidazole, spandex, and vinyon fibers can be fabricated using this process [25].

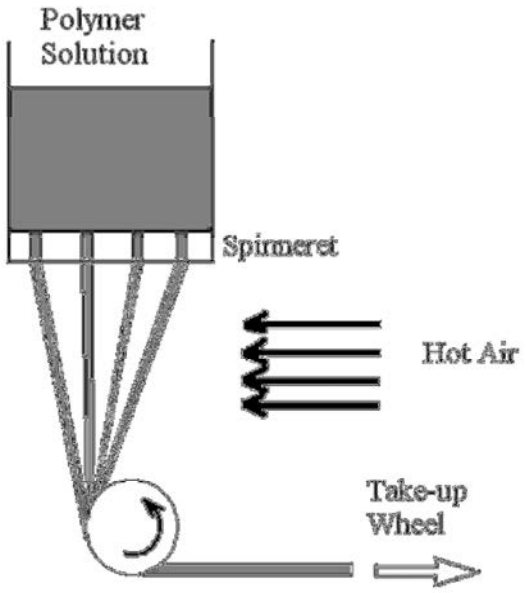

Figure 1-4. Schematic of dry-spinning process [27].

1.1.4 Melt Spinning

Melt spinning is the preferred method of manufacturing polymeric fibers. The polymer is melted and pumped through a spinneret (die) with numerous holes (one to thousands). The molten fibers are cooled, solidified, and collected on a take-up wheel (Figure 1-5). Stretching of the fibers in both the molten and solid states provides for orientation of the polymer chains along

the fiber axis. Polymers such as poly (ethylene terephthalate) and nylon 6, 6 can be spun-melted in high volumes [27].

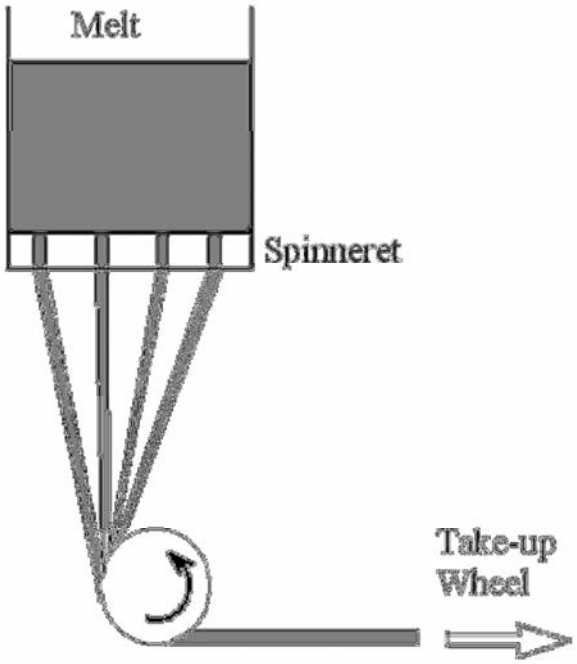

Figure 1-5. Schematic of melt-spinning process [27].

1.1.5 Gel Spinning

Gel spinning is a special process used to obtain high-strength or other special fiber properties. Fibers are spun from a semi-dilute solution and quenched in a liquid bath. This causes the polymer to solidify and form a gel fiber. Upon stretching the solidified filament, the chains are extended and oriented. This results in stronger inter-chain forces in the filaments, giving the fibers a high tensile strength and high stiffness. This process (Figure 1-6) involves the following steps:

1. A semi-dilute polymer solution is extruded through spinneret orifices into a quench bath. The solution solidifies rapidly and forms an oriented gel fiber in which the polymer molecules are randomly aligned.

2. The gel fiber is then heated in an oven. Upon drawing, it becomes 100 times longer than its original length, which increases the tensile strength of the fibers.

Gel spinning produces strong inter-chain forces in the resulting filaments that can significantly increase the tensile strength of fibers. In addition, the liquid crystals are aligned along the fiber axis by the shear forces during extrusion. The filaments emerge with an unusually high degree of orientation relative to each other, which further enhances strength. This process can also be described as dry-wet spinning, since the filaments first pass through air and then are cooled further in a liquid bath. Some high-strength polyethylene and aramid fibers are produced by gel spinning [25, 28].

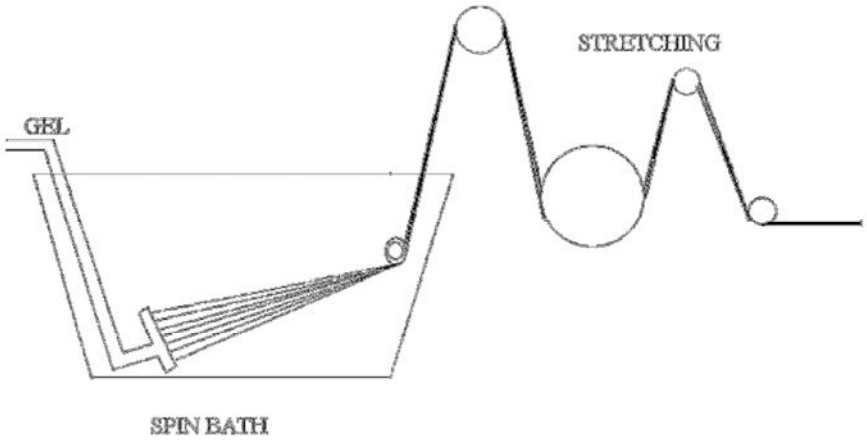

Figure 1-6. Schematic of gel-spinning process [28].

1.2 Nanofiber-Forming Techniques

Various methods are used to produce nanofibers. A few of them are explained below.

1.2.1 Drawing

In this process, the fiber-forming substances are mechanically streched into the desired shape. The material must sustain large deformation without failure [29].

1.2.2 Template Synthesis

In template synthesis, nonporous membranes are used as a template to produce nanofibers. The main disadvantage of this process is that it cannot produce continuous fibers [29].

1.2.3 Phase Separation

Phase separation involves disolution, gelation, and extraction through a solvent. Sebsequent drying results in a nano-range porous foam. The only disvantage of this process is that it takes longer in order to transform the polymer from a solid form to a porous form [3, 29].

1.2.4 Self-Assembly

In self-assembly, the fiber-forming substances organize themselves into a nanoscale preferential pattern. This process, like phase separation, is also time consuming [29].

1.2.5 Electrospinning

In electrospinning, no mechanical force is used. The only force involved is the electrostatic field, which causes the polymer solution to emerge from the pipette, form a cone at the apex of the pipette, then whip around because of the unstability in the electrostatic field, and stretch plastically to produce nanofibers [29].

1.3 Nanomaterials

The properties of nanomaterials are different from bulk materials. Once materials are reduced to nanoscale, they exhibit unusal and exotic properties. For example, silver is opaque in bulk form, but once it is reduced to nanosize it becomes transparent; gold becomes liquid when it is in nanosize. Many researchers have studied this abnormal behavior of nanomaterials, and they have outlined three reasons for the abnormal behavior: quantum size effect, surface and interface effects, and characteristic length scale.

1.3.1 Quantum Size Effect

When materials are in bulk form, they contain thousands of atoms, but when they are reduced to nanosize, they contain only a few atoms; therefore, the density of states in the valence and conduction bands decreases, and as a result, properties change drastically. Electrons lose their freedom in all directions, leading to discrete energy states. The energy of the electron is not large enough to break this confinement. As a result, unusal properties are observed, which is called the quantum size effect.

1.3.2 Surface and Interface Effects

Nanomaterials contain a large number of surface atoms per unit volume. The ratio of surface atoms to interior atoms increases drastically once the materials are in nanosize. This high ratio results in unexpected physical and chemical properties of the materials. The surface on the top possesses fewer atoms than the interior surface; thus, there are broken bonds exposed to the surface. Surface atoms are inward directed, and the bond distance between surface atoms and subsurface atoms is smaller than interior atoms. When the material is in nanosize, this decrease in bond length between surface atoms and interior atoms becomes critical, and the lattice constant of the entire nanoparticle shows remarkable reduction as well. Due to the large number of broken bonds on the surface of nanomaterials, they possess a high surface area and high surface energy, both of which cause them to become unstable.

1.3.3 Characteristic Length Scale

The properties of a material are determined by coupling between two size dependencies. While studing nanomaterials, it is important to understand the length scale. There are two distinct features of nanograin materials that lead to exotic properties: one is the dimension characteristic

of the physical phenonmenon involved, called characteristic length, and the other is the microstructural dimension, designated as size parameter. The range in which these two physical properties differ or coincide is of great interest to researchers. Conventional-size laws often fail to explain this, and in many cases, these laws are reversed.

1.4 Motivation and Objectives

Conventional fiber-forming techniques produce fibers in the range of 5–500 microns. These techniques rely on mechanical forces to produce fibers. Electrospining offers a different approach to producing fibers by introducing electrostatic forces instead of mechanical forces and producing fibers in the nano range. The main advantage of the electrospinning process is its ability to produce fibers in the nano range quickly and with minimum investment. The objectives of the current project are to add nano inclusions in polymeric solutions, fabricate fibers via the electrospinning process, and investigate the physical properties of nanocomposite fibers. Specific goals are to do the following:

1. Produce nano- and microfibers via electrospinning, and determine the surface morphology of fibers using scanning electron microscopy (SEM) and atomic force microscopy (AFM).
2. Study the dielectric properties of polyvinylpyrrolidone (PVP) and polyacrylonitrile (PAN) nanocomposite fibers at different temperatures.
3. Study load and temperature effects on PVP and PAN nanocomposite fibers.
4. Determine the thermal characterization of PVP and PAN nanocomposite fibers.
5. Determine the acoustical characterization of nanocomposites fibers.
6. Find the magnetic properties of PVP and PAN nanocomposite fibers.

1.5 Organization of Thesis

In this research, the electrospinning process was studied, nanofibers were produced from polymeric solutions of PVP and PAN, and the surface morphology of electrospun fibers was determined using SEM and AFM. Nano inclusions—multiwall carbon nanotubes (MWCNTs) and $NiZnFe_2O_4$—were added to a polymeric solution, and the surface morphology of electrospun nanocomposite fibers was determined. The dielectric properties and temperature effects on dielectric properties were studied, and the reasons for changes in dielectric properties at high temperature were determined. The load and temperature effects on electrical resistance, thermal conductivity, and acoustical characterization of nanocomposite fibers were studied, and the scientific reasons of change in these properties were investigated. Mössbauer spectroscopy, vibrating sample magnetometer, and the superconduction of quantum interface devices (SQUIDs) were also performed.

1.6 Properties of Nanofibers

Nanofibers posses some unique properties, all of which make them an ideal material for many industrial applications [29]:

- High aspect ratio
- Nanosize diameter
- Good surface morphology
- Large surface area-to-volume ratio
- Thermal and chemical stability
- Low ohmic resistance
- High porosity
- High directional strength

1.7 Summary

In this chapter, the electrospinning process was discussed briefly, and an equation that can be used to determine the critical voltage (threshold voltage) during electrospinning was developed. Also discussed in this chapter were all conventional microfiber techniques, such as solution spinning, wet spinning, melt spinning, dry spinning, and gel spinning, as well as all nanofiber-forming techniques such as drawing, template synthesis, phase separation, self-assembly, and electrospinning. In addition, some important features of nanomaterials were covered in this chapter.

CHAPTER 2

HISTORICAL BACKGROUND OF ELECTROSPINNING

Electrospinning is not a new technology. The phenomenon that a spherical drop of water on a dry surface is drawn into a cone when a piece of electrically charged amber is held at a suitable distance above it was pointed out 370 years ago by William Gilbert [1]. This was the beginning of the electrospinning process [9].

Lord Rayleigh [9, 30, 31, 32] studied the hydrodynamic stability mechanism of a liquid jet, with and without an applied electrostatic field. In 1882, he examined the instability mechanism in an electrified liquid jet and showed that the electrostatic force overcomes surface tension, which acts in the opposite direction, and liquid is thrown out in the form of fine jets [9]. In 1960, Taylor [30, 33, 34] studied the disintegration of water drops and demonstrated that a conical interface between two fluids could not exist in equilibrium in an electrostatic field. He found that a droplet elongates at the onset of bending instability at its end and is transformed into a conical shape with a semi-vertical angle of 49.3 degrees. This was the first suggestion for development of Taylor cone, which was discussed extensively later on by researchers around the world [9].

The electrospinning of a polymeric solution has been done since the 1930s [35, 36]. Some patents by Formhals [35, 37] contain different experimental setups, the collection of elecytrospun fibers, and their applications during that time. In 1971, Bumgarten [38, 39], using a simple apparatus, was successful in generating electrospun microfibers using a polyacrylonitrile/ dimethylformamide (DMF) solution. The polymer solution was suspended from a stainless steel capillary tube, and a high voltage was applied. He observed that the diameter of the jet reaches a minimum value with an initial increase in the applied voltage and then increases with an increase

in the applied field. Larrondo and Manley [39] studied the relationship between the melt temperature and fiber diameter of polyethylene and polypropylene, and found that the fiber diameter decreased by increasing the melt temperature. In 1987, Hayati [39] demonstrated the effects of an electrostatic field, process conditions, and process parameters on electrospun fibers. He found that the conducting polymeric solution with a high-applied electrostatic field produced an unstable jet that looped around and whipped in different directions.

In 1994, Reneker and Doshi [40, 41], studied the electrospinning of polyethylene oxide (PEO). Reneker and Srinivasan [42, 43] electrospun a liquid crystal system, poly solution (p-phenyleneterephthalamide) in sulfuric acid and an electrically conducting polymer poly (aniline) in sulfuric acid. The real surge in the electrospinning process started in 1995, when Renekar and co-workers began publishing several papers on the electrospinning process and its potential applications in industries [9].

In 1995, Reneker and Chun [44, 45] used the electrospinning technique to produce nanofibers from several polymeric solutions such as poly (amic acid) and poly (acrylonitrile). They demonstrated the electrospinning of polymer melts both in air and in vacuum as well.

In 1996, G. J. Vancso and co-workers [46, 47], electrospun poly (ethylene oxide) fibers and used scanning probe microscopy to characterize electrospun fibers. Reneker and Feng [48], used a polymeric solution of nylon 6 and polyimide to produce nanofibers via electrospinning.

Similarily, H.Fong and Weidang [49] used nylon 6 to fabricate nanocomposite fibers. Reneker and Kim [20, 21] electrospun polybenzimidazole nanofibers and studied the reinforcement effects on electrospun nanofibers in a rubber and epoxy matrix. Fabric membrances were electrospun at the U.S. Army research laboratory in Aberdeen [13]. A silicone polyester composite vascular graft was fabricated by an electrospinning technique by Stenoien

[50], in 1998. Zakoob [51, 52] used an electrospinning technique to produce silk nanofibers and compared them with naturally occurring silk fibers. Chaikof and co-workers [53], in 1999, studied the electrospinning of a synthetic elastin-mimetic peptide.

Reneker and Fong [18, 9, 45, 54] demonstrated the electrospinning of beaded nanofibers of poly (ethylene oxide). In 2000, MacDiarmid [55], fabricated a conducting electrospun mat by blending a conducting material, polyaniline, which was doped with camphorsulfonic acid with poly (ethylene oxide). The conductivity of the electrospun mat was found to be lower than the cast film, due to the porosity effects of the fiber texture. Daoheng sun et al. [56] developed a near-field electrospinning (NFES) process to deposit solid nanofibers in a direct, continuous, and controllable manner. A tungsten electrode with tip diameter of 25 μm was used to construct nanofibers of 50–500 nm line width on silicon-based collectors, while the liquid polymer solution was supplied in a manner analogous to that of a dip pen.

Greiner [9, 57, 58] electrospun polylactide from organic solutions such as dischloromethane with the addition of organosoluable salts such as tetraethyl benzylammonium chloride or hyrdophilic polymer-like poly (ethylene oxide). A decrease in fiber diameter was observed in this mixture. Samuelson [9, 59] electrospun sulfonated polystyrene (PS), and enzymatically synthesized polyaniline and its blends into nanofibers.

In 2001, Frank used the electrospinning process to make nanocomposite fibrils with carbon nanotubes (CNTs) [9]. G. Chase [60] used polymeric solutions of nylon, polyacrylonitrile, and Ultem meta-aramid blended with glass fibers to produce nanocomposite fibers.

Electrospinning of biodegradable polymers and biopolymers has generated the considerable interest of many researchers with some very promising results, which were

published by Bowlin et al. [61] on electrospinning of collagen and its use as a band-aid. Several patents on the biomedical applications of electrospun fibers have been reported recently. Notable among them are those filed by Reneker and co-workers [62] who produced a skin mask by directly electrospinning fibers onto the skin surface in order to protect or heal eventual wounds. Another scientist, P. Gibson [63], who reported the production of electrospun fibers containing pH adjustment substances for use in wound dressing. In 2003, poly (ethylene terephthalate-co-ethylene isophthalate copolymers), poly (hexyl isocyanate), cellulose, poly (3, 4 ethylenedioxythiophene), and acrylonitrile-butadiene-styrene were electrospun from different polymeric solutions [9]. Electrospinning technology has been used for the preservation of enzymes and chemical warfare protective clothing. Functionalized silk fibers containing various peptides, such as poly-L-aspartic acid, poly-L-glutamic acid, poly-L-lysine, were fabricated by electrospinning after adding functional peptides into poly (ethylene oxide) [64, 9]. The functionalized silk mats were used as matrixes for in vitro growth of calcium carbonate and hydroxyapatite [9].

In this modern era, the electrospinning technique has drawn the attention of many researchers and scientists around the globe. In 2003, more than 250 research papers were published on electrospinning. In 2003 and 2004, more than 300 research papers were published on electrospinning. These figures are increasing every year. A sudden rise in research on electrospinning is because of the latest knowledge of the industrial applications of nanofibers. Several companies such as Donaldson, Espin, Star, and Nanomatrix are applying this technology to produce nanofibers.

CHAPTER 3

ELECTROSPINNING PROCESS

3.1 Process Details

Electrospinning is a process in which a high voltage, and consequently a high electric field, is used to directly fabricate nanofibers. A polymer melts or solution is held by its surface tension at the end of a capillary tube. A charge is induced into the liquid by an electric field. Mutual charge repulsion creates a force that overcomes the surface tension. As the intensity of the electric filed is increased, the hemispherical surface of the solution at the tip of the capillary tube elongates to form a structure known as the Taylor cone [1]. When the electric field reaches a critical value, the repulsive forces overcome the surface tension, and a continuous charged jet of liquid is ejected from the tip of the cone. After accelerating for a few centimeters, the jet allegedly splits and re-splits or whips around into many fibers. The thinning of the jet is caused by the bending instability associated with the electrified jet. The jet begins to stretch and whip around forming a single nanofiber as it travels to the grounded collector screen. During the jet's flight, most of the solvent evaporates and jet is finally collected on a grounded collector screen [8]. Figure 3-1 shows a schematic of the electrospinning process.

The electrospinning technique is similar to the commercial process for microscale fibers drawing except for the use of electrostatic repulsion between surface charges rather than a mechanical or shear force as the drawing force. A syringe pump can control the flow rate of the polymeric solution. The distance between the grounded collector and the tip of the capillary can be altered. Generally, a higher distance (20–30 cm) between the grounded collector and tip of the capillary is used.

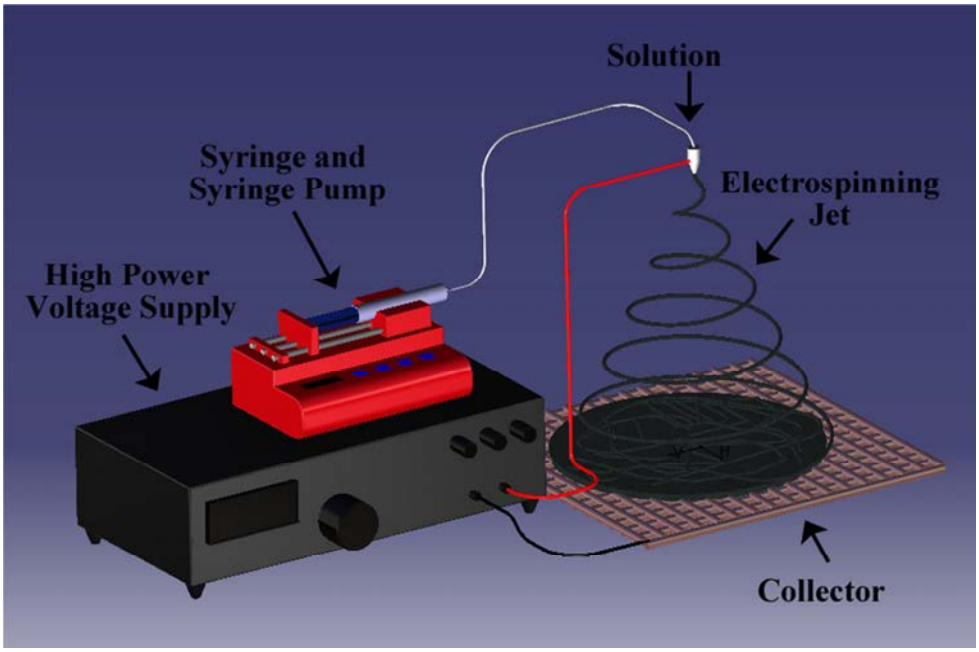

Figure 3-1. Schematic of electrospinning process.

When an external electrostatic field is applied to the polymeric solution, the positive and negative ions move in opposite directions. Negative ions move towards the positive electrode. The difference in the number of positive and negative ions in a polymeric solution is known as the excess charge, or simply charge. Some of the polymeric solutions are highly insulating, and therefore, salt, such as potassium chloride, is added to the polymeric solution, which dissociates into equal numbers of positive and negative ions and thereby increases the ionic conductivity of the polymeric solution by increasing the number of ions per unit volume, but does not increase the excess charge. The higher conductivity usually shortens the time required for the excess charge, in the form of ions, to move to a particular direction in response to the applied field. When the electrostatic field is applied to the polymeric solution, the surface of the solution is charged and causes the migration of ions through the solution, thus forming a jet, which carries the excess charge [65]. The jet coming out of the capillary tube first follows a straight path and then experiences a sequence of unstable bending back and forth, with growing amplitude in three

dimensions. The jet loop grows longer and thinner simultaneously, and the loop diameter and circumference increases as well. After some time, segments of the loop develop a new bending instability. Each cycle of bending instability can be described in three steps [65]:

1. A smooth segment of the jet that was previously straight suddenly develops an array of bends.
2. The segment of the jet in each bend elongates, and the array of bends becomes a series of spiraling loops with increasing diameters.
3. As the perimeter of the loops increases, the cross-sectional diameter of the jet grows smaller. The condition of step 1 is established on a small scale, and the next cycle of bending instability begins.

It can be observed that the cycle of instability is repeated many times on a smaller scale. As more and more cycles occur, the jet diameter is continually reduced, thus creating nanofibers. After, the second cycle, the axis of a particular segment may point in any direction. The jet evaporates during its flight from capillary tube to collector screen and electrospun nanofibers are collected [65].

The reason for the bending instability can be understood in the following way. In the coordinate system that moves with a rectilinear electrified jet, the electrical charges can be regarded as a static system of charges interacting mainly by Coulomb's law. Such systems are unstable according to Earnshaw's theorem [65]:

> *"Earnshaw's theorem states that a collection of point charges cannot be maintained in a static equilibrium solely by the electrostatic interactions of the point charges."*

This theorem was first applied to a magnetic field but originally was applied to an electrostatic field. To explain the instability mechanism, consider three point charges of the same nature, each with a value "e" and originally in a straight path line at A, B, and C, as shown in Figure 3-2 [65].

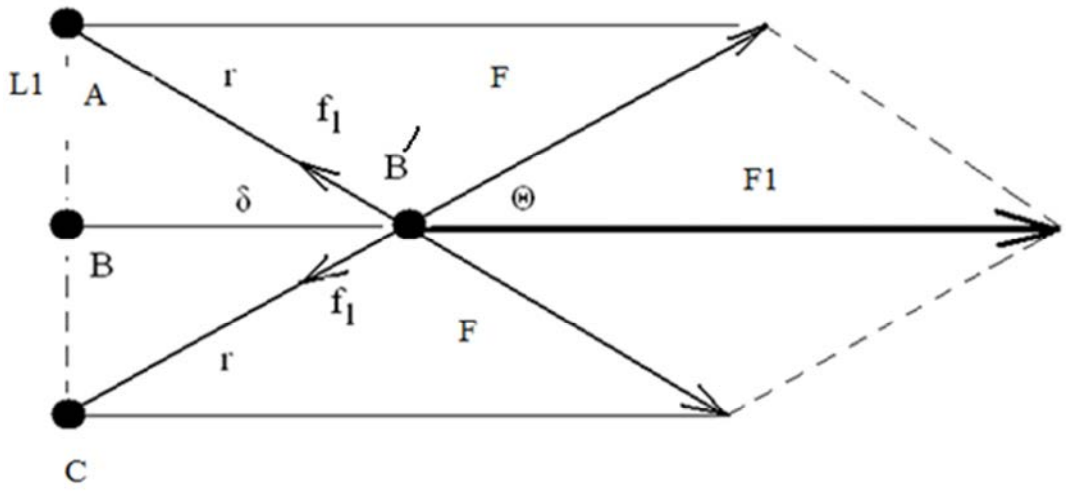

Figure 3-2. Illustration of bending instability [65].

Two Coulomb forces having magnitudes $F = \frac{e^2}{r^2}$ push charge B from opposite directions, which causes B to move to B′ by a distance δ. A force having magnitude $F_1 = 2FCos\theta = 2(\frac{e^2}{r^3})\delta$ acts on charge B perpendicular to straight lines A, B, and C and causes B to move in the direction of perturbation. The growth of perturbations is governed by [65]

$$m.\frac{d\delta^2}{dt^2} = 2e^2.\delta/L_1^3 \tag{3.1}$$

where "m" is the mass of the jet. The solution of this equation, $\delta = \delta_0 \exp\{[\frac{2e^2}{L_1^3 m}]^{\frac{1}{2}} t\}$, shows that small bending perturbations increase exponentially. This increase is sustained because the electrostatic energy of the system decreases as $\frac{e^2}{r}$, when the perturbations characterized by δ and r grow. If charges A, B, and C are attached to a liquid jet, the forces associated with the liquid

tend to counteract the instability caused by the Coulomb forces. For this jet, the influence of the shearing forces related to the bending stiffness can be neglected in comparison to the longitudinal forces. The bending instability can always overcome the viscoelastic forces, since the Coulomb force increases when the wavelength of the perturbations decreases, but the surface tension always counteracts the bending instability because bending always leads to an increase of the jet area. Surface tension resists the development of a large curvature by perturbation ABC in Figure 3-2 and therefore limits the small perturbation wavelengths [65].

When a jet becomes unstable at some point from the straight path, stress relaxation occurs, and a number of instabilities occur, as shown in Figure 3-3 [66].

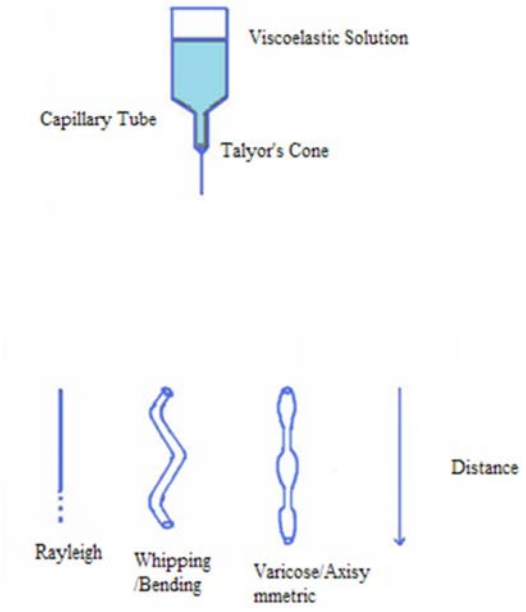

Figure 3-3. Schematic of various types of instabilities emerging from Taylor cone [66].

The instabilities take place after the stress relaxation. The jet undergoes a large reduction in the cross-sectional area, and spiral and whipping motion take place, which is known as the bending/whipping instability of the jet. As a result, the jet can coil and loop itself, as shown in Figure 3-3 [66]. This type of instability is known as varicose instability, the centerline of the jet

remains straight, but the radius of the jet is modulated or changed [66]. The last type of instability is the axisymmetric breakdown of a continuous cylindrical column of liquid into spherical droplets, which is known as Rayleigh instability, whereby a stream of liquid can break up into small droplets if its length is greater than its diameter. This type of instability can be suppressed at a high electric field [66].

Depending upon the applied field and other process parameters, a variety of jets can emerge from the Taylor cone, as shown in Figure 3-4 [66]. In dipping mode, spherical droplets may emerge from the Taylor cone [66, 67, 68, 69]. In spindle mode, the jet is elongated into thin fibers before it breaks up into small droplets. In oscillating mode, the jet is twisted and drops are expelled. In precession mode, the looping jet is initiated from the capillary tube and then breaks up into many droplets. Generally, electrospinning is carried out by cone jet mode.

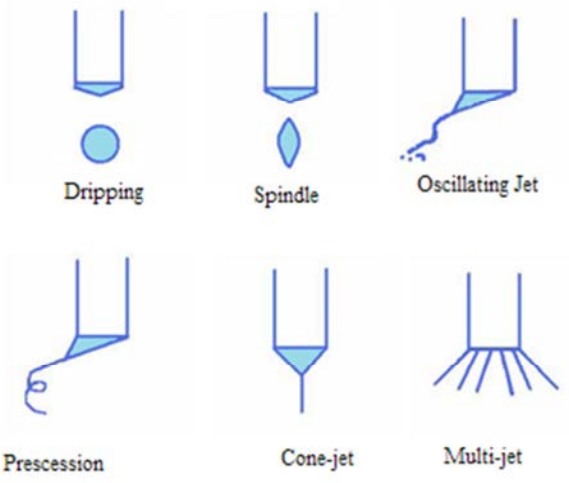

Figure 3-4. Schematic of various modes of charged jets emerging from Taylor cone [66].

The electrospinning jet has three regions, as shown in Figure 3-5: the base, where the jet emerges from the Taylor cone; a region, just after the base, where the jet stretches and accelerates, the diameter of the jet decreases, the length of the jet increases, and the jet moves

towards the collector screen with a whipping and looping motion; and the collector region, where fibers are collected [66].

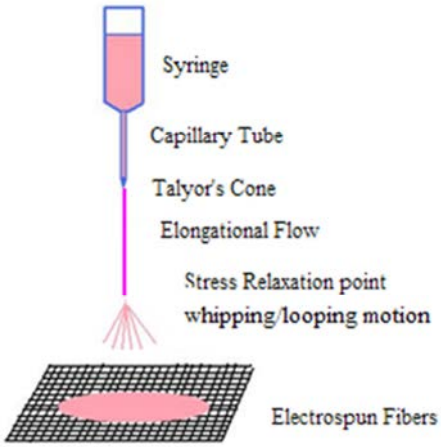

Figure 3-5. Schematic of various regions in electrospinning process [66].

The region of interest is where the whipping/looping motion occurs, that is, where the jet splits into numerous subjets, reducing the jet's diameter to submicron size and finally collecting on the collector screen.

3.1.1 Mathematical Models for Initiation and Bending Instability of Jet

Many researchers have proposed mathematical models for electrospinning. Some of them are outlined here.

Spivak and Dzenis [70] modeled the movement of a conductive jet by an electrostatic field, considering inertia, hydrostatic, viscoelastic, and surface tension forces. The polymeric solution was described as a non-linear rheological constitutive equation, which is governed by the Ostwald-de Waele law. It is obvious that Newton's law of viscosity cannot treat non-Newtonian fluid. Therefore, other approaches should be considered, which lead to a rheological constitutive equation. The simplest one is the Ostwald-de Waele power law:

$$\tau_{yx} = -k|dv_x/dy|_1^{n-1} dv_x/dy \tag{3.2}$$

where dv_x/dy is the value of the rate of shear, "k" is the consistency index, and "n" is the flow behavior index. It is also possible to drive the expression

$$\tau_{yx} = k\,(\frac{d\gamma}{dt})^n \tag{3.3}$$

where $d\gamma/dt$ is the rate of strain, and $\frac{d\gamma}{dt} = dv_x/d_y$. For a fluid that is described by a nonlinear rheological constitutive equation, the electric current due to ionic conductivity of the polymeric solution is very low as compared to the current provided by convective charge transfer due the movement of the fluid elements, but the conductivity is high enough to transfer the charges to the surface of the jet. The surface charge interacts with the applied potential, and as a result, a force is developed that is responsible for jet acceleration. The overall electric potential is the sum of the surface potential and applied potential. The linear moment balance would result in the following equation of motion in axial direction [70, 71]:

$$d/dx[\tfrac{\rho}{2}\pi R^2 v^2 + \pi R^2 \rho - \mu\pi R^2(\left|\tfrac{dv}{dx}\right|)^{m-1}]dv/dx = 2\pi R\omega E \tag{3.4}$$

where "v" is the average jet velocity, "R" is the radius of the jet, "m" is the mass index, and "ω" is the surface charge density. The hydrostatic pressure ρ can be determined by the surface tension and electrostatic repulsion. Spivak and Dzenis approximated the slender jet as [70]

$$P = \frac{\gamma}{R}\frac{\omega^2}{2\varepsilon_0} \tag{3.5}$$

where "γ" is the surface tension coefficient, and "ε_0" is the dielectric permeability of the vacuum. The mass and electric charge balance equation can be given by [70]

$$\pi R^2 v = Q \tag{3.6}$$

$$2Q\frac{\omega}{R} - \pi\sigma_e R^2\frac{d\phi}{dz} = I \tag{3.7}$$

where "Q" is the volume flow rate, "σ_e" is the electrical conductivity of the fluid, and "I" is the current. For a less conductive polymeric solution, the current will be [70]

$$I = 2Q\omega/R \tag{3.8}$$

Where the dimensionless jet radius, $R_1 = {}^{R}/_{R_0}$ and axial coordinate, $X_1 = {}^{X}/_{X_0}$, where

$$X_0 = \rho Q^3/2\pi^2 R_0^4 EI \tag{3.9}$$

where "R_0" is the radius of the capillary tube, the equation (3.5) and (3.6) reduces to give the following dimensionless equation of jet [70,71]:

$$\frac{d}{dx}\left[R_1^{-4} + WeR_1^{-1} - YR_1^{-2} - \frac{1}{R_e}\left(\frac{1}{2}\frac{d}{d_{z1}}(R_1^{-2})\right)^m\right] = 1 \tag{3.10}$$

The dimensionless parameters in equation (3.10) are Weber numbers, which can be defined as [70]

$$W_e = \frac{2\pi^2 R_0^3 \gamma}{\rho Q^2} \tag{3.11}$$

which describes the ratio of surface tension to inertia force; the parameter Y [70] is

$$Y = (\pi^2 I^2 R_0^6)/(4\varepsilon_0 \rho Q^4) \tag{3.12}$$

which describes the ratio of the electrical to inertia force, and the Reynolds number for the fluid [70] is

$$R_e = {}^{Q^2\rho}\Big/_{(R_0^4 2\pi^2\mu)[4\pi R_0^2 EI/Q^2\rho]^{-\mathrm{m}}} \tag{3.13}$$

which describes the ratio of inertia force to viscous force. Integrating equation (3.10) yields [70,71]

$$\left\{R_1^{-4} + WeR_1^{-1} - YR_1^{-2} - \frac{1}{R_e}\left[\frac{1}{2}\frac{d}{d_{z1}}[R_1^{-2}]\right]^m\right] = X_1 + C \tag{3.14}$$

where "C" is the constant of integration. A power law asymptotic approximation of the jet radius is $R_1 \sim X_1^{-\alpha}$, where "α" is a constant. Substituting α in equation (3.14) yields [70,71]

$$X_1^{-4\alpha} + W_e X_1^{-\alpha} - YX_1^{-2\alpha} - \frac{\alpha^m}{R_e} X_1^{(2\alpha-1)m} - X_1 = O(1) \tag{3.15}$$

The power balance as $X_1 \to +\infty$ yields

$$4\alpha = \max[1, (2\alpha - 1)m] \tag{3.16}$$

For pseudoplastic and dilatants fluids with flow index m having values in the range of 0 to 2, the solution of equation (3.16) is $\alpha = {}^{1}/_{4}$, which is governed by the power law for Newtonian fluids [70,71]:

$$R_1 = X_1^{-1/4} \tag{3.17}$$

3.1.2 Mathematical Model for Initiation of Jet

Renekar et al. [65] proposed a mathematical model to describe the whipping or chaotic motion of the jet, also known as the bending instability of the jet. Bending instabilities can be thought of as a system of connecting viscoelastic dumbbells. Consider a rectilinear liquid jet in an electrostatic field emerging from the capillary tube parallel to its axis. A segment of the electrified jet can be modeled as a viscoelastic dumbbell, as shown in Figure 3-6 [65].

Figure 3-6. Viscoelastic dumbbell showing segment of rectilinear portion of jet [65].

The beads, A and B, possess a charge "e" and a mass "m." Suppose the position of bead A is fixed by the non-Coulomb forces. The Coulomb repulsive force acting on bead B is $-\frac{e^2}{I^2}$, where "I" is the filament length. The force applied on B due to the applied electrostatic field is $-eE/H$, where "E" is the applied field, and "H" is the distance between the liquid drop to the collector

screen. The dumbbell, AB, represents a model of a viscoelastic Maxwellian jet. Therefore, the stress, σ, pulling B back to A can be given by [65]

$$\frac{d\sigma}{dt} = \frac{Gdl}{l\,dt} - G.\frac{\sigma}{\mu} \tag{3.18}$$

where "t" is time, and "G" and "μ" are the elastic modulus and viscoelasticity, respectively. The momentum balance for bead B can be given by [65]

$$\frac{mdv}{dt} = -\frac{e^2}{l^2} - e.\frac{E}{h} + \sigma\beta^2\pi \tag{3.19}$$

where "β" is the cross-sectional radius of the filament, and "v" is the velocity of bead B that satisfies the kinematics equation [65]

$$\frac{dt}{dv} = -v \tag{3.20}$$

Based on the experimental observations, several mathematical models have been developed to investigate the electrospinning process. Reneker and co-workers took the charged liquid jet as a system of connected, viscoelastic dumbbells and provided an interpretation for the formation of bending instability [70, 72]. They calculated the three-dimensional trajectory for the jet using a linear Maxwell equation, and the computed results were in agreement with the experimental results. Rutledge and co-workers treated the jet as a long, slender object and thereby developed a different model to explain the electrospinning process [73]. Their experimental and theoretical studies revealed that the electrospinning process involves whipping instability of a liquid jet. The whipping instability is mainly caused by electrostatic interactions between the external applied field and surface charges on the jet. The fiber formation in nanosize is due to the stretching and accelerating fluid filament in the instability zone. They also showed that the model could be extended to predict the saturation of whipping amplitude and the diameter of the resulting fibers [74]. Feng proposed another model to show the motion of a highly charged jet in an electrostatic field, and the role of non-Newtonian rheology in the stretching of an electrified jet was examined

[4]. The electrospinning process is better understood by these models, with their limitations. Nearly all kind of polymers can be electrospun in different solvents. The polymer for electrospinning should have moderate molecular weight. If the molecular weight is too high, then electrospinng will be very difficult. If is too low, electrospinng will be impossible. The solvent should be such that it can dissolve polymer easily.

Viscosity plays an important in electrospinning. At low viscosity, spherical and conical beaded structures are observed. At high concentration, large molecular chain entanglement resists the breaking up of the electrified jet and promotes the electrostatic field to elongate the jet. It has been determined experimentally that at higher viscosity, the spinning drop changes from hemispherical to conical, and the length of the jet increases also. Fiber diameter is related to viscosity by [5]

$$d \sim \eta^{0.5} \tag{3.21}$$

where "d" is the diameter of the fibers, and "η" is the viscosity of the polymeric solution. For creating a fiber diameter in the nano range, the conductivity of the polymeric solution should be high. Beads and pores are observed when the conductivity of the solution is low. When the surface tension of the polymeric solution is low, nanofibers form without any beads or pores. Generally, the fiber diameter (other parameters are constant) depends upon the electrical potential as [5]

$$d \sim V^{-1/2} \tag{3.22}$$

where "V" is the electrical potential. Hendricks [5] calculated the minimum spraying potential of a suspended, hemispherical conducting drop in air as

$$V = 300\sqrt{20\pi\gamma r} \tag{3.23}$$

where "r" is the radius of cone, and "γ" is the surface tension of the polymeric solution. Taylor [1, 5] developed a similar relation for the critical potential as

$$V_c^2 = 4H^2/L^2 \left(\ln \frac{2L}{R} - 3/2\right)(0.117\pi\gamma R) \tag{3.24}$$

where "V_c" is the critical voltage, "H" is the separation between the capillary and the ground, "L" is the length of the capillary, "R" is the radius of the capillary, and "γ" is the surface tension of the liquid.

The morphology of the fibers depends upon the flow rate of the solution. When the flow rate is exceeded, the fibers become surrounded with beads and pores. As the polymer concentration increases, the diameter of the electrospun fibers increases. The shape of the beaded structure changes from spherical to spindle, when the polymer concentration increases. The electrospinning process is usually carried out at room temperature under normal conditions. However, if the temperature is slightly above room temperature, then the evaporation rate will increase, and this will help in reducing the fiber diameter. High airflow will increase the evaporation rate due to convection and will help in reducing the fiber diameter.

3.2 Polyvinylpyrrolidone

PVP is a water-soluble chemically inert solid polymer $(\text{-}CH_2CHC_4H_6NO\text{-})_n$ used chiefly in medicine as a vehicle for drugs. When dry, it is a light flaky powder, which readily absorbs up to 40% of its weight in atmospheric water. In solution, it has excellent wetting properties and readily forms films, which makes it a good coating or an additive to coatings. PVP binds to polar molecules because of its polarity, making it a suitable application in coatings for photo-quality ink-jet papers and transparencies and in inks for inkjet printers.

3.3 Polyacrylonitrile

PAN (C_3H_3N) is a resinous, fibrous, organic polymer. All polyacrylonitrile resins are copolymers made from mixtures of monomer, with acrylonitrile as the main component. PAN fibers are the chemical precursor of carbon fiber. This polymer is modified by a chemical process in order to produce carbon fibers, and these fibers are used to fabricate badminton rackets and tennis rackets, for example.

3.4 Carbon Nanotubes

Carbon nanotubes possess remarkable characteristics such as nanosize, high aspect ratio, and phenomenal electrical conductivity. The combination of these outstanding characteristics makes CNTs suitable for numerous industrial applications. The remarkable electrical and thermal characteristic of CNTs has stimulated many researchers around the globe to use them as inclusions or fillers to enhance polymer properties. CNTs have better thermal characteristic than almost all metals. The physical properties of CNTs have been thoroughly investigated for more than a decade. It has been determined that CNTs consist of higher electrical conductivity, and higher mechanical and thermal properties than their counterparts. For example, CNTs can sustain electrical current densities hundreds of times greater than other conductive metals, and they are produced in both metallic and semiconductor forms. It has also been reported that CNTs are one of the strongest known materials in terms of their tensile strength (150 Gpa) and elastic modulus (1,200 Gpa). This strength comes from the sp2covalent bonds between the individual carbon atoms and the lower density (1.35 g/cm3) of CNTs. Additionally, they are thermally good conductors along the length of the tube, and good insulators laterally to the tube axis. Today, composites made from CNTs garner much attention because of their unique properties. CNTs are either single-wall carbon nanotubes (SWCNTs) or multiwall carbon nanotubes (MWCNTs) (Figure 3-7).

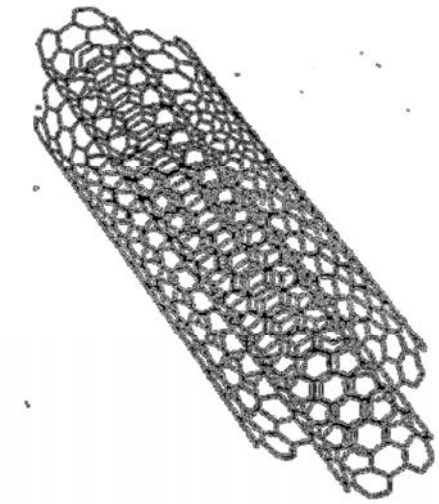

Figure 3-7. Multiwall carbon nanotube (MWCNT).

MWCNTs having a diameter of 140 (+/- 30) nm and length of 7 (+/- 2) microns were used in this research.

3.5 Experiment

Polyvinylpyrrolidone having a molecular weight of 130,000g/mole was purchased from Sigma-Aldrich. MWCNTs with diameters of 140 (+/- 30) nm and lengths of 7 (+/- 2) microns were purchased from Fisher Scientific. Different weight percentages (wt%) (0%, 1/2%, 1%, 2%, and 4%) of MWCNTs were dissolved in ethanol and sonicated for 30 minutes, and then PVP was added and the solution was constantly stirred at 40^0C for 12 hours. Similarly, different weight percentages (1%, 2%, and up to 16%) of $Ni_{0.6}Zn_{0.4}Fe_2O_4$ (NiZn ferrites) were dissolved in ethanol and sonicated for 30 minutes, and then PVP was added and the solution was constantly stirred at 40 ^{0}C for 2-3h.

Polyacrylonitrile having a molecular weight of 150,000g/mole was purchased from Sigma-Aldrich. Different weight percentages (1/2%, 1%, and 2% up to 15%) of MWCNTs were dissolved in dimethylformamide and sonicated for 30 minutes, and then PAN was added and the solution constantly stirred at 40^0C for 12 hours. Similarly, different weight percentages (1%,

2%, and up to 16%) of NiZn ferrites were dissolved in DMF and sonicated for 30 minutes, and then PAN was added and the solution constantly stirred at 40^0C for 2–3 hours.

The prepared dispersion/solution was transferred to a 10 ml syringe that was connected to a capillary needle with an inside diameter of 0.5 mm. A platinum electrode inside the syringe was attached to a high DC voltage supply. The applied voltage is usually within the range of 15–30 KV, and the distance between capillary tip and collector screen is around 15–30 cm. Electrospun fibers were then collected on a grounded screen and dried in an oven at 60^0C for 8 hours to remove all residual solvent. Scanning electron microscopy and atomic force microscopy were used to determine the fiber diameter and morphology.

3.6 Preparation of $NiZnFe_2O_4$

$Ni_{0.6}Zn_{0.4}Fe_2O_4$ was prepared by the usual co-precipitation technique from $NiSO_4$, $ZnSO_4$ and $Fe_2 (SO_4)_3$ according to the following equation:

$$0.6\ NiSO_4 + 0.4\ ZnSO_4 + Fe_2 (SO_4)_3 + 8\ NaOH$$

$$\Rightarrow 0.6\ Ni (OH)_2 + 0.4\ Zn(OH)_2 + 2Fe(OH)_3 + 4\ Na_2(SO_4)$$

$$\Rightarrow Ni_{0.6}Zn_{0.4}Fe_2O_4$$

The sulfates were mixed in required stoichometric ratios in deionized water. Then the NaOH solution was added dropwise while stirring until the pH value became 12. The mixture was stirred continually at 700 rpm for 2 hours while being heated at 80^0 C. Since a dark color was observed due to the formation of the ferrite particles, the mixture's sediment was allowed to settle. The mixture was washed 10 times to remove the sodium sulfate formed. Then the powder sample was dried at room temperature. AFM at Wichita State University was used to determine the particle size of these ferrites. Figures 3-8 (a) and 3-8 (b) show AFM images of NiZn ferrites. It is clear from the images that the particle size of these ferrites is between 21.5 and 28 nm.

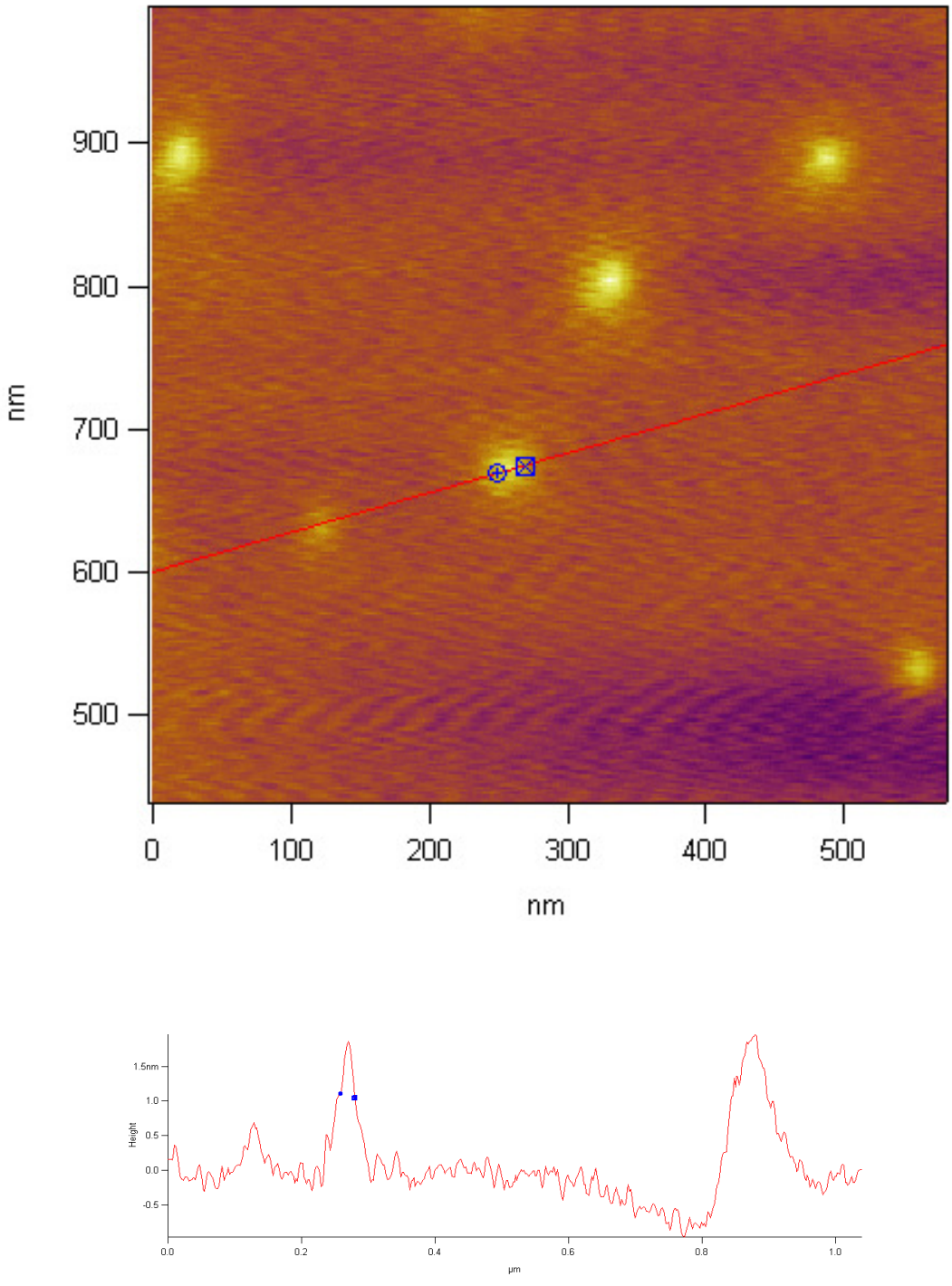

Figure 3-8 (a). AFM images of NiZn ferrites.

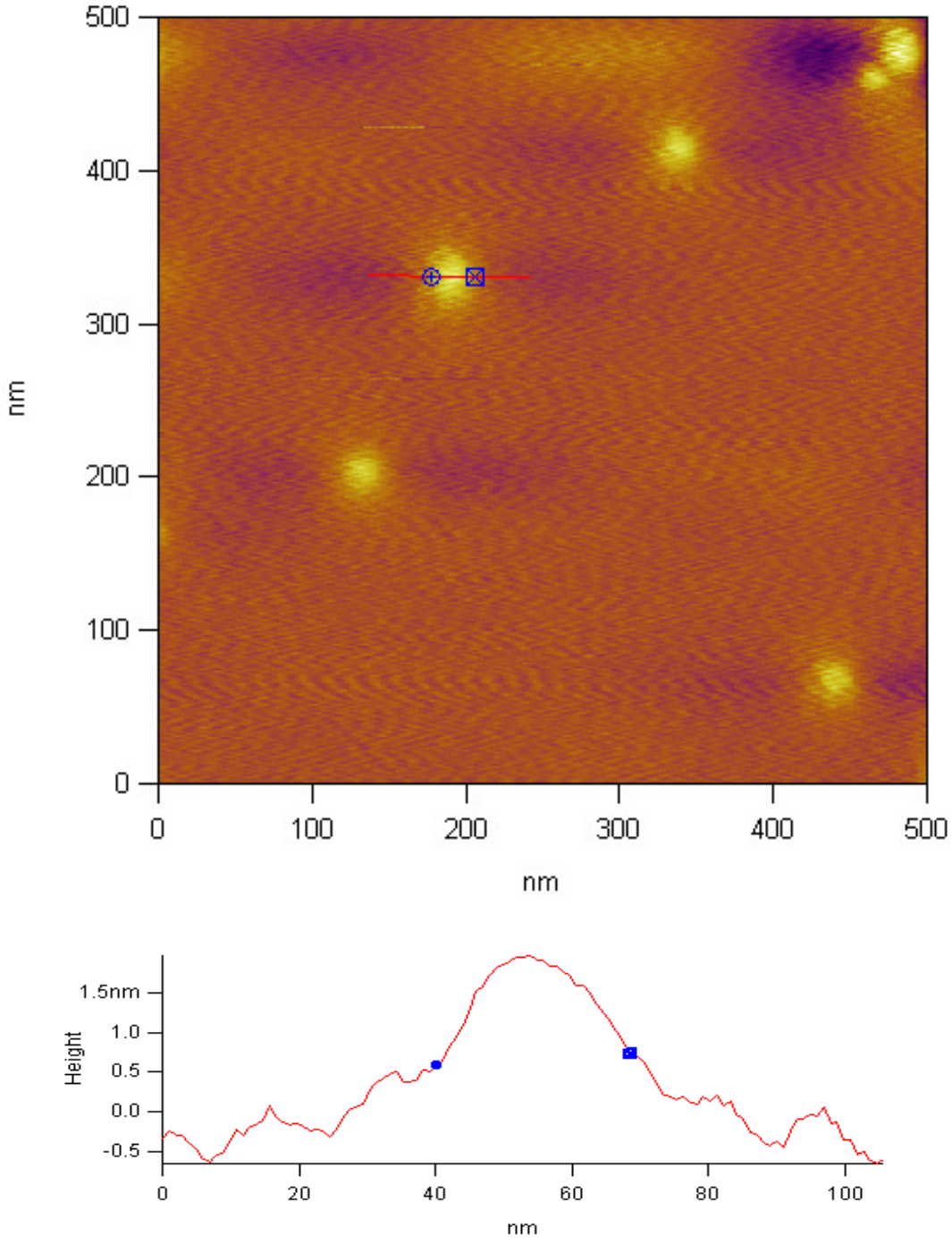

Figure 3-8 (b). AFM images of NiZn ferrites.

NiZn ferrites are commercially important materials because of their high electrical resistance and soft magnetic properties. NiZn ferrites have many industrial applications, such as microwave devices, transformer cores, rod antennas, and read/write heads for high-speed digital

tapes. These ferrites can be prepared by various techniques including combustion synthesis, hydrothermal formation, laser ablation, and a co-precipitation technique. The properties of ferrite materials depend on the material composition and preparation technique. Therefore, the selection of a particular process for preparating ferrites is the fundamental aspect to obtain high quality ferrites. When the ferrite particles are nanosize, their magnetic properties are significantly different then microsize ferrites. The electrical and magnetic properties of ferrites depend largely on the distribution of cations in tetrahedral and octahedral sites and on the deficiencies in chemical compostion, which have different configurations in bulk and in nanophase. It has been observed that the distribution of cations and chemical composition of ferrites depend upon the preparation technique.

Figure 3-9 shows the X-ray pattern of the prepared NiZn ferrite nanoparticles with the identified reflection plans. It is clear from the X-ray pattern that the powder is a single phase of spinel structure.

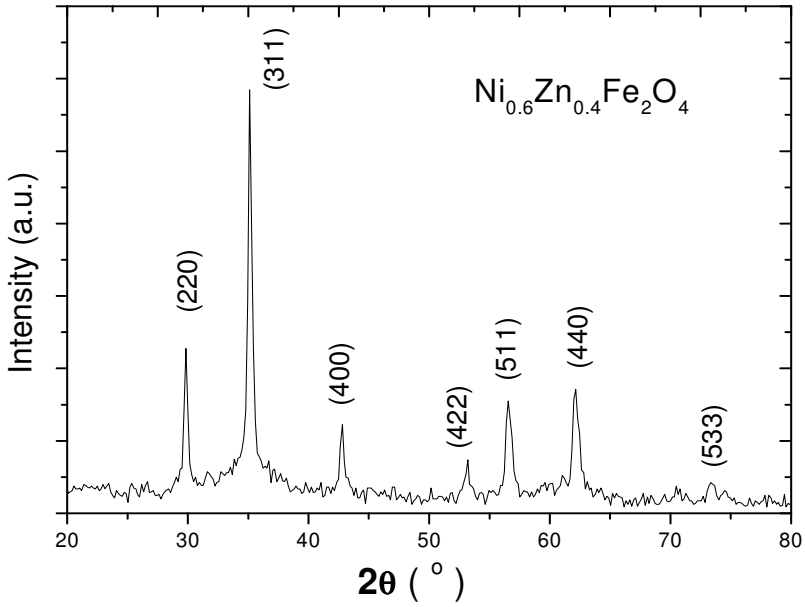

Figure 3-9. X-ray pattern of NiZn ferrites.

3.7 Structure of Ferrites

Ferrites are ceramic magnetic materials having the general formula AB_2O_4, where A and B represent metal ions, and O represents oxygen ions. Ferrites form a crystalline structure. Their spinel structure (Figure 3-10) is composed of a close-packed oxygen arrangement in which 32 oxygen atoms form a unit cell leaving 96 interstitial sites, 64 of them being tetrahedral A sites and 32 of them being octahedral B sites. Each tetrahedral site is coordinated with 4 neighboring oxygen ions, and each octahedral site is coordinated with 6 neighboring oxygen ions. If all the sites are filled with metal ions, of either +3 or -3 valence, the positive charge will be greater than the negative charge, and the structure would be electrically neutral as a whole. Out of 64 tetrahedral sites, 8 sites are occupied by divalent ions, and out of 32 octahedral sites, only 16 sites are occupied by trivalent ions. Therefore, the total positive charge would be $8X(+2) = +16$ plus$16X(+3) = +48$, or a total of +64, which is balanced by $32X(-2) = -64$ oxygen ions. Therefore, the structure is electrically neutral, and each cell of spinel lattice contains eight molecules of AB_2O_4.

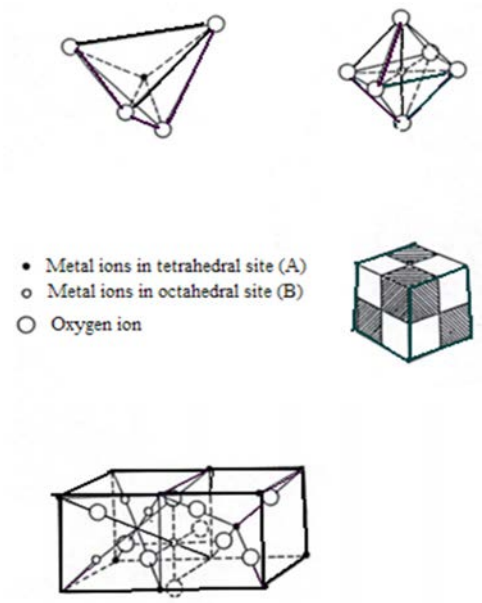

Figure 3-10. Spinel structure of ferrites.

Ferrites can be categorized into three kinds, depending on the occupancy of divalent and trivalent ions between the tetrahedral and octahedral sites:

1. Normal Ferrites
2. Inverse Ferrites
3. Mixed Ferrites

In normal ferrites, the tetrahedral sites are occupied by divalent ions, and the octahedral sites are occupied by trivalent ions such as $A^{2+}[B^{3+}]O_4$. An example of normal ferrites are as follows:

$$Cd^{2+}[Fe_2]O_4 \ \ \boldsymbol{and} \ \ Zn^{2+}[Fe_2]O_4.$$

In inverse ferrites, the divalent metal ions and half of the Fe^{3+} ions are in octahedral sites B. The other half of the Fe^{3+} ions occupy the tetrahedral sites. An example of inverse ferrites are as follows:

$$Fe^{3+}[Ni^{2+}Fe^{3+}]O_4 \ \ \boldsymbol{and} \ \ Fe^{3+}[Co^{2+}Fe^{3+}]O_4$$

In mixed ferrites, both sites A and B are occupied by divalent and trivalent ions. The general cation distribution in a mixed ferrite can be represented as follows:

$$(A_x^{2+}B_{1-x}^{3+})[A_{1-x}^{2+}B_{1+x}^{3+}]O_4^{2-}$$

3.8 Shape of Fibers Produced by Electrospinning

A wide variety of fibers can be produced by electrospinning process. The cross-section of fibers produced mainly depends upon the polymeric solution. Round fibers, branched fibers, flat fibers, and split fibers can be produced by various polymeric solutions. By controlling the various process parameters, individual fibers of submicron size can be produced. A scanning electron microscope (JEOL Model JSM -6460LV) was used to determine the fiber diameter and morphology. Figures 3-11 to 3-24 show SEM images of the electrospun fibers.

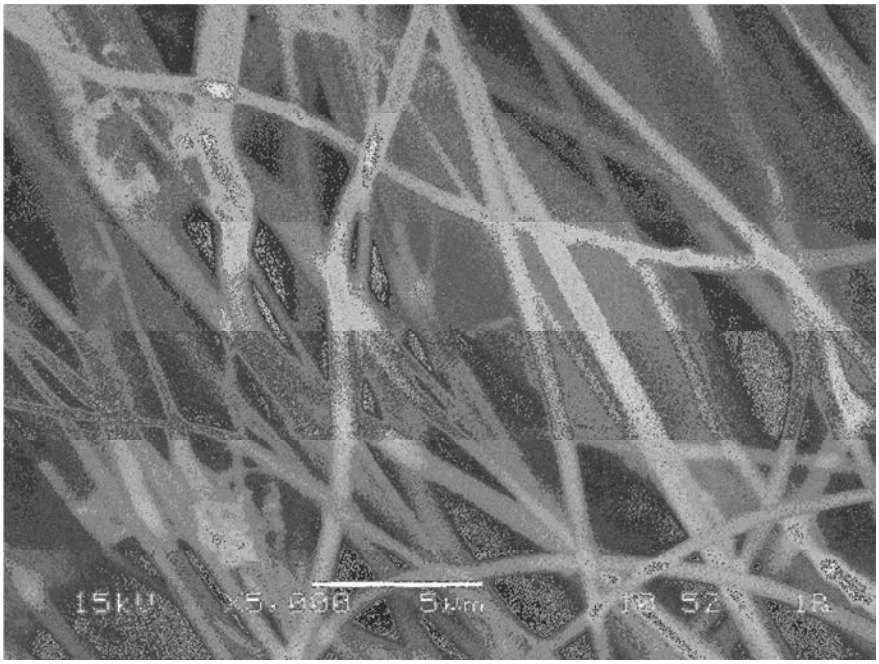

Figure 3-11. SEM image of PVP fibers produced with processing parameters: PVP and ethanol (85:15), v = 20 kv, d = 25 cm, and m = 2.5 ml/hr.

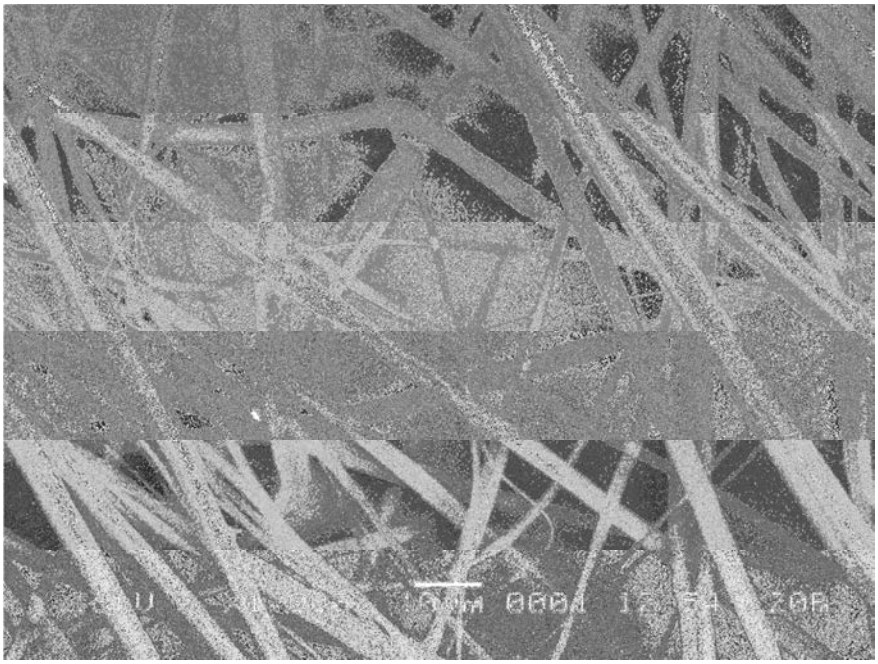

Figure 3-12. SEM image of PVP fibers produced with processing parameters: PVP and ethanol (85:15), 1/2% MWCNTs, v = 18 kv, d = 15 cm, and m = 3 ml/hr.

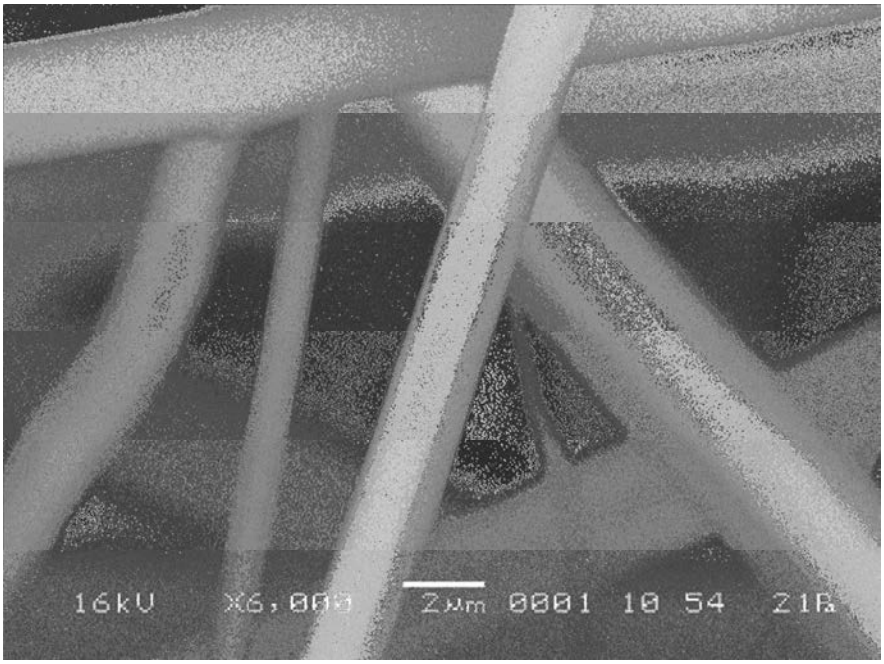

Figure 3-13. SEM image of PVP fibers produced with processing parameters: PVP and ethanol (85:15), 2% MWCNTs, v = 18 kv, d = 15 cm, and m = 3 ml /hr.

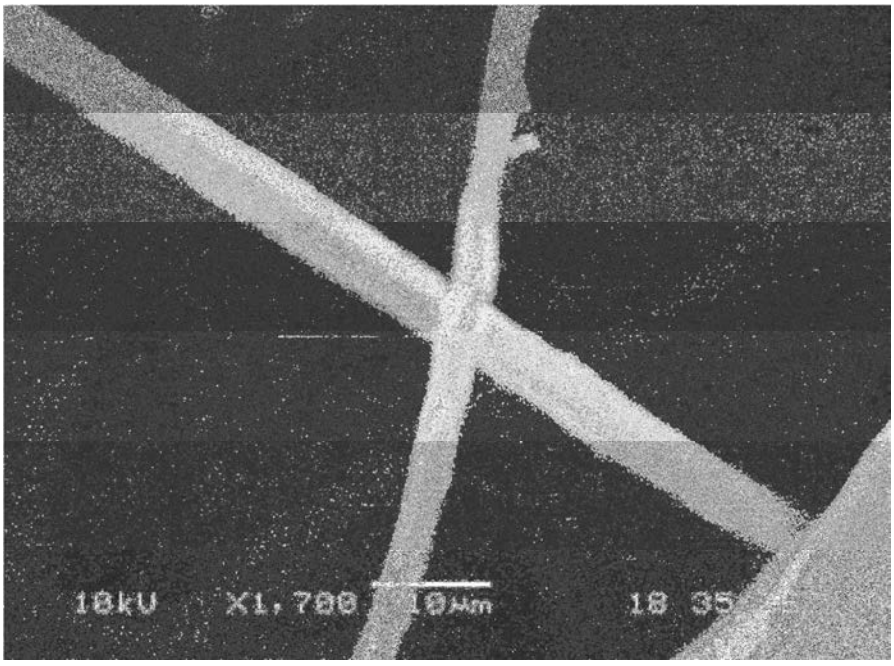

Figure 3-14. SEM image of PVP fibers produced with processing parameters: PVP and ethanol (85:15), 4% MWCNTs, v = 18 kv, d = 15 cm, and m = 3 ml/hr.

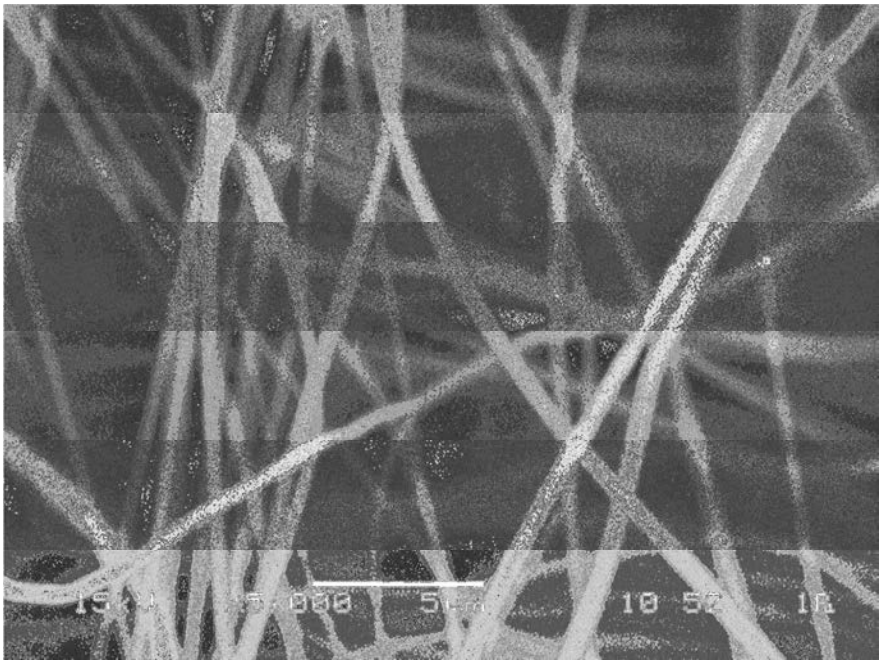

Figure 3-15. SEM image of PAN fibers produced with processing parameters: PAN and DMF (90:10), 0% MWCNTs, v = 25 kv, d = 25 cm, and m = 1 ml /hr.

Figure 3-16. SEM image of PAN fibers produced with processing parameters: PAN and DMF (90:10), 1% MWCNTs, v = 25 kv, d = 25 cm, and m = 1 ml/hr.

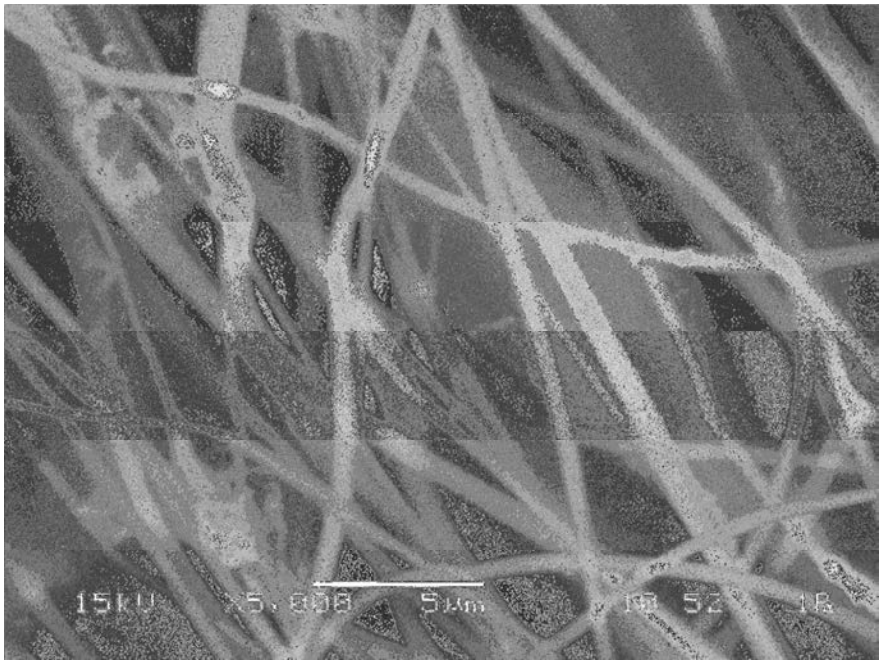

Figure 3-17. SEM image of PAN fibers produced with processing parameters: PAN and DMF (90:10), 4% MWCNTs, v = 25 kv, d = 25 cm, and m =2 .5 ml/hr.

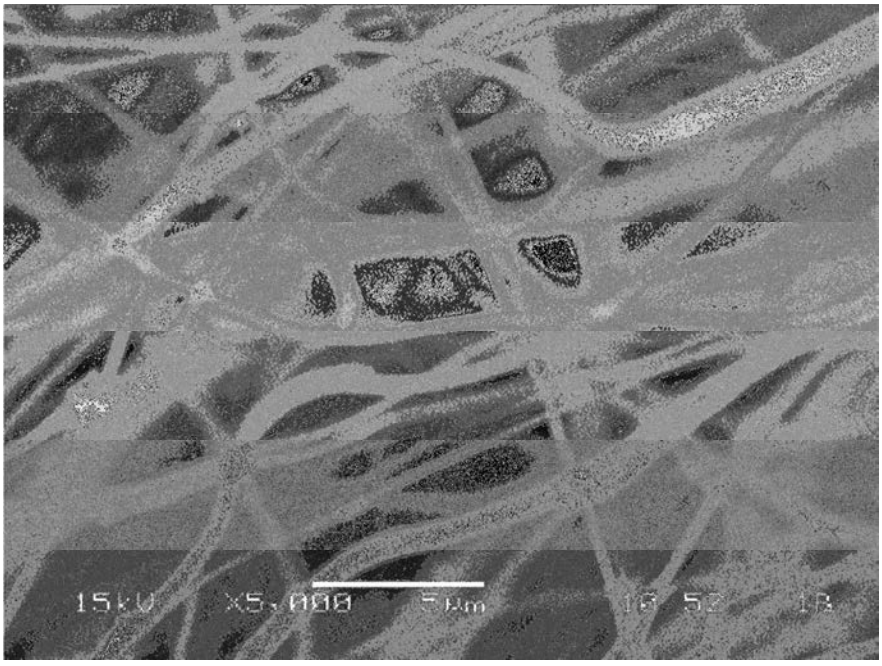

Figure 3-18. SEM image of PAN fibers produced with processing parameters: PAN and DMF (90:10), 10% MWCNTs, v = 28 kv, d = 25 cm and m = 3 ml /hr.

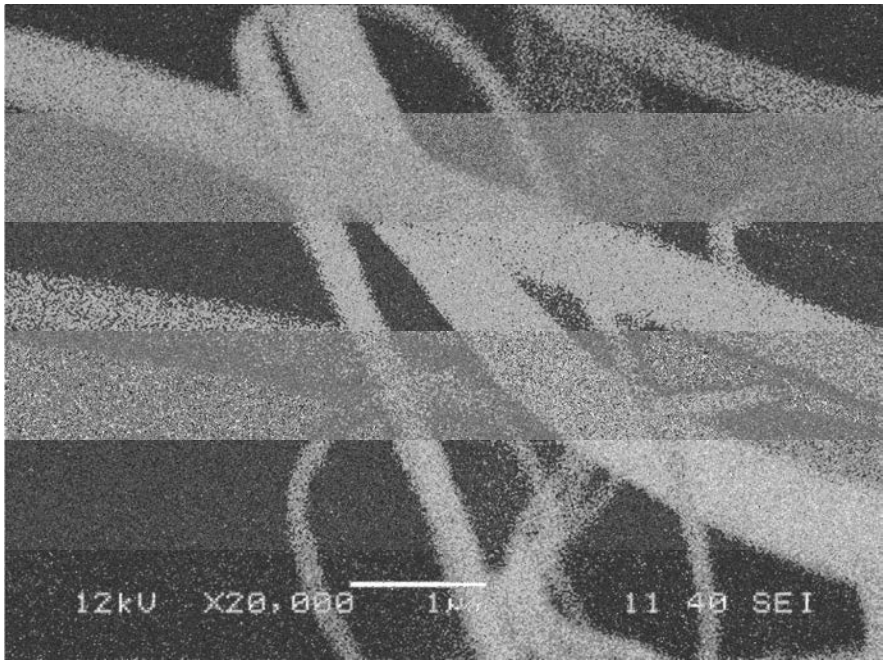

Figure 3-19. SEM image of PAN fibers produced with processing parameters: PAN and DMF (95:05), 15% MWCNTs, v = 28 kv, d = 30 cm, and m = 3.5 ml /hr.

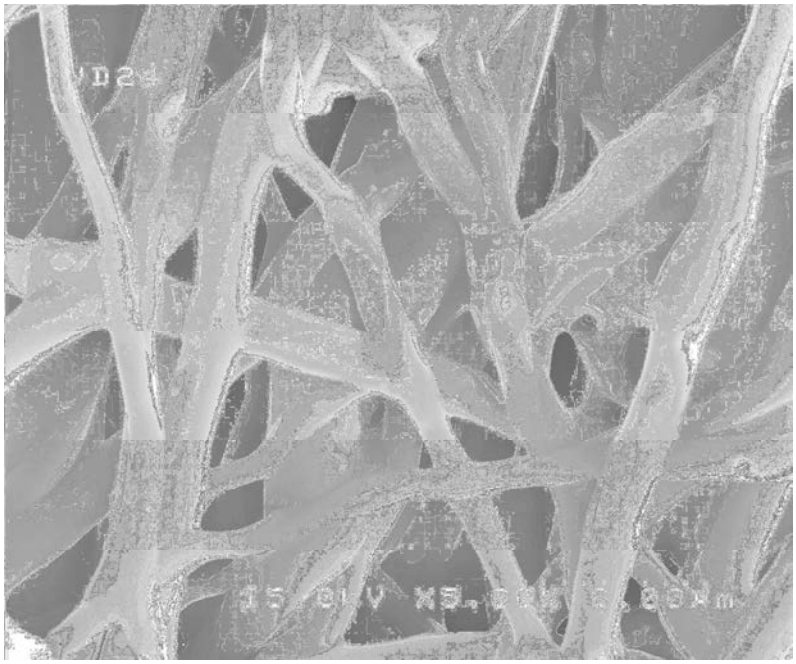

Figure 3-20. SEM image of PVP fibers produced with processing parameters: PVP and ethanol (90:10), 4% $NiZnFe_2O_4$, v = 25 kv, d = 25 cm, and m = 2.5 ml /hr.

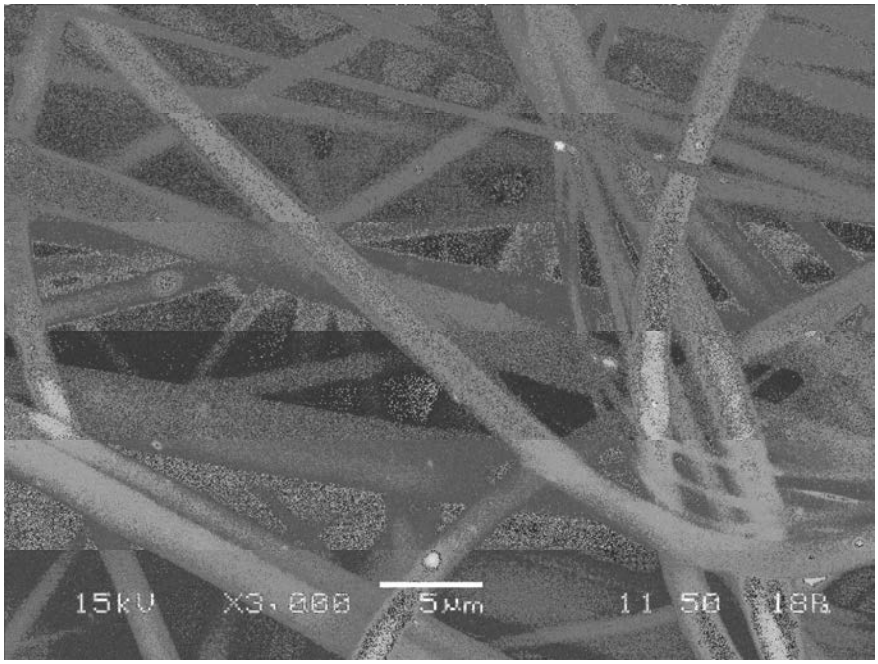

Figure 3-21. SEM image of PVP fibers produced with processing parameters: PVP and ethanol (90:10), 8% $NiZnFe_2O_4$, v = 25 kv, d = 25 cm, and m = 2.5 ml/hr.

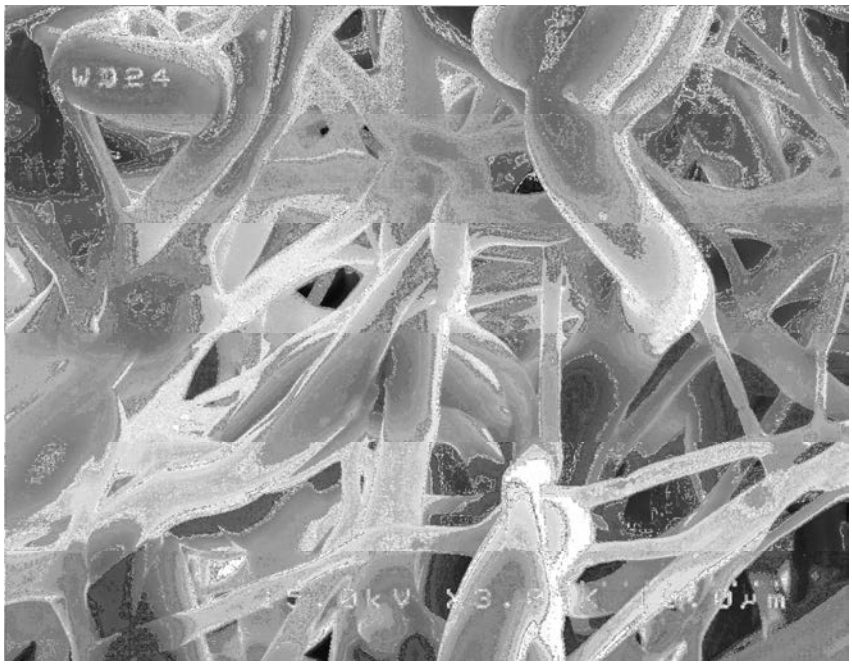

Figure 3-22. SEM image of PVP fibers produced with processing parameters: PVP and ethanol (90:10), 16% $NiZnFe_2O_4$, v = 25 kv, d = 25 cm, and m = 2.5 ml/hr.

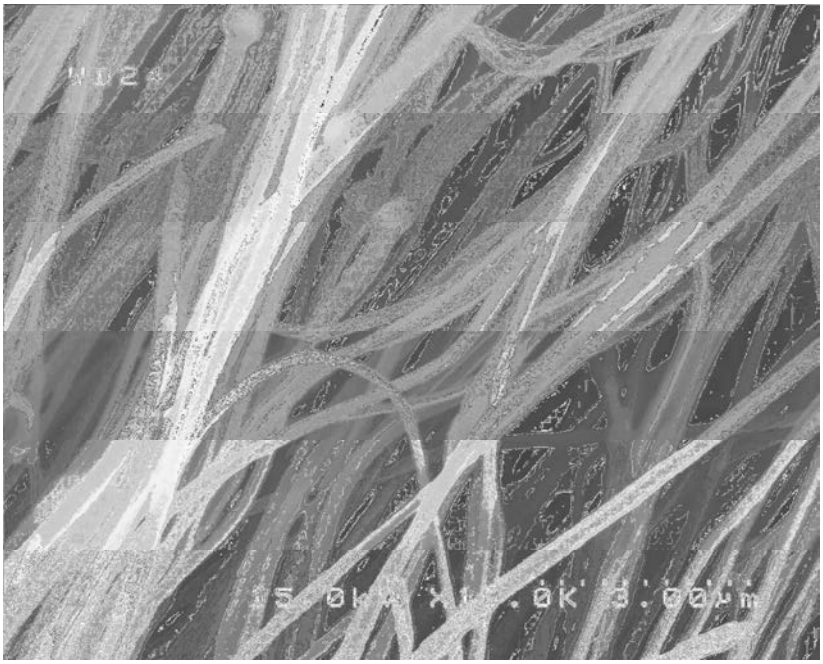

Figure 3-23. SEM image of PAN fibers produced with processing parameters: PAN and DMF (90:10), 4% $NiZnFe_2O_4$, v = 25 kv, d = 25 cm, and m = 2.5 ml/hr.

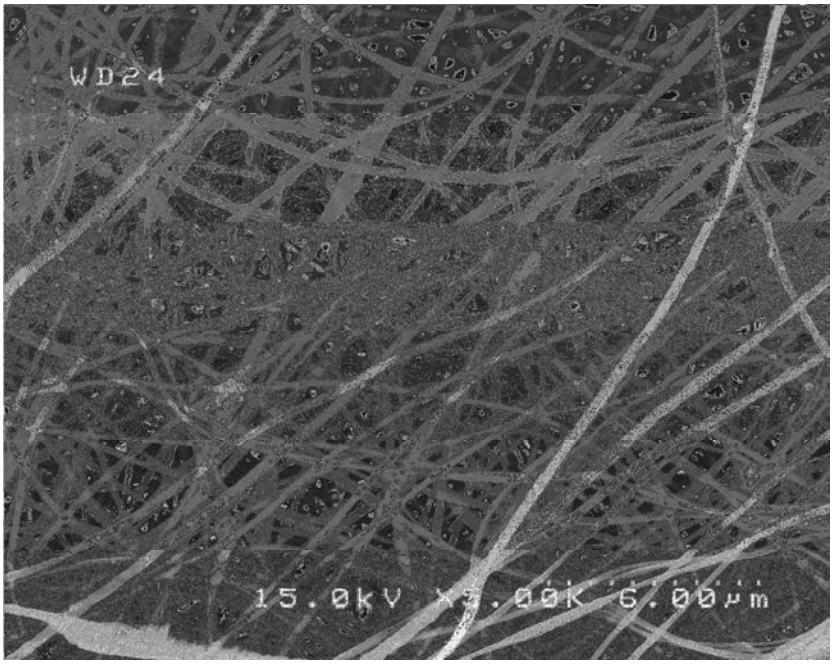

Figure 3-24. SEM image of PAN fibers produced with processing parameters: PAN and DMF (90:10), 16% $NiZnFe_2O_4$, v = 25 kv, d = 25 cm, and m = 2.5 ml/hr.

Atomic force microscopy was also used to determine the diameter of electrospun fibers. Figures 3-25 to 3-27 show the AFM images of electrospun fibers.

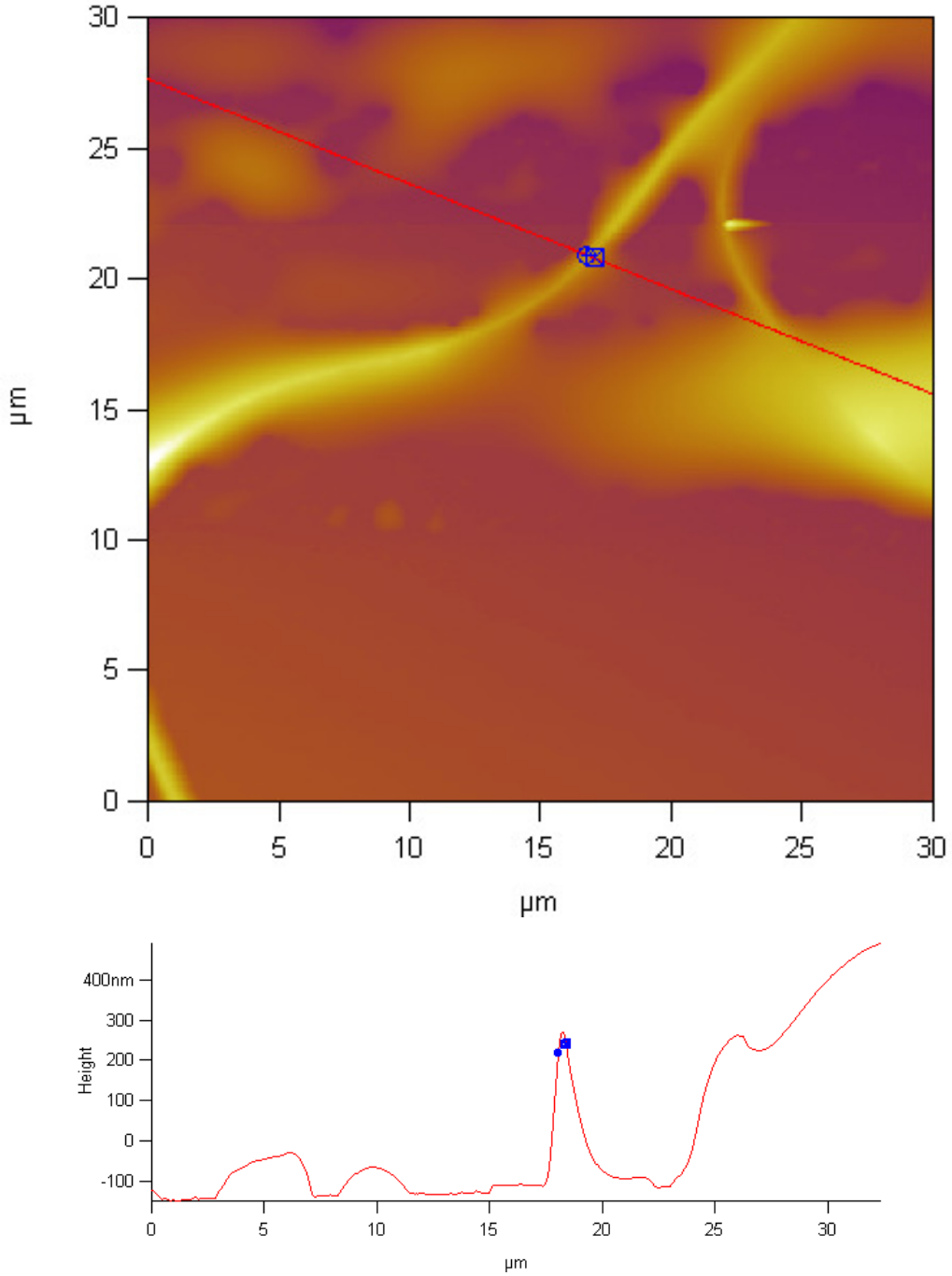

Figure 3-25. AFM images of PAN fibers produced with processing parameters: PAN and DMF (90:10), 2% $NiZnFe_2O_4$, v = 15 kv, d = 25 cm, and m = 1 ml /hr.

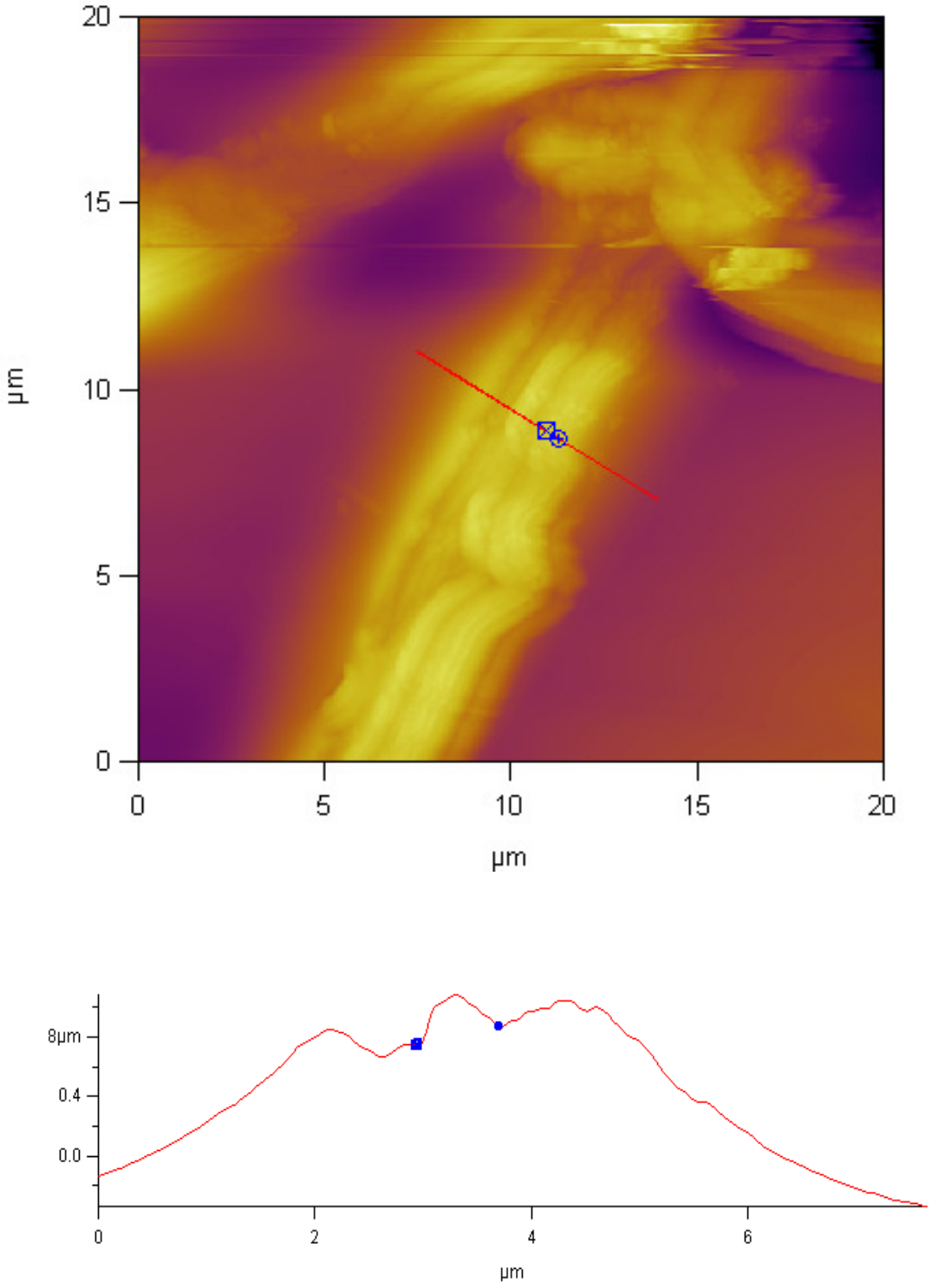

Figure 3-26 AFM images of PAN fibers produced with processing parameters: PAN and DMF (90:10), 8% $NiZnFe_2O_4$, v = 25 kv, d = 25 cm, and m = 2.5 ml /hr.

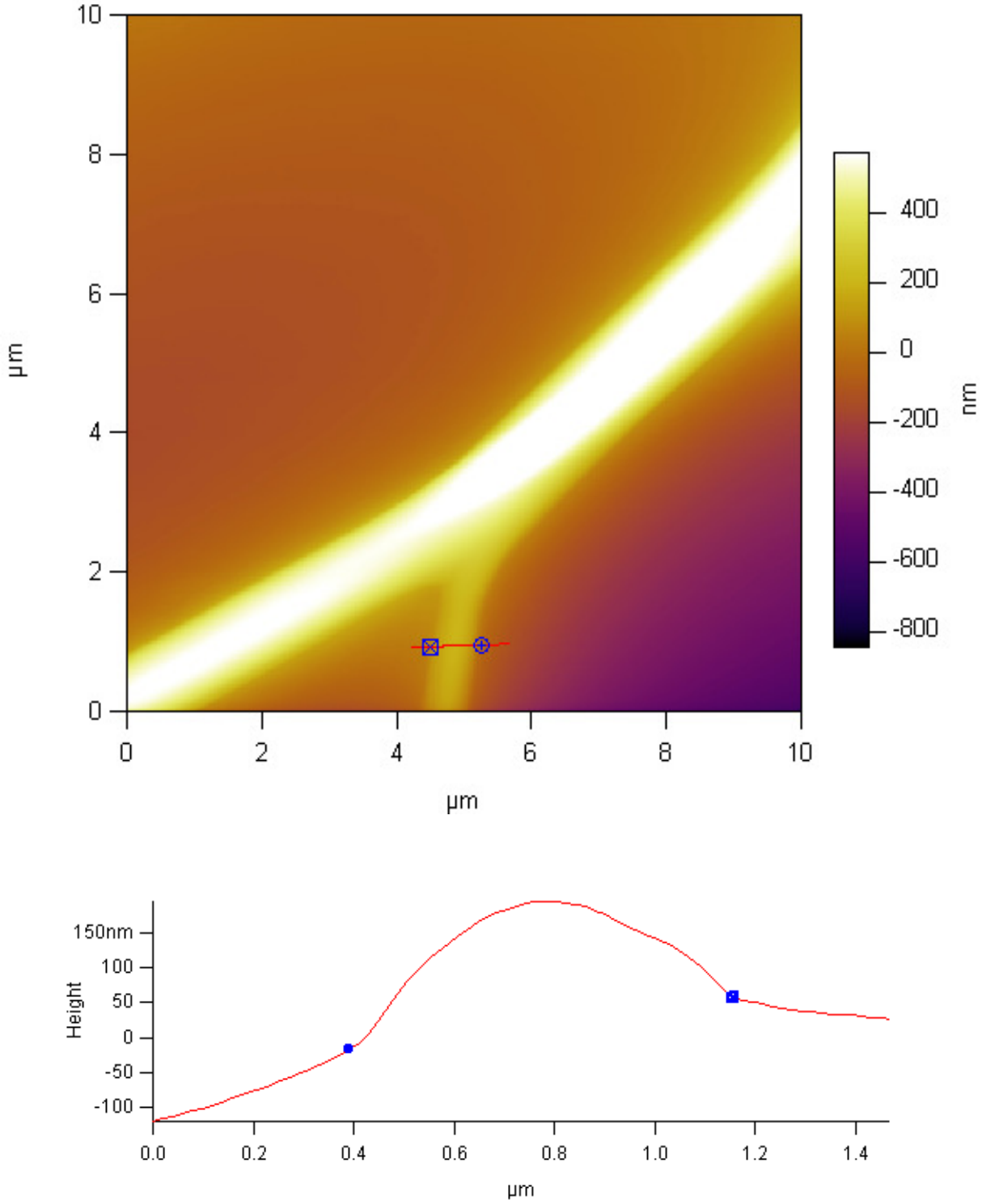

Figure 3-27. AFM images of PVP fibers produced with processing parameters: PVP and Ethanol (90:10), 16% $NiZnFe_2O_4$, v = 2 5kv, d = 25 cm, and m = 2.5 ml /hr.

3.9 Structure of the Electrospun Fibers

Electrospinning usually produces fibers of submicron size. However, if the processing parameters are not controlled properly, micron size fibers are produced by electrospinning. After the evaporation of the solvent, the molecules of the polymer come together and solidify during the nucleation and growth process. The structure of the polymer deposited on the collector screen consists of mostly amorphous, some semi-crystalline, and oriented or spherulitic structures. In electrospinning, growth and nucleation occurs rapidly, and therefore, this high kinetic lowers the crystallinity of the polymer [66].

3.10 Parameters Affecting Electrospun Fibers

Two types of parameters affect the morphology of electrospun nanofibers:

- System Parameters
  - Polymer and solvent types
  - Viscosity, conductivity, and surface tension of polymers
- Process Parameters
  - Electric potential, flow rate, and polymer concentration
  - Distance between capillary and collection screen
  - Temperature, humidity, and air velocity effects in the chamber

3.10.1 System Parameters

Nearly all kind of polymers can be electrospun in different solvents. The polymer for electrospinning should have moderate molecular weight. If the molecular weight is too high, then electrospinng will be very difficult. If it is too low, electrospinng will result in spherical and beaded structures. The solvent should be such that it can dissolve polymer easily.

Viscosity plays a major role in electrospinning and significantly influences the diameters of electrospun fibers. Electrospining depends on rheological properties of the polymeric solution. Increasing the viscosity of the solution reduces the formation of beads and increases the fiber diameter. If the viscosity is above 20 poise, electrospinning becomes impossible because of the instability of flow caused by the cohesivity of the solution. Droplets form when the viscosity is low (< 1 Poise). The solution should be conductive. If it is not, then calcium chloride is added to make it conductive. When the conductivity of the solution is high, the resulting electrospun fibers will have small diameters. Beads and pores are observed, when the conductivity of the solution is low. When the surface tension of the polymeric solution is low, the nanofiber does not have beads and pores. Surface tension should not be too low or too high for electrospinning, but should be a compromise between the two in order to have fibers in the nano range.

3.10.2 Process Parameters

The diameter electrospinning jet becomes smaller as it progresses to the target because of evaporation of the solvent and continuous stretching of the jet due to the electrostatic forces. The fiber diameter decreases as the applied electrical potential increases. An increase in the applied electrical potential increases the field strength, which in turn accelerates changes in the electrified jet and instability region, and as a result, the fibers produced are submicron in size. The drift velocity of the charge carriers is related to mobility of charge carriers by [8]

$$u = \mu_i V \tag{3.25}$$

where "u" is the drift velocity, "μ_i" is the mobility of charge carriers, and "V" is the applied field. The morphology of the fibers depends upon the flow rate of the solution. When the flow rate is exceeded, fibers surrounded with beads and pores are produced. The polymer concentration should be a compromise between minimum and maximum. If the polymer

concentration is too high, then a beaded structure is observed. The diameter of electrospun fibers increases as the polymer concentration increases. The shape of the beaded structure changes from spherical to spindle, when the polymer concentration increases (high viscosity). A higher polymer concentration will result in a large fiber diameter. When the molecular weight is high, viscosity will be high and electrospinning will result in beaded structure.

The fiber diameter reduces as the distance between capillary and collection screen increases. When this distance is too small, a beaded structure with a larger diameter is observed.

The electrospinning process is usually carried out at room temperature under normal conditions. However, if the temperature is higher than the room temperature, then the evaporation rate will be high, and this will help in reducing the fiber diameter. Some researchers use dehumidifiers to control humidify and produce fibers in nanoscale. High airflow will increase the evaporation rate due to convection and will help in reducing fiber diameter.

3.11 Summary

In this chapter, the electrospinning process was discussed extensively, and various process and system parameters were outlined. The polymers and solvents used in this study were mentioned.

Mathematical models were developed for jet initiation and bending instability of the electrified jet. The structures and features of nano inclusions (MWCNTs and NiZn ferrites) were also outlined.

CHAPTER 4

DIELECTRIC PROPERTIES OF NANOCOMPOSITE FIBERS

4.1 Introduction

The dielectric constant is an important electrical property and helps in understanding the basis of crystal physics [78]. Measurement of the dielectric constant as a function of temperature assists in the electrical characterization of the material. Every material has some unique electrical characteristics that are dependent on its dielectric properties. Measurements of these properties can provide useful data to apply to materials that are used in different industrial applications. Measurement of the dielectric constant can provide critical design information for many electronics applications, such as the loss of a cable insulator, the impedance of a substrate, or the high frequency of a dielectric resonator. The dielectric properties of polymers are very important in many industrial applications, such as cable insulation, encapsulants for electronic components, wiring board materials, etc.

4.2 Motivation and Objectives

Dielectric materials are used in almost all electrical equipment. They have low conduction and are capable of storing a charge. Dielectric materials can be in the form of either a solid, liquid, or gas. Generally, solid materials are dielectric. PAN and PVP polymers are insulators, and generally insulators are good dielectric materials. This chapter discusses the determination of dielectric properties of PAN and PVP fibers at different temperatures in order to explore the possibility of using them as dielectric materials in the electrical and computer industries.

4.3 Molecular Origins of Permittivity

A polar molecule has a permanent dipole moment, meaning that it has the same amount of positive and negative charge; therefore, the molecules are neutral and the distribution of these charges is not symmetrical. The positive and negative charges are centered at a point separated by a distance that is on the order of a molecular dimension, thus making a dipole. Considering that the dipole is made up of charges ($+q\ and\ -q$) separated by a distance d_1, then the dipole moment is qd_1 [79]. The magnitude of the dipole moment depends on the size, orientation, and symmetry of the molecule. The dipole moment of a material greatly influences the dielectric constant. A material is said to be dielectric if it has the capability of storing energy when an external electric field is applied. The extent to which a material responds to an applied electrostatic field can be determined in the case of a parallel plate capacitor, as shown in Figure 4-1.

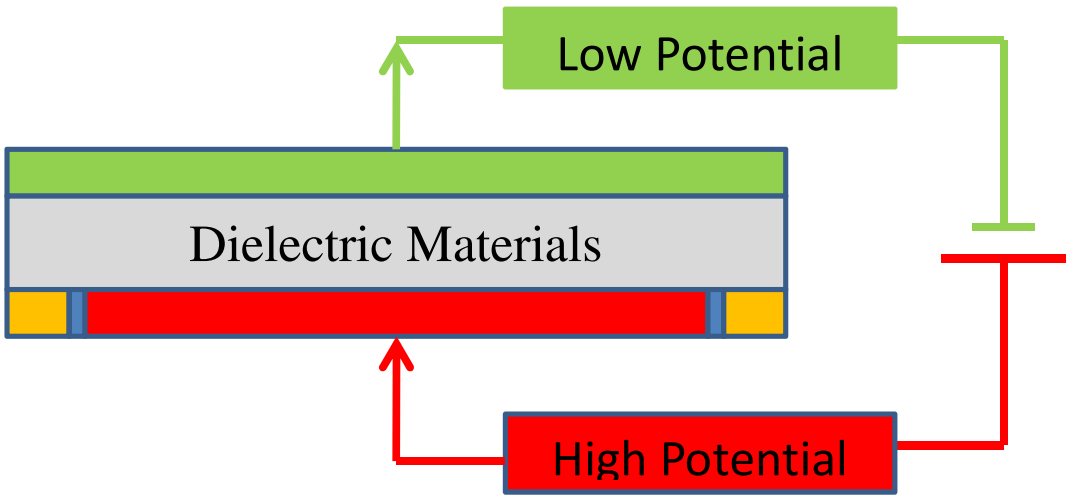

Figure 4-1. Parallel plate capacitor.

If a voltage (V) is applied across such a capacitor and the plates are separated by a distance (d_1), then the electric field (E) produced can be determined by [79].

$$E = V/d_1 \tag{4.1}$$

The charges $+q\ and\ -q$ stored on the plates are proportional to the magnitude of the electrical field (E) [79] as

$$Q = \epsilon_0 E \tag{4.2}$$

The constant of proportionality is called the permittivity of the free space and has a value of about 8.854 x 10^{-12} F/m. The vacuum capacitance per unit area of electrode C_0 can be defined by the ratio of stored charge to the applied voltage [79] as

$$C_0 = Q/V \tag{4.3}$$

When the electric field is applied, the material will be polarized. The positive charge will be attracted by the negative electrode, and the negative charge will be attracted by the positive electrode. If the material is isotropic, the effect will be the production of a small dipole moment pdv aligned in the field direction in each elemental volume dv. The polarization can be defined by a vector expressing the direction and magnitude of the electric moment per unit volume induced in the material by the applied electric field. Each small volume element in a polarized material will behave electrically and will consist of charges $+q\ and\ -q$ separated by a distance I in the field direction, giving a dipole moment $QI = Pdv$. These dipoles will combine to produce $+p\ and\ -p$ per unit area on the surface of the electrodes. The field as the result of uniform polarization (P) in a material is equivalent to that from distribution of charges p_n on the bond surface, where p_n is the normal component of the polarization at the surface. The presence of this polarization means that more charges can be stored on the capacitor electrodes for the same applied field, and thereby the capacitance of the system can be increased [80]. The ratio ϵ of the increased capacitance to the vacuum capacitance can be given by

$$\epsilon = \frac{C}{C_0} = (Q + P)/Q \tag{4.4}$$

This characteristic ratio has different values for different materials and depends upon the polarization of the material. It is independent of the applied field and is commonly known as the dielectric constant (relative permittivity) of the material. Substituting for Q from equation (4.2) into equation (4.4) and using the vector notation,

$$\epsilon = (\epsilon_0 E + P)/\epsilon_0 E$$

$$= 1 + P/\epsilon_0 E$$

$$= 1 + X \tag{4.5}$$

where $X = P/\epsilon_0 E$ is the electric susceptibility of the material. The quantity $\epsilon\epsilon_0 E$ is called the electric displacement D in the material and can be obtained as [80]

$$D = \epsilon\epsilon_0 E = \epsilon_0 E + P \tag{4.6}$$

The quantity $\epsilon\epsilon_0$is the absolute permittivity of the material, and the ratio $\epsilon = C/C_0$ is called the relative permittivity of the material. The dielectric material increases the storage capacity of the capacitor by neutralizing charges at the electrodes, which probably contribute to the applied field. The capacitance with the dielectric material is related to the dielectric constant. The dielectric constant ϵ_r can be obtained from the measured capacitance C with the help of the electrodes area A, the layer thickness d, and the vacuum dielectric constant ϵ_0, by using

$$\epsilon_r = C.\frac{d}{A.\epsilon_0} \tag{4.7}$$

When the permittivity of the material is high, the polarizability of the molecules will be high too. In a non-polar molecule, this polarizability arises from two effects: the electric field, which causes a displacement of the electrons relative to the nucleus in each atom (electronic polarization), and the displacement of the atoms' nuclei relative to one another (atomic polarization), the effect of the former generally being greater [79].

4.4 Electronic Polarization

An applied field (electric) that causes a small displacement of electrons of any atoms with respect to the nucleus is called electronic polarization. This shift is small because the applied field is usually very weak relative to the intra-atomic field of an atom due to the nucleus. If the charge on a proton is around 1.6×10^{-19} C and a typical atomic radius is around 10^{-11} m, then the electric field on an electron will be on the order of 10^{8} Vm^{-1}. Electronic polarization can occur at very high frequencies and can be responsible for light refraction [79].

4.5 Atomic Polarization

An electric field can also distort the arrangement of atomic nuclei in a molecule or lattice. The movement of heavy nuclei is slower than that of electrons. Therefore, atomic polarization cannot take place at high frequency, whereas electronic polarization can take place at high frequency. The magnitude of atomic polarization is usually small, often one-tenth of that of electronic polarization [79].

4.6 Orientation Polarization

If a polar molecule is used, a third process contributes to the polarizability. In the absence of an electric field, the permanent dipole moments of the molecules are randomly distributed in all directions and change direction constantly because of the thermal motion of the molecules. Since an electric field is applied, there is a tendency for the permanent dipoles to align themselves parallel to it because of the thermal motion; the departure from a random arrangement is very small in fields of the size normally used for measurement and at ordinary temperatures. This orientation polarization is in addition to electronic and atomic polarization, and collectively is called distortion polarization. The internal electric field varies from point to point due to field interactions from the dipoles, which are induced on each molecule by the

applied field. The field acting on an individual polarizable entity like an atom or molecule is called the local field and is an important concept in linking observable bulk behavior of a material with the properties of its constituent atoms or molecules. The local field can be divided into two components [80] as

$$E_L = E_C + \sum E_D \tag{4.8}$$

where "E_C" is the field due to real charges on the electrodes that sustain the externally applied field, and "$\sum E_D$" is the sum of fields from all molecular dipoles apart from that on the molecules at the reference point within the sample. A general evaluation is difficult because the sum "$\sum E_D$" does not converge for an infinitely large sample, and it depends on the shape of the sample.

Polar polymers generally have higher permittivity than non-polar polymers. The temperature dependence of the permittivity of polar polymers also differs from that of the non-polar polymers. In non-polar polymers, change of temperature has only a small effect, which can be accounted for by the change in density; but in polar polymers, the orientation polarization falls off rapidly with rising temperature, because the increasing thermal motion reduces the alignment of the permanent dipoles by the electric field. For this reason, the permittivity of a polar polymer falls more rapidly with increasing temperature than that of a non-polar polymer. The relationship between permittivity and the various types of polarization can be expressed quantitatively, whereby permittivity is given in terms of the polarization "P" produced by an applied field "E" by [79]

$$\epsilon_0 = 1 + (4\pi P)/\epsilon E \tag{4.9}$$

where "ϵ" is a constant (dielectric constant) whose value depends upon the material used, and "P" is the intended surface charge density on the polymer and also the electric moment induced

per unit volume. Suppose that there are "N" molecules per unit volume and that the average moment induced in each of them, because of all types of polarization, is "$m,$" then [79]

$$P = Nm \tag{4.10}$$

If the average electric field acting on a molecule is F (different from the applied field E), then the average moment "m" will, for fields of the order of magnitude normally encountered, be proportional to F [79] as

$$m = F\alpha_T \tag{4.11}$$

where "α_T" is the total polarization of the molecules and

$$\alpha_T = \alpha_e + \alpha_a + \alpha_0 \tag{4.12}$$

where "$\alpha_e,$" "$\alpha_a,$" and "α_0" are the electronic, atomic, and dipole contributions, respectively, to the polarizability. Hence [79],

$$\epsilon_0 = (1 + 4\pi NF\alpha_T)/E\epsilon \tag{4.13}$$

Each of the three types of polarizability is a function of the frequency of the applied field

4.7 Experiment

The dried PVP and PAN nanofibers were sandwiched between two parallel metal plates forming a parallel-plate capacitor. These fibers were heated in a small furnace, and the capacitance values were measured using a TENMA 72-370 CRL meter. A K-type thermocouple thermometer, IDEAL 61-312, was used to measure the temperature of the nanofibers within the range of 23^0C to 90^0C. In this experiment, a constant frequency of 60 HZ was used.

4.8 Results and Discussions

In the first part of this experiment, the dielectric constants were measured with different wt% of MWCNTs and NiZn ferrites at room temperature, and in the second part of this

experiment, the dielectric constants were measured with varying temperatures. The dielectric properties of a polymer depends on the following factors.

- Temperature
- Frequency
- Structure and composition (polar and non-polar polymers)
- Inclusions, additives, plasticizers, moisture, and filler materials

The temperature and frequency dependencies of a dielectric constant rely upon whether the polymer is polar or non-polar. Non-polar polymers (hydrocarbon polymers) have low dielectric constant values as compared to polar polymers. In non-polar polymers, the dielectric values change very little with temperature and frequency. PAN and PVP are polar polymers, and they behave in a different way than non-polar polymers. The dielectric constants of polar polymers are very sensitive to moisture. Water molecules can incorporate into them. Water has a dielectric value of around 80 at room temperature. The incorporation of a very small amount of water can increase the dielectric constant of polar polymers to a significant level. The dielectric constant is also very sensitive to small amounts of impurities, additives, inclusions, and plasticizers. In this study, the MWCNTs and NiZn ferrites were used as inclusions, which increased the dielectric constants, as shown in Figures 4-2 (a), 4-2 (b), 4-3 (a), and 4-3 (b).

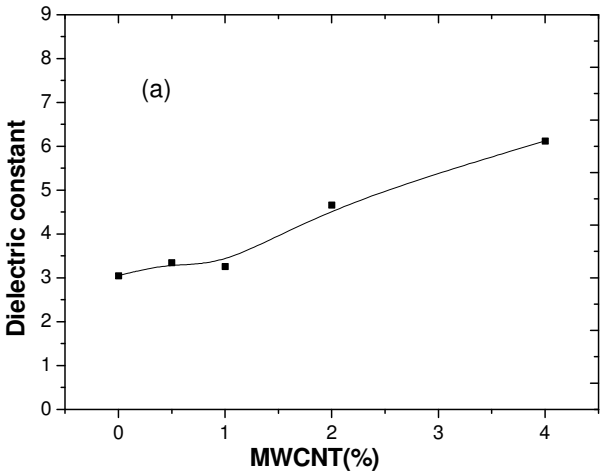

Figure 4-2 (a). Dielectric constant values of PVP fibers as function of MWCNTs concentration.

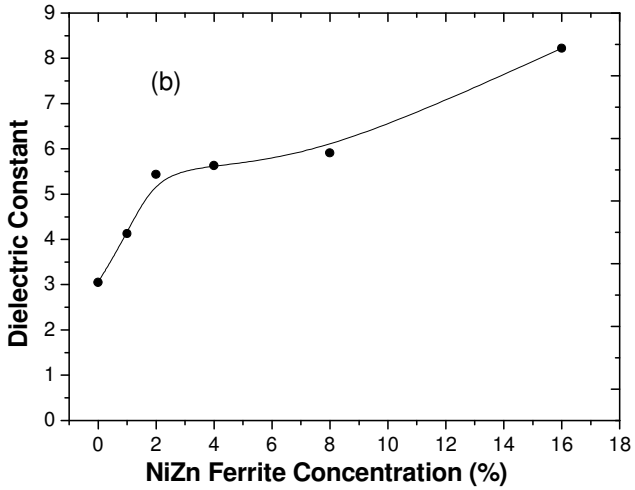

Figure 4-2 (b). Dielectric constant values of PVP fibers as function of NiZn-ferrite nanoparticle concentration.

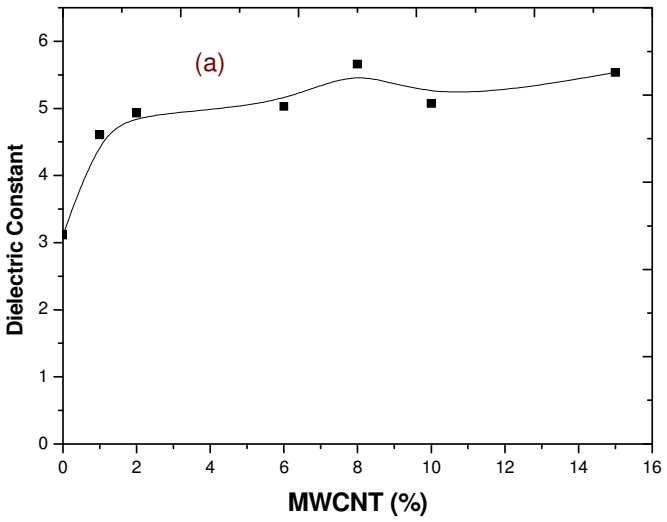

Figure 4-3 (a). Dielectric constant values of PAN fibers as function of MWCNTs concentration.

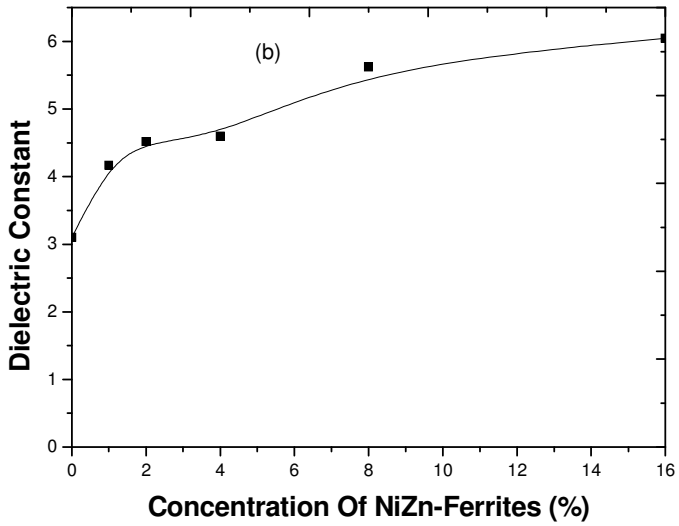

Figure 4-3 (b). Dielectric constant values of PAN fibers as function of NiZn-ferrite nanoparticle concentration.

MWCNTs absorb ethanol but do not absorb dimethylformamide. NiZn ferrites do not absorb either ethanol or DMF. Therefore, it is possible to add a high weight percentage of NiZn ferrites and MWCNTs in a PAN-based polymeric solution, but not a high weight percentage of MWCNTS in a PVP-based polymeric solution. In this study, only 4 wt% of MWCNTs was added to a PVP-based polymeric solution. If a higher wt% of MWCNTs is added to a PVP-based polymeric solution, it becomes highly viscous and difficult to electrospin. It is clear from Figures 4-2 (a), 4-2 (b), 4-3 (a), and 4-3 (b) that dielectric values increase as the wt% of MWCNTs and NiZn ferrites increases. It is well known that MWCNT and NiZn ferrites are conducting and semicoducting materials, respectively, while PVP and PAN are electrical insulators. This means that MWCNTs and NiZn ferrites have a higher free-charge concentration at room temperature than PVP and PAN fibers. This leads to increased polarizability of the nanocomposite fibers with the increasing wt% of MWCNTs and NiZn ferrite concentrations. The relationship between the dielectric constant "ε_r" and the molecular polarizability "α_t" is given by [81]

$$\varepsilon_r = 1 + (\frac{N\alpha_t}{\varepsilon_0}) \tag{4.14}$$

where "N" is the concentration of molecules, and "ε_0" is the permittivity of free space. According to this relationship, the dielectric constant has to increase by increasing the polarizability. In this experiment, the dielectric readings were taken on the assumption of uniform thickness of the sample, uniform dispersion of MWCNTs and NiZn ferrite nanoparticles, and no moisture present in the samples. These factors certainly change the dielectric properties to a significant extent. Apart from these factors, porosity and air pockets present in the fiber texture also play an important role in altering the dielectric properties of nanocomposite fibers. The value of the dielectric constant of material in fibrous form is lower than that in bulk form because of air pockets present in the fiber texture. Polar polymers have a tendency to absorb moisture from the atmosphere; therefore, the presence of moisture generally raises the dielectric constant. In the second part of this study, dielectric constants were measured at different temperatures.

From Figure 4-4, it is obvious that PVP fibers have no significant effect on their dielectric properties as the temperature increases. It is noticeable that MWCNTs have thermal stability in dielectric properties until 50^0C, and then the dielectric constant decreases as the temperature increases up to 80^0C and above. This reveals that the addition of MWCNT to PVP fibers did not change the temperature dependence profile, which could be attributed to the inconsiderable change of polarizability with temperature due to the constant charge-carrier concentration with temperature. PVP fibers have polar tendency. In polar polymers, the orientation polarization falls off rapidly with rising temperature, because the increasing thermal motion reduces the alignment of the permanent dipoles by the electric field. For this reason, the permittivity of a polar polymer falls more rapidly with increasing temperature, and therefore, the dielectric constant decreases.

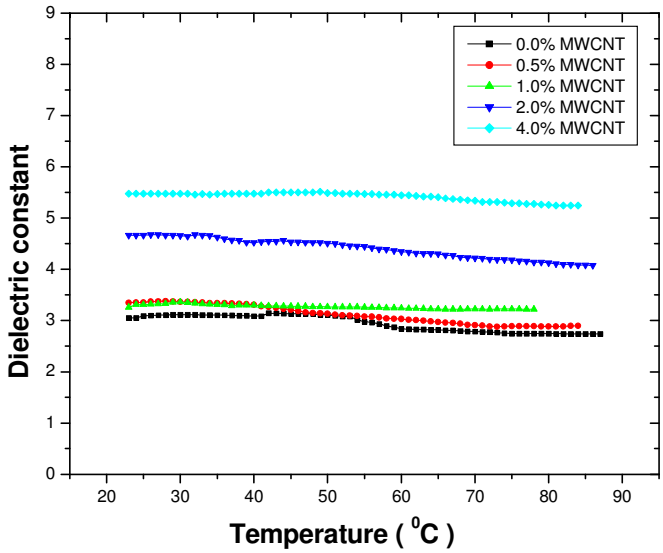

Figure 4-4. Dielectric constant values of PVP nanocomposite as function of MWCNTs and temperature.

The addition of NiZn ferrites to PVP fibers does not seem to improve the dielectric properties. At higher wt% (8 and 16) of NiZn ferrites, the dielectric constant (Figure 4-5) shows some improvement. At higher wt% of NiZn ferrites, there are more charge carriers, and as the temperature increases, the mobility of these charge carriers increases, as well. This helps to improve the dielectric properties of PVP fibers to some extent. This behavior may be attributed to the increase of polarizability of NiZn ferrite particles in nanofibers due to the increase of charge-carrier concentration (electrons) in NiZn ferrite particles since these ferrites are n-type semiconductors. It is well known that in the temperature range 25^0C–100^0C, the concentration of free electrons increases as the temperature increases. If the temperature increases, the atoms oscillate with high energy and transfer kinetic energy to neighboring atoms, and heat conduction takes place. The charge-carrier mobility increases as the temperature increases, and this helps to speed conduction. However, the orientation polarization decreases as the temperature increases, and therefore the dielectric constant does not have any significant effect as the temperature

increases. The glass transition temperature (T_g) of PVP is 105^0C, and in polar polymers, the dielectric constant generally increases after T_g. Since the dielectric readings were taken up to 90^0C, no improvement in the dielectric constant was observed.

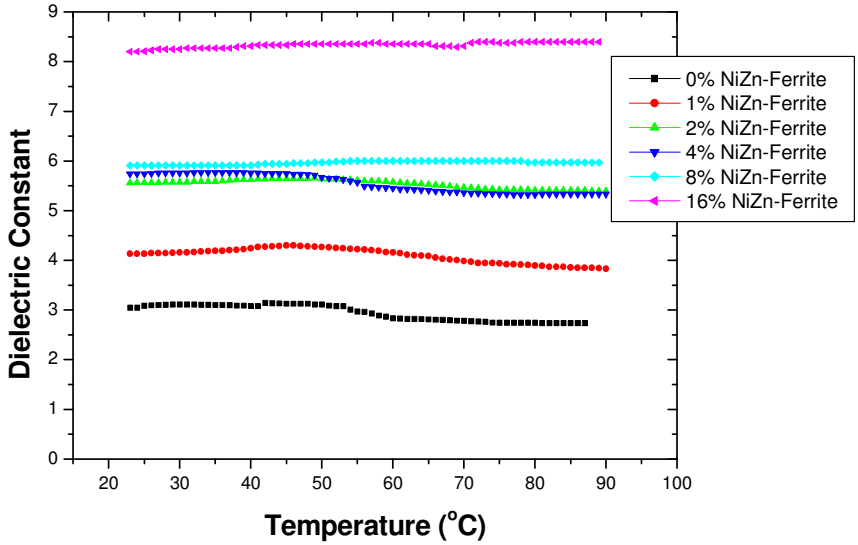

Figure 4-5. Dielectric constants of PVP fibers with different wt% of NiZn-ferrite vs. temperature.

In PAN fibers, the dielectric properties show some improvement as the temperature increases. PAN is a polar polymer. In a polar polymer, dipoles are created by an imbalance in the distribution of electrons and in the presence of an electric field, whereby the dipoles will attempt to move to align with the field. This will create "dipole polarization or orientation polarization" of the material, and because movement of the dipoles is involved, a time element is added to the movement of the induced dipole. For polar polymers, the alternating current frequency is an important factor because of the time taken to align the polar dipoles. At very low frequencies, the dipoles have sufficient time to align with the field before the field changes directions and the dielectric constant is high. At very high frequencies, the dipoles do not have sufficient time to align before the field changes directions and the dielectric constant is low. At intermediate frequencies, the dipoles move but have not completed their movement before the field changes direction and they must realign with the changed field. Generally, polar polymers have dielectric

constants between 3 and 9 at low frequencies (60 Hz) and between 3 and 5 at high frequencies. Raising the temperature of the PAN polymer allows faster movement of polymer chains and faster alignment of the dipoles; therefore, the dielectric constant increases. This is particularly true if the temperature is raised above the glass transition temperature. The T_g of PAN is 85^0C, and it is obvious from Figures 4-6 and 4-7 that the dielectric constant increases after 85^0C.

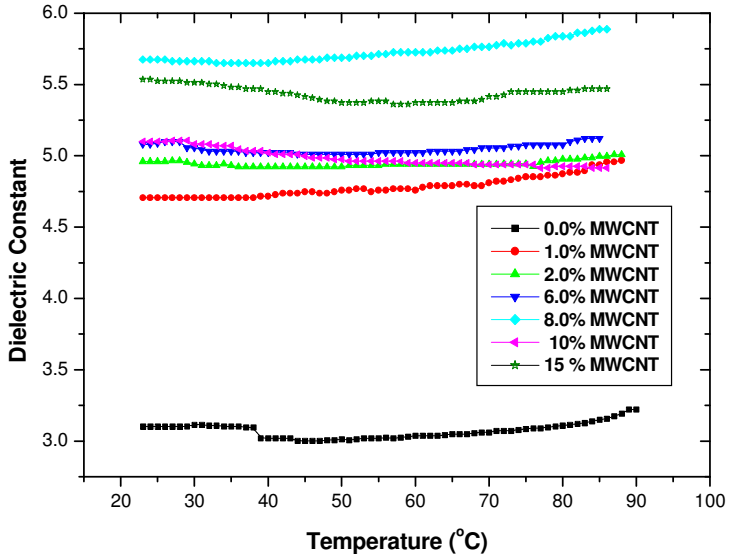

Figure 4-6. . Dielectric constant values of PAN nanocomposite as function of MWCNTs and temperature.

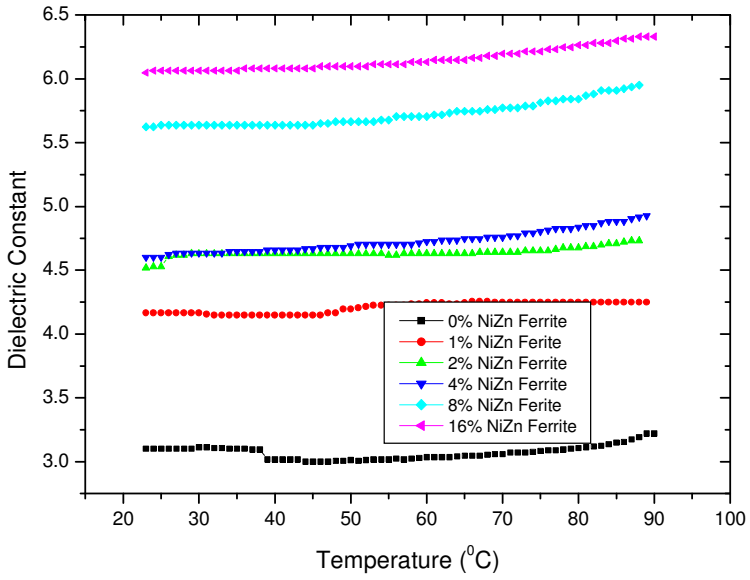

Figure 4-7. Dielectric constants of PAN fibers with different wt% of NiZn-ferrite vs. temperature.

The PAN-NiZn ferrites fibers behave more or less in the same way as PAN-MWCNT fibers. The dielectric constant increases as the temperature increases because at high temperature and at high wt% of NiZn ferrites, the concentration of charge carriers increases and so does the mobility of the charge carriers.

4.9 Empirical Relation

The critical spinning voltage for electrospinning as calculated in Chapter 1, equation (1.2) is

$$V_C = \sqrt{\frac{\gamma H^2}{r\epsilon}}$$

The critical spinning voltage according to Talyor [1, 5] from Chapter 3, equation (3.24) is

$$V_c^2 = 4H^2/L^2 \left(\ln\frac{2L}{R} - 3/2\right)(0.117\pi\gamma R)$$

Balancing equations 1.2 and 3.24 yields

$$\frac{0.6779\,L^2}{r.\epsilon.R} = \ln(2L/R) - 3/2 \tag{4.15}$$

where "L" is the length of the capillary tube, "R" is the radius of the capillary tube, and "r" is the radius of the meniscus. Substituting typical experimental values of capillary tube length (L = 0.130 m) and capillary tube radius (R = 0.5 x 10^{-3} m) yields

$$r = \frac{4.8199}{\epsilon} \tag{4.16}$$

which means that if the radius of meniscus is known, then the permittivity of the polymeric solution can be determined, provided the radius is in millimeters.

The minimum spraying voltage, according to Hendricks [5], from Chapter 3, equation (3.23) is

$$V = 300\sqrt{20\pi\gamma r}$$

Balancing it with the critical voltage calculated in Chapter 1, equation (1.2),

$$\epsilon = {H^2}/{(\pi r^2 18000{,}00)} \tag{4.17}$$

If the radius of the cone "r" and separation distance"H" between capillary tube and collector screen are known, then the permittivity of the polymeric solution can be determined. In this study, the separation distance used was 25 cm. If this separation distance is put into equation (4.17), then another empirical equation forms as

$$r = \sqrt{\frac{1.1x10\text{^}-8}{\epsilon}} \tag{4.18}$$

4.10 Conclusions

The addition of MWCNTs and NiZn ferrites increases the polarizability of nanocomposite fibers, which leads to an increase in the dielectric constant of the material. The dielectric constant of polar polymers generally increases after the glass transition temperature;

therefore, no increase in the dielectric constant values in PVP fibers was observed, and some increase in the dielectric constant values in PAN fibers was observed.

CHAPTER 5

ELECTRIC RESISTANCE OF NANOCOMPOSITE FIBERS UNDER VARIOUS LOADS AND TEMPERATURES

5.1 Introduction

Load and temperature have a direct relationship to fiber resistance. When the load is applied on a film of fibers, the fibers and molecules of polymer move closer together, heat conduction becomes easy, and contact resistance greatly decreases. PVP and PAN fibers are good insulators. As temperature increases on the films of fibers held in a furnace, the resistance decreases exponentially. This is because at high temperatures, molecules vibrates and transfer translational and rotational energy to neighboring molecules, and the mobility of charge carriers increases. The rate at which the resistance decreases is increased by the addition of MWCNTs and NiZn ferrites. The increase of charge-carrier mobility with temperature is governed by [86]

$$\mu_t = \mu_o e^{\frac{-E_\mu}{RT}} \tag{5.1}$$

where "μ_t" is the mobility at temperature T (^{0}K), "E_μ" is the activation energy, "R" is Boltzmann's constant, and "μ_0" is a temperature-independent constant. In this chapter, the effects of compressive loading on fiber texture and the effects of temperature on electrical resistance on a film of fiber is discussed.

5.2 Motivation and Objectives

Nearly all kinds of polymers exhibit a glass transition temperature (T_g), an important parameter that determines the application of nearly all amorphous polymers. The properties of polymers are changed when they are heated to their T_g; therefore, the selection of a polymer for a particular application is based on its Tg. In this chapter, the effects of hysteresis, polarization,

and conduction mechanisms when fibers are subjected to the external loading and temperature are mentioned.

5.3 Hysteresis Effects

When a polymer is cooled down rapidly and then heated slowly, it follows different pattern, as shown in Figure 5-1. Consider a sample of polymer that is cooled down along the line 1, as shown in Figure 5-1, and then heated slowly; the rate at which it was cooled will follow the dotted line 2.

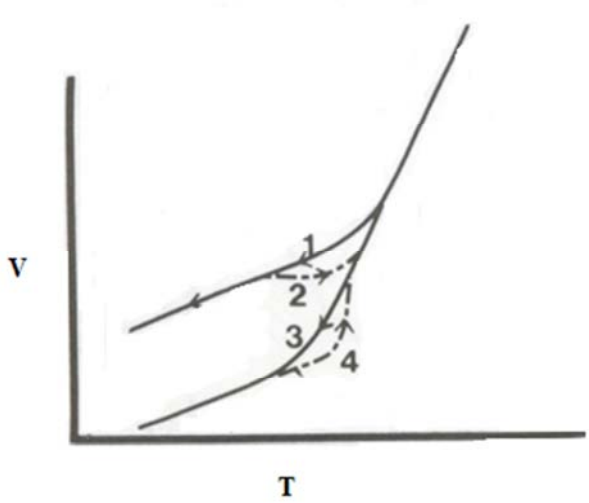

Figure 5-1. Hysteresis effects on volume-temperature plot [87].

While heating, the polymer has more time for it to adjust to its environmental conditions than when it is cooled down. The longer time results in volume shrinkage so that the volume of the polymer near glass transition temperature on heating is smaller than the volume at the same temperature on cooling. Storing the polymer for a longer period of time also results in volume shrinkage. When a polymer is cooled down very slowly and subsequently heated rapidly, the opposite trend is observed, as shown in Figure 5-1 (lines 3 and 4). A very rapid heating of a slowly cooled-down polymer results in over-shooting the glass transition temperature, which

leads to rapid expansion above the inflection point of the cooling curve. This rapid expansion causes hysteresis effects [87]. Hysteresis could be path dependent or rate independent.

5.4 Effects of Charge-Carrier Concentration

Charge carriers are free mobile particles carrying electrical charges. When MWCNTs and NiZn ferrite are added to polymers, the concentration of the charge carrier increases and, thus, conduction also increases. At higher temperatures, the mobility of the charge carrier increases, as well as conduction.

5.5 Polarizability

Increasing the wt% of MWCNTs and NiZn ferrite increase the dipole moments in polymers. Increasing the dipole moments increases the polarizability of the material and hence increases the conduction mechanism.

5.6 Effect of Porosity

Porosity is the amount of voids or empty spaces present in a material. This is an important physical property and affects almost all physical properties of the material.

5.7 Conduction Mechanism

Conductivity may be either ionic or electronic or both. It is very difficult to separate these types of conductivities experimentally, but the basic theoretical ideas are quite distinct and can be treated as such.

Ionic conductivity is simply the migration of positive and negative ions. The basic theoretical expression for all electrical conductivity is [88]

$$K_\rho = \sum n_i \, e_i \, \mu_i \tag{5.2}$$

where "n_i" is the density of charge carriers of the i th species, and "e_i" and "μ_i" are corresponding charges and mobility of charge carriers, respectively. Ionic conductivity can be expressed by [88]

$$K_\rho = K_0 e^{(-E_\mu/RT)} \tag{5.3}$$

where "K_0" and "E_μ" can be determined experimentally, "R" is the Boltzmann's constant, and "T" is the absolute temperature. Since both density and mobility of the charge carrier are temperature-dependent, the single temperature-dependent term in equation (5.3) combines the effects of temperature on both n_i and μ_i of equation (5.2). The ionic mobility depends greatly on temperature. The understanding of electronic conduction in polymers and solid arises from modifications to the quantum-mechanical band theory. This results in a picture of a solid in which a series of allowed electronic energy bands are completely occupied by electrons up to a certain level, and then empty thereafter. The conduction band does not give rise to any conduction since it contains no electrons, and the valence band does not conduct either since there are no unoccupied states into which an electron can be accelerated by an applied field. The isolated electronic energy level (i.e., electron traps) is actually the forbidden band. These trapping levels are caused by foreign ions, vacant lattice positions, and interstitials on the normal lattice field. The electrons are thermally excited into conduction levels and trapped there. The density of electron traps can be determined by the density of deformation of the lattice field. In reality, only the conduction and valence levels are important in pure, strain-free crystals at low temperature [88].

Understanding electronic conduction in terms of conduction bands and traps is not the only way to proceed, but in some circumstances, it is inappropriate [88]. In band theory, the effect of an applied electrical field is regarded as causing an acceleration of conduction electrons

in the band, and it may be appropriate to regard the electric field as causing transitions between adjacent but more or less localized states of the conducting electrons. This mechanism can be regarded as hopping conduction, and the conducting electrons can be regarded as making their way through the polymer in a series of discrete movements. Band conduction and hopping conduction are not regarded as the antithesis of each other; rather, the latter is a more appropriate visualization than the former in the limiting case of narrow bands.

These simple ideas of electronic conductivity fail in transition-metal oxides in a striking way. Some of these substances have only partially filled bands, yet they are highly insulating; others exhibit metallic conductivity at high temperatures but are insulating at low temperatures. Regardless of the theoretical model that is adopted to explain electrical conductivity in the insulating transition-metal oxides, the experimental data is adequately described in terms of activation energy with the conductivity given by equation (5.3).

The basic theoretical steady-state conduction equation is [88]

$$J = K_\rho F \tag{5.4}$$

where "J" is the current density, "F" is the field strength, and "K_ρ" the conductivity. The experimentally measured quantities are the current I and the voltage V. The easiest way to establish a connection between theory and the experiment is to write [88]

$$\left.\begin{aligned} J &= I/A \\ F &= V/d \end{aligned}\right\} \tag{5.5}$$

where "A" is the cross-sectional area, and "d" is the specimen thickness. Since the breakdown path usually only extends over a tiny fraction of the cross-sectional area, the current density in the breakdown channel is much higher than found by equation (5.5).

As is known, current-voltage characteristics present some practical problems. A steady-state condition requires a long period of time. It is well known that the relaxation time associated with the approach of a current distribution to the steady state is give by [88]

$$\tau = \epsilon/4\pi K_\rho \tag{5.6}$$

where "ϵ" is the dielectric constant, and "K_ρ" is the conductivity. If the current is due to charge carriers of different species, then the conductivity will be given by equation (5.2). In this case, there will be a relaxation time [88]

$$\tau_i = \epsilon/4\pi n_i e_i \mu_i \tag{5.7}$$

associated with each species of the charge carrier, and the eventual attainment of a steady state will be determined by the longest of the time constants in equation (5.7). It is readily verified that small concentrations of relatively immobile species may result in relaxation times of order of hours. This will not be important if the space-charge density due to carriers is so low as to cause negligible field distortion. The long time variation of the conduction process arises from possible carrier injection from the electrodes. The electrodes may be injected from a blocking contact at the cathode; these electrons may be trapped as they cross the material towards the anode, and this would cause a space charge tending to reduce injection from the contact. Gradual trapping of electrons at deeper levels could be associated with very long time constants, and the final steady state would depend, in a complex way, on the details of these processes. Injection of this type results in an electrical modification of the properties of the test sample. The sample becomes charged. An even more complex situation can arise if ionic species are injected from an electrode.

For low field strengths, ionic conductivity is always greater than corresponding electronic conductivity, which is true for all temperatures. At low temperatures, the ionic conductivity is

too small to cause more than infinitesimal heating of a solid, which will then withstand applied fields so strong that electronic conductivity becomes dominant. At high temperatures, the enhanced ionic conductivity plays a decisive role in the failure of a material before the field is sufficiently strong to cause appreciable enhancement of the electronic component.

5.8 Experiment

PVP and PAN nanocomposite fibers with various MWCNTs and NiZn ferrite nanoparticles were used in these experiments. The fibers were placed in a Carver laboratory press (Figure 5-2) and loaded up to 9 tons. Resistance was measured with a highly sensitive multimeter. In this temperature-resistance experiment, the fibers were placed in a furnace enclosed by insulation and heated by means of a D.C. power supply. Temperature versus resistance readings were taken [89].

Figure 5-2. Carver laboratory press [89].

5.9 Results and Discussions

5.9.1 Resistance of PVP and PAN Nanocomposite Fibers Under Load

PVP and PAN nanocomposite fibers with different weight percentages of MWCNTs were subjected to loading from 0 to 9 tons, and resistance was measured using two props with a circular cross section of diameter 2.5 cm. Readings were recorded by means of a highly sensitive multimeter. Five loading cycles were conducted for each set of experiments, as shown in Figures 5-3 to Figure 5-6 [89].

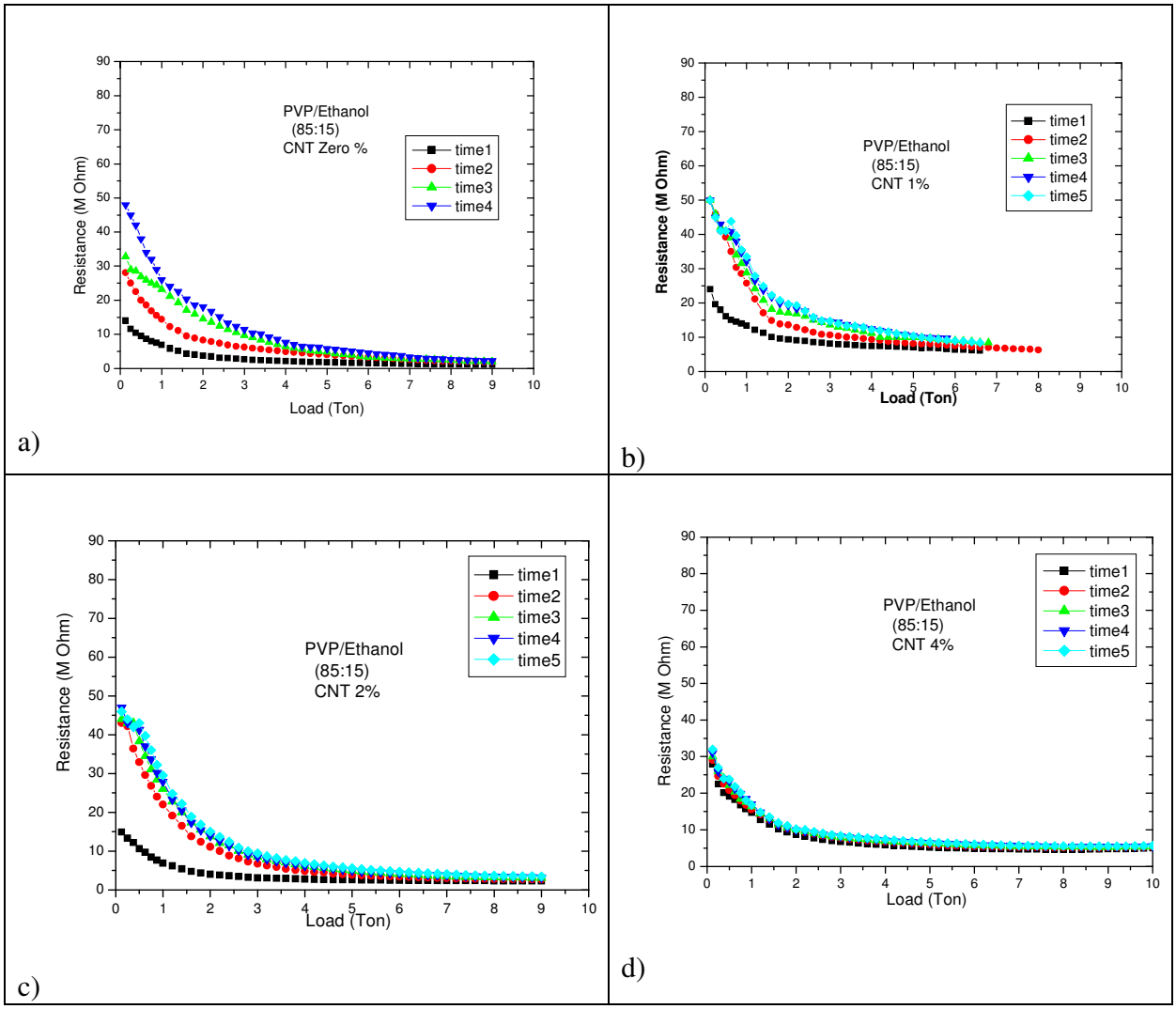

Figure 5-3. Load vs resistance curves of PVP fibers with different wt% of MWCNTs.

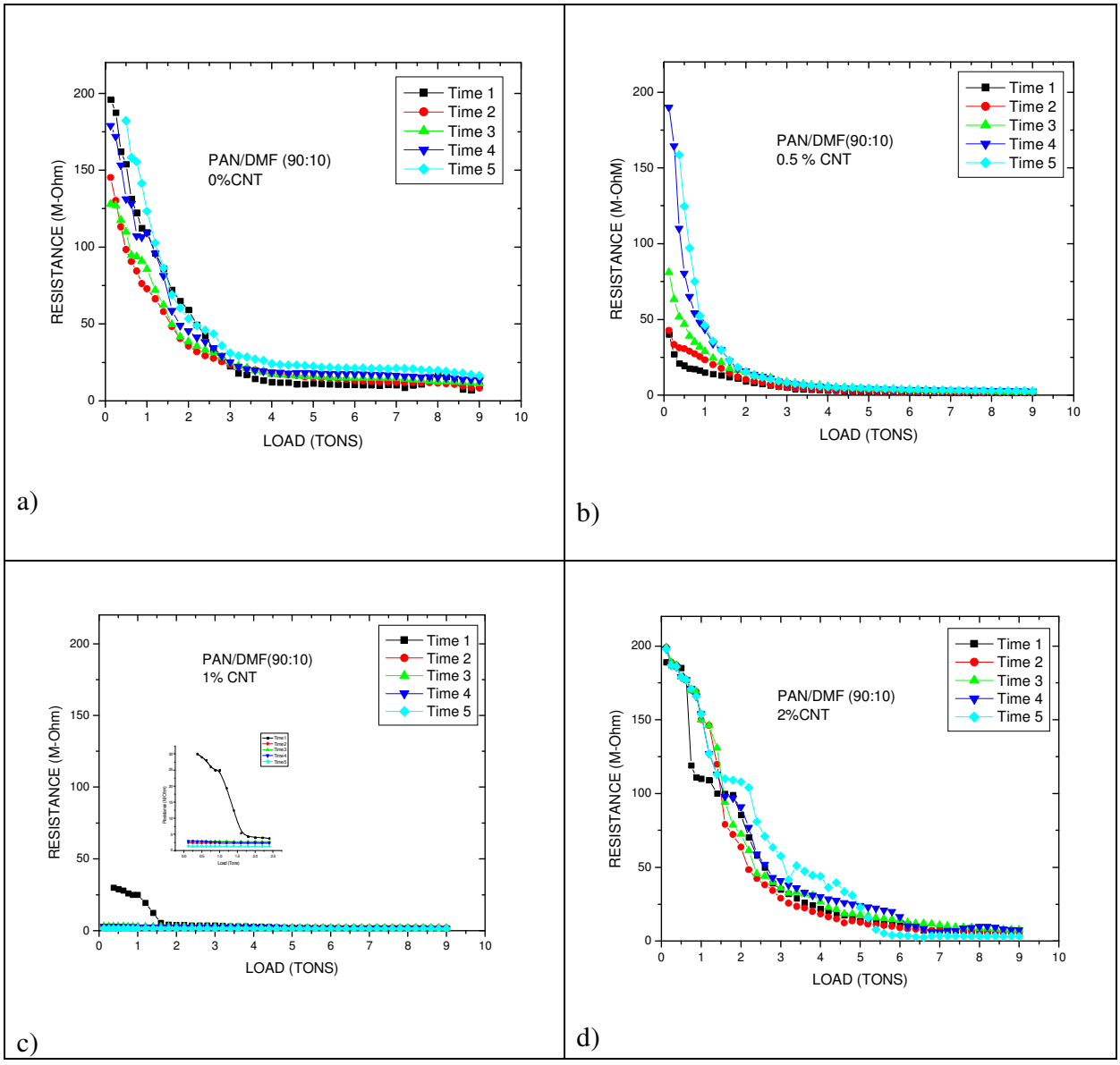

Figure 5-4. Load vs resistance curves of PAN fibers with different wt% of MWCNTs.

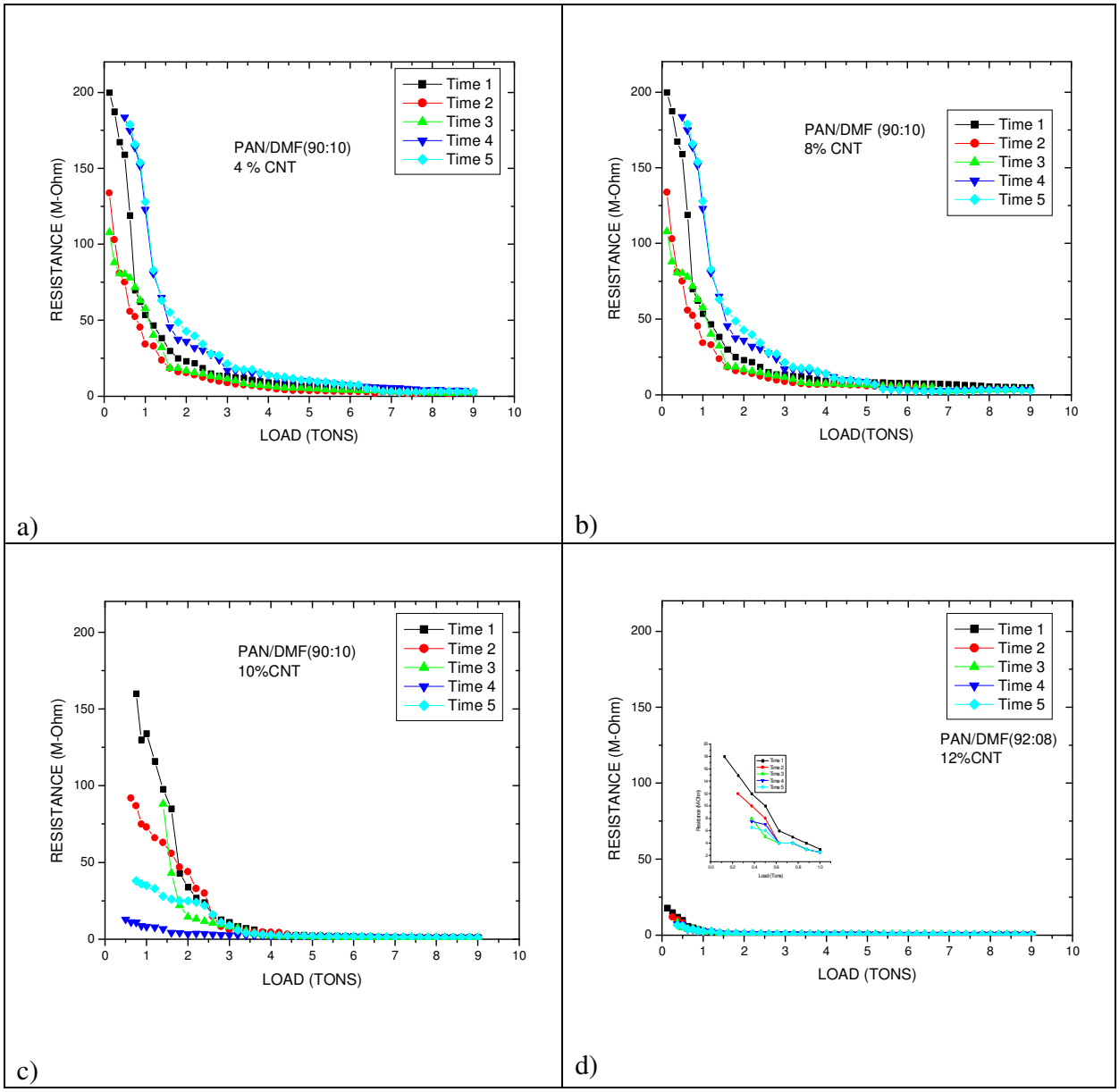

Figure 5-5. Load vs resistance curves of PAN fibers with different wt% of MWCNTs.

As expected, for all the investigated samples and for all cycles, the resistance decreases with load. This behavior can be explained in view of the following equation.

$$R_{resistance} = \rho\left(\frac{L}{A}\right) \tag{5.8}$$

Where $"\rho","\ L"\ and\ "A"$ are resistivity, thickness and cross-sectional area of the sample respectively.when the load increases, there could be two effects. First, the thickness of the sample decreases, and contact area between fiber and electrode increases and therefore resistance decreases. At 0 Wt% of MWCNTs in PVP fibers (Figure 5-3 a), the resistance increases in each trial, when the load is removed, this is due to hysteresis and porosity effect. Whereas, in I and 2 Wt% MWCNTs (Figure 5-3 b & c) experiment, the porosity was reduced due to high Wt% of MWCNTs and therefore, resistance increases only in first trial, when the load is removed, and in subsequent trials the resistance curves overlap due to the fact that porosity is not as effective as it was in first trial and loadings causes inter-molecular damage in polymer fibers and MWCNTs. The MWCNTs are expanded in the polymer matrix thereby reducing the porosity. It was observed that hysteresis reduces as the Wt.% of MWCNTs increases.

As the Wt% of MWCNTs increased the resistance curve became smooth and at 4 Wt% of MWCNTs (Figure 5-3 d) all resistance curves overlapped. This is due to the fact that at high Wt% of MWCNTs, porosity decreases and polarizability and charge carrier concentration increases and therefore, conduction increases. Increasing the content of MWCNTs increases the thermal capacity of the fibers. When the MWCNTs % is higher i.e. 4%, there is no shift between successive trials, since MWCNTs makes nanocomposite conductive and therefore, resistance decreases.

The same trend was observed in PAN fibers (Figure 5-4, 5-5). The factors that influence the resistance are porosity, charge carrier concentration and polarizability. At higher

Wt% of MWCNTs (12%), the resistance curves ovelapped due to high polarizability and high charge carrier concentration. Porosity effect is more dominant without MWCNTs and with low Wt% of MWCNTs, but as the Wt% of MWCNTs increases the effect of polarizability and charge carrier concentration become more dominant. Figure 5-6 shows the resistance vs load curve for PVP and PAN fibers with NiZn ferrites.

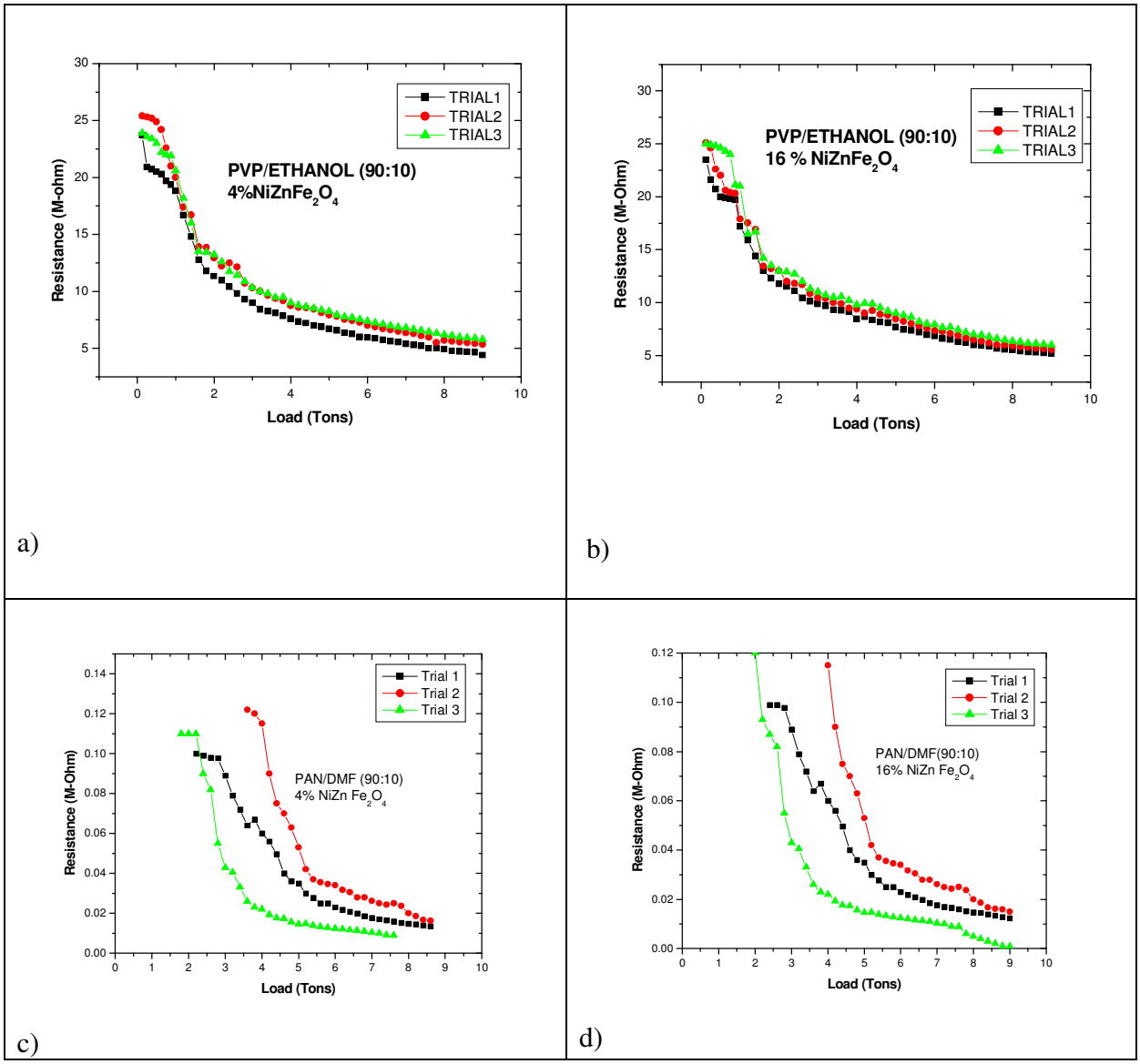

Figure 5-6. Load vs resistance curves of PVP and PAN fibers with different wt% of NiZn-ferrites.

As we can see from Figure 5-6, the slope is not as steep as it was in case of MWCNTs. This shows that the addition of NizN ferrites does not decrease resistance as much as it was in case of MWCNTs. This behavior is due to semi-conducting natrure of NiZn ferrites. Resistance decreases exponentially in case of MWCNTs, but the rate at which resistance decreases is not as high as it was in case of MWCNTs.

5.9.2 Resistance of PVP Nanocomposite Fibers Under Temperature

Figure 5-7 shows the electrical resistantce of PVP fiber with different wt% of MWCNTs and temperature.

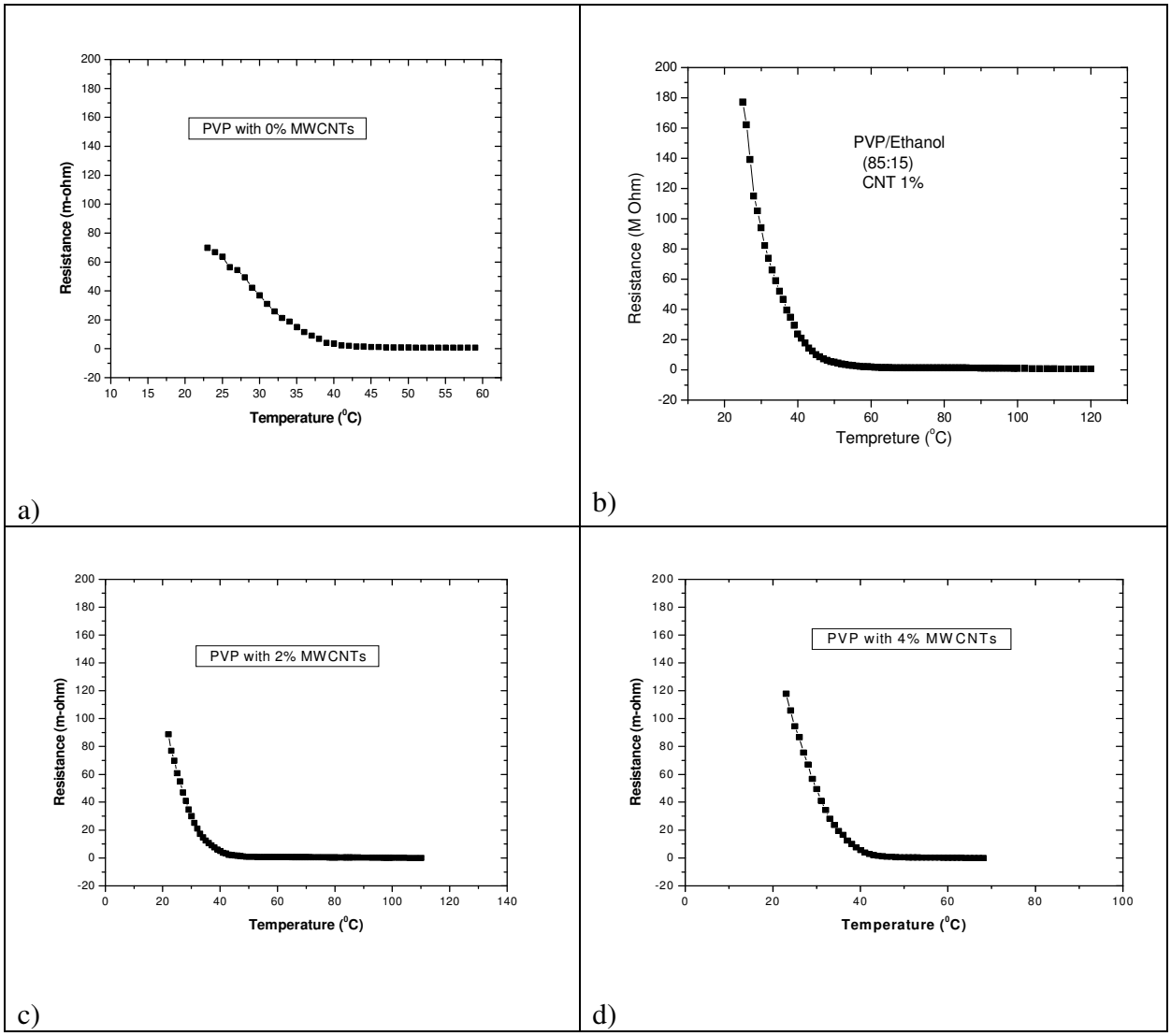

Figure 5-7. Temperature vs resistance curves of PVP fibers with different wt% of MWCNTs.

It is clear from Figure 5-7 that as the temperature increases, electrical resistance decreases. The relationship between temperature and resistivity is governed by [90]

$$\rho = \rho_0 e^{\frac{-E_\mu}{RT}} \tag{5.9}$$

where "ρ" is the resistivity at temperature $T(K)$, "E_{μ}"is the conduction activation energy, "R" is the Boltzmann's constant, and "ρ_0" is the temperature-independent constant. As temperature increases, the polymer molecules slide over each other, and as the tempertaure increases further, the polymer molecules undergo transition phase, where they are partly rubbery and partly solid. Conduction is easy in this phase. PVP is an amorphous temperature and amorphous polymers undergo a transition phase when heated or cooled at a specific temperature known as glass transition temperature (Tg), where the polymer is partly in rubbery and partly in glassy phase.

The glass transition temperature is a function of molecular architecture, monomer units, presence of impurities or low molecular weight species and the rate of temperature changing. Glass transition temperature (Tg) has been extensively studied for many polymers since it is one of the most fundamental feature relative directly to polymer properties. In general, organic nanoinclusions directly contribute to glass transition temperature (Tg) of nanocomposite and the interaction of the polymer chains with the surface of the nanoinclusion can siginificantly alter the chain kinetics in the region surrounding the nanoinclusions due to interface of polymer and inclusions. Numerous studies have shown that nanoinclusions have some effect on glass transition temperature (Tg) of polymer/ nanocomposites. However, no coherent conclusion has been drawn about the effect of nanoinclusions on the glass transition temperature (Tg) so far. Some investigators proved that the glass transition temperature (Tg) of polymer/ nanocomposites increased with increasing the nanoinclusions content.

Since the mechanism is thermally induced, resistance vs temperature behavior can be understood in terms of activation energy. Figure 5-8 shows Log R vs 1,000/T^0K curve for PVP nancomposite fibers with different wt% of MWCNTs.

These plots confirm linear behaviors, which can be divided into three distinct zones, as indicated by the green, blue, and red lines. In the first zone (between room temperature and 37^0C), the conduction could be attributed to impurities [91, 92]. In the second zone, the slopes of the lines (expressing the conduction activation energy) are larger than that of the first zone. This is because more energy is needed to move charge carriers from the impurity level to bands. The activation energy is high in the first and second zones, whereas it is low in the third zone. The transition phase (second zone) between the first and third zones is attributed to the phase transition (phase change), which occurred in nanocomposite fibers. This explanation is confirmed by thermal analysis. Figure 5-9 shows the differential scanning calorimetry (DSC) for the samples with 0, 1, and 4% MWCNTs. It is clear from both the heat flow and the derivative of heat flow that there is a phase transition, which is a second order, and it takes place in the temperature rang (39^0C–57^0C). This confirms that there is a phase transition in the temperature range 39^0C–57^0C, as shown in the 1,000/T curve.

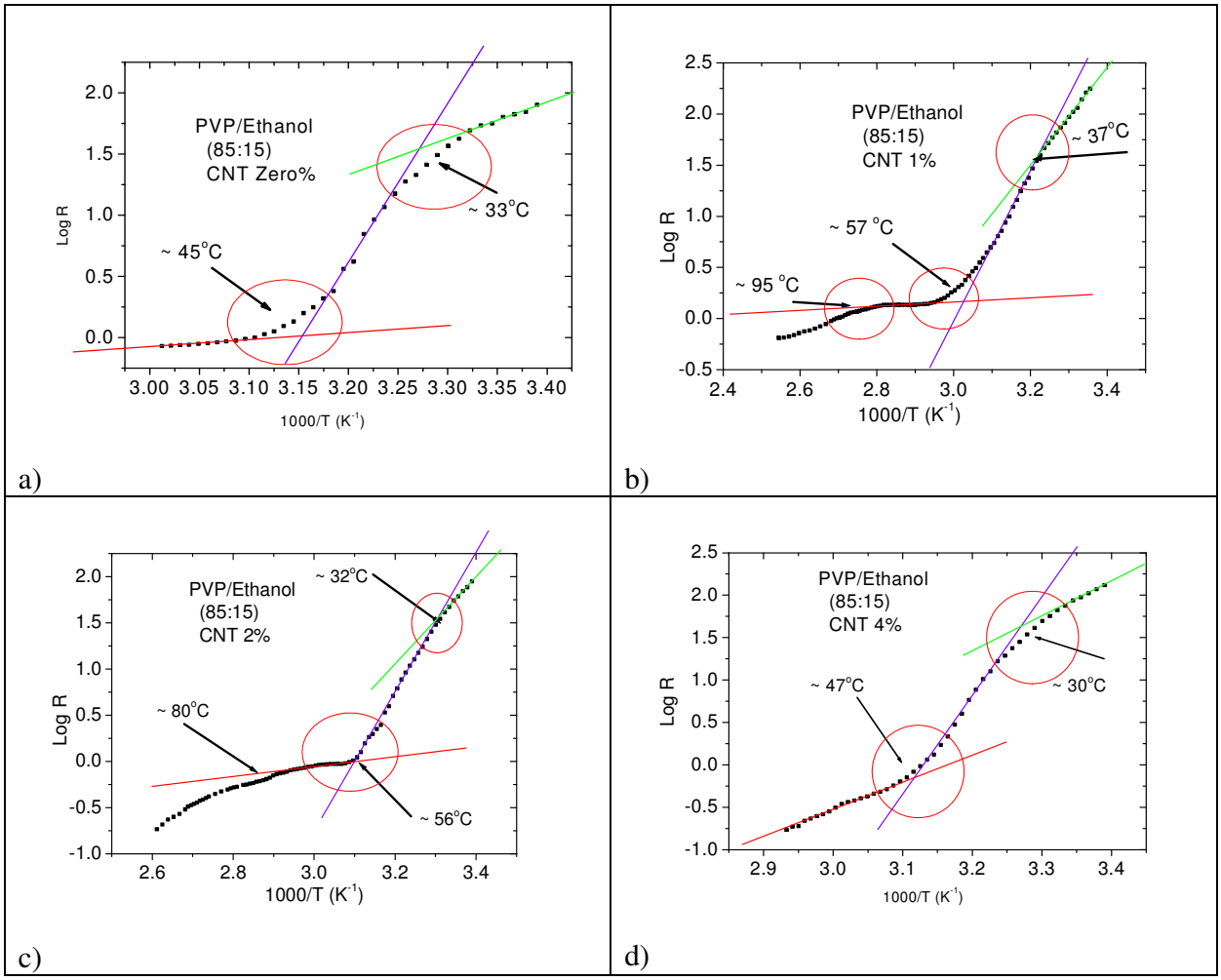

Figure 5-8. Log R vs 1,000/T curves of PVP fibers with different wt% of MWCNTs.

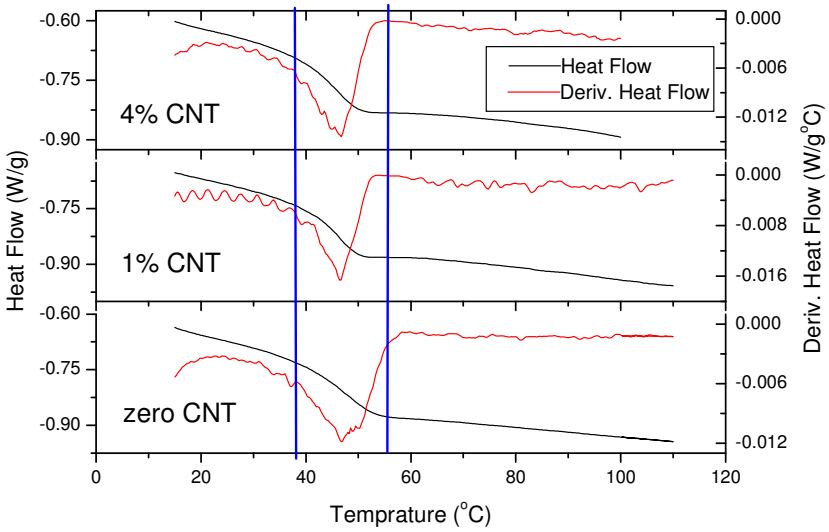

Figure 5-9. Differential scanning calorimetry (DSC) for samples with 0, 1, and 4% MWCNTs.

5.10 Conclusions

In this chapter, the effect of load and tempertaure on the resistance of nanocomposite fibers was determined. The factors that influence the resistance are porosity, charge-carrier concentration, and polarizability. The addition of MWCNTs and NiZn ferrites increases the charge-carrier concentration and polarizability but decreases porosity. Therefore, the resistance curve overlapped due to high weight percentage of MWCNTs in load vs resistance experiments. In load vs resistance experiments of PAN nanocomposite fibers with 4 and 16 wt% of NiZn ferrites, the resistance curves did not overlap. This could be attributed to interfacial resistance between fibers and NiZn ferrites, high ohmic resistance of the PAN polymer, and the semi-conducting nature of NiZn ferrites. In the temperature vs resistance experiment with PVP nanocomposite fibers, the polymer molecules underwent a transition phase in the temperature range 39^0C–57^0C. This transition phase was confirmed by differential scanning calorimetry.

CHAPTER 6

THERMAL CHARACTERIZATION OF NANOCOMPOSITE FIBERS

6.1 Introduction

The thermal conductivity of solid materials can be determined by numerous experimental methods. These methods have been designed for a specific application to suit the desired accuracy. The comparative method is one of the most widely use techniques of measuring thermal conductivity and is the only feasible method of measuring thermal conductivity of thin layers. This method uses a sample of unknown thermal conductivity and a sample of known thermal conductivity. It is based on recording the progress of the temperature increase in the unknown sample and comparing it to the progress of rising temperature in the known sample. This method carries minor errors and is very sensitive to the environment. Recently, Moss et al. [99] and Sweet et al. [100] at the Sandia National Laboratories (USA) conducted a systematic study to determine the accuracy limits of the measurements by the comparative method and confirmed that the accuracy of $\pm 5\%$ can be achieved by this method.

6.2 Motivation and Objectives

In this research, the thermal conductivity of MWCNTs and NiZn ferrite-based nanocomposite fibers was determined and compared. It was shown that carbon nanotubes have better thermal and electrical characteristics. Their thermal conductivity is 3 to 4 times higher than many metals such as copper and silver. NiZn ferrite is a single-phase powder having spinel structure. NiZn ferrite is a semi-conductor material, whereas carbon nanotubes are very good conductors. In this research, thermal conductivity of nanaocomposite fibers as a function of nanoscale inclusions was determined.

6.3 Heat Conduction in Polymers

Heat conduction usually follows Fourier's law, which can be stated with isotropic systems [101] as

$$q_x = -K\Delta t/\Delta x \tag{6.1}$$

This law states that heat flux is proportional to temperature gradient. Since polymers are often anisotropic, it is therefore relevant to state the general three-dimensional form of Fourier's law [101] as

$$\left.\begin{aligned} q_x &= -\frac{K_{xx}\Delta t}{\Delta x} - \frac{K_{XY}\Delta t}{\Delta y} - \frac{K_{XZ}\Delta t}{\Delta z} \\ q_Y &= -\frac{K_{YX}\Delta t}{\Delta x} - \frac{K_{YY}\Delta t}{\Delta y} - \frac{K_{Yz}\Delta t}{\Delta z} \\ q_{Z=} &-\frac{K_{Zx}\Delta t}{\Delta x} - \frac{K_{Zy}\Delta t}{\Delta y} - \frac{K_{ZZ}\Delta t}{\Delta z} \end{aligned}\right\} \tag{6.2}$$

These equations show that for an anisotropic material, the heat flux in a certain direction does depends on the temperature gradient not only in that direction but also in other directions. The thermal conductivity for an anisotropic material is a tensor property, which can be identified by nine components, K_{ij}. The nine components can be reduced to six components as follows [101]:

$$\left.\begin{aligned} K_{xy} &= K_{yx} \\ K_{YZ} &= K_{Zy} \\ K_{xz} &= K_{zx} \end{aligned}\right\} \tag{6.3}$$

When the coordinate directions corresponding to the directions of principal conductivity, the cross components of the conductivity tensor are zero [101]:

$$\left.\begin{aligned} q_x &= -\frac{K\Delta t}{\Delta x} \\ q_y &= -\frac{K\Delta t}{\Delta y} \\ q_z &= -\frac{K\Delta t}{\Delta z} \end{aligned}\right\} \tag{6.4}$$

If theses conductivities are known, then all the conductivity coefficients for any arbitrary coordinate's orientation with respect to the principal conductivities may be determined. If the

principal conductivity directions are known, then the conductivities can be measured by standard methods utilizing one-dimensional heat flow. The quantum of lattice vibration is called phonon. Over most of the temperature range, phonons are scattered by the disordered, amorphous structure giving a constant mean free path and a thermal conductivity proportional to the volumetric heat capacity. At low temperature, phonon wavelength becomes larger and the mean-free path is proportional to the square of the phonon wavelength, leading to a liner relation between thermal conductivity and temperature. The crystalline polymer has a higher thermal conductivity. This is because energy can be transmitted more readily along the polymer molecule than between molecules. Hansen and Ho [101] predicted that thermal conductivity increases as the square root of the weight-average molecular weight at low molecular weights, and become independent of molecular weight at high molecular weights. For branched and linear polymers of equal molecular weight, the linear polymer will have higher thermal conductivity. Addition of plasticizers generally reduces the thermal conductivity. The thermal conductivity is also dependent on orientation of the polymers. The thermal conductivity is generally increased parallel to stretching and reduced perpendicular to stretching. Stretching the polymer orients the low resistance preferentially parallel to the stretching direction and the high resistance preferentially perpendicular to the stretching direction. In comparison to amorphous polymers, crystalline polymers are ordered and dense and, therefore, have high thermal conductivity.

PVP is amorphous, while PAN is around 34% crystalline. It is expected that the conductivity of crystalline polymers would be less sensitive to molecular weight. The crystalline structure of polymers are anisotropic and when oriented could yield significant anisotropy in heat conduction properties. No research has been done on the orientation effects of polymer conduction. Some researchers have reported that thermal conductivity of polymers is dependent

on density of polymers. No adequate theory that may be used to predict accurately the thermal conductivity of polymeric solution or solid exists. Most proposed theoretical expressions are based on Debye's [103] treatment of conductivity, which is given by the following equation:

$$K = \Lambda C_y \rho u L \tag{6.5}$$

where "C_y" is the specific heat, "ρ" is the density, "u" is the velocity of elastic wave (sound velocity),"L" is the average free path length, and "Λ" is a constant on the order of magnitude of unity. Kardos et al. later proposed the following analogous equation [103]:

$$K = C_p \rho u L \tag{6.6}$$

at which "L" represents the distance between the molecules in adjacent isothermal layers. In an amorphous polymer, thermal conductivity increases until the glass transition temperature is reached and then exhibits a gradual decline as the temperature continues to increase beyond the glass transition temperature (Tg). Crystalline polymers show much higher thermal conductivity.

6.4 Non-Conducting Polymers

In polymers with chemically saturated structures, the electrons are tightly bounded in the α-bonds between atoms. In α-bond polymer structures, all available electrons are tightly connected in strong covalent bonds [102]. Since all available electrons are fixed in the α-bonds, there are no free electrons to carry the electrical current. Therefore, saturated polymers are characteristically electric insulators. Because of this, any electrostatic charges that they acquire are retained for a long time. Since charges may be deposited by mere contact with a different material, the charged condition is frequently encountered with articles made from polymers. Although the contact charges represent only a small imbalance of charge compared with the total amounts of positive and negative charge that is present in the matter, they give rise to electric fields, which are high enough to cause a spark. Thus, a surface-charge density resulting from just

one or two extra electronic charges per million surface atoms is sufficient to generate a field that exceeds the air breakdown value [102]. The occurrence of sparking means that an insulating specimen will often present a complex and confusing distribution of charges on its surface. No known insulator is completely free of the conduction process, charges are expected to diffuse away eventually under the influence of their field. This is true in polymers in which the structure is disordered, creating a low density of defects sites, which can be occupied by charge carriers. Low-level conduction in essentially insulating materials can take a variety of forms. Often it may be attributed to impurities that provide a small concentration of charge carriers in the form of electrons or ions. At high fields, the electrodes may inject new carriers into the polymers, causing the current to increase more rapidly with voltage than in accordance to Ohm's law. At very high fields, these and other processes, often-involving conduction over a surface, inevitably lead to complete failure of the material as an insulator [102].

6.5 Conducting Polymers

Compounds in which orbits are used to form double bonds between carbon atoms, rather than forming single bonds with other atoms, are said to be unsaturated [102]. Successive carbon atoms in a chain engage in π-bonding, where the structure is said to be conjugated and may be represented as a sequence of alternating single and double bonds. The π-bonding in a conjugated chain would produce bonds of equal length, with the one orbit of each carbon overlapping equally with the orbits of both of its neighboring carbon atoms along the chain [102]. Such uniform orbit overlap would form a π-electron wave function extending over the entire polymer backbone. The electrons would then be delocalized and free to move along the polymer backbone. In this idealized case, the polymer can be described as a one-dimensional metal with a half-filled conduction band. However, localization of electrons in double (or triple) bonds, which

characterize conjugated polymers, lowers the overall energy of the electron system. This introduces an alternation in bond length and opens up an energy gap in the electron density of states. An increase in the elastic energy of the backbone bonds occurs, but this is less than the energy gained by the electron system. This has some significant effect on the properties of the polymer, with the presence of the energy gap turning it into a semiconductor. Interaction of conjugated polymers with electrons donating or accepting impurities can also result in the addition or removal of electrons from the polymers. This can produce a sufficient number of free-charge carriers in the polymer; therefore, it becomes metallic [102].

6.6 Experiment

The thermal conductivity of PVP and PAN nanocomposite fibers with different wt% of MWCNTs and NiZn ferrites was measured by the comparative method. This method is used extensively for axial-flow thermal-conductivity testing. In this method, the heat flux passes through the known sample and the unknown sample, and compares the thermal gradient of the two, which will be inversely proportional to their thermal conductivities. The unknown sample is placed between the two known samples. The known sample is copper, which has a thermal conductivity of 401 W/m-^{0}K at room temperature. This arrangement is shown in Figure 6-1. A copper rod was heated by means of a power source (Elenco Precison Quad Power Four Liner Regulated Supplies) at the top, and ice water was placed at the bottom (sink), in order to have maximum heat flow in the axial direction. The sink removes heat, and the electrical coil regulates the flow of heat to the sink without distorting the temperature gradient. Different compressive stresses (834.20 Kpa, 333.67 Kpa and 166.83 Kpa) were applied at the top of the assembly to provide better contact between known and unknown samples and a comparision was made between the thermal conductivities under different stress level.

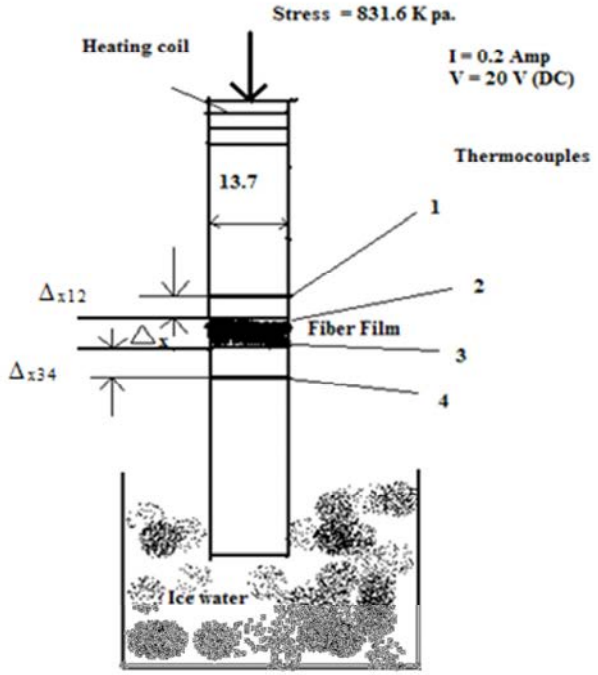

Figure 6-1. Experimental arrangement of thermal conductivity measurement.

This setup was tested on the known materials before using the nanocomposite fibers. Both samples (known and unknown) were enclosed by insulation to eliminate convection losses. As far as radiation losses are concerned, which are more significant at high temperature (above 100^0C), the current supply was limited to 0.2A (20 DC volts), which provided a temperature of around 60-70^0C. The same conditions were kept throughout the experiment. Four K-type thermocouples, two at the top of the sample (thermocouples 1 and 2) and two at the bottom of the sample (thermocouples 3 and 4) were attached. A sensitive multimeter was used to measure the temperature difference in millivolts. Then the millivolt readings were converted into ^{0}C by the following equation:

$$1\ mv = 5.46\ ^0\text{C} \tag{6.7}$$

This equation was developed by immersing the two ends of the nickel-chromium and nickel-aluminum thermocouples at two different temperatures in water and recording the millivolt readings on a sensitive multimeter. The heat flux through points 1 and 2 and points 3 and 4 were calculated as [104]

$$\left.\begin{aligned} q_{12} &= \frac{K_{cu} A\, \Delta T_{12}}{\Delta x_{12}} \\ q_{34} &= \frac{K_{cu} A\, \Delta T_{34}}{\Delta x_{34}} \end{aligned}\right] \tag{6.8}$$

where "K_{cu}"(copper) is the thermal conductivity of the references, "A" is the cross-section area of the copper rod (1.47×10^{-4} m^2), "ΔT_{12} and ΔT_{34}" are the temperature differences between points 1 and 2 and points 3 and 4, respectively. The average heat flux $(q_{12} + q_{34})/2$ was compared with the heat flux flowing through the sample. The thermal conductivity of the sample was calculated as [104]

$$q_{Avg.} = \frac{K_S\, \Delta T_{23} A}{\Delta x_{23}} \tag{6.9}$$

The measurement uncertainties used in this experiment are based on instrument manufacturer's specifications. K-type thermocouples (Nickel-Chromium and Nickel-Aluminum) were used in this experiment and they carry an error of 0.75% above 0°C. An error of 0.75% was applied to the thermocouples reading before calculating the thermal conductivity.

Figure 6-2 shows the setup of the thermal conductivity measurement apparatus.

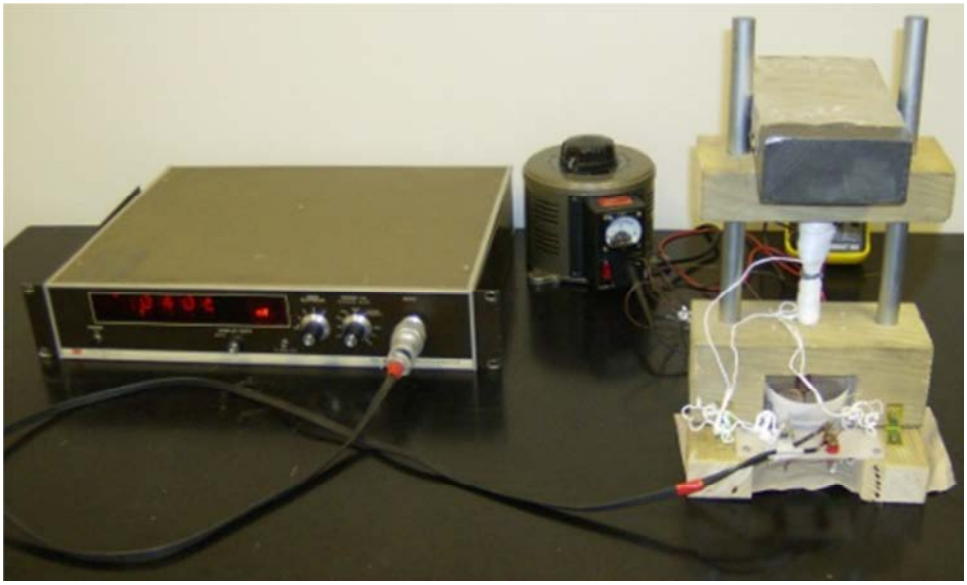

Figure 6-2. Setup for thermal conductivity measurement of PVP and PAN fibers [104].

6.7 Results and Discussions

The thermal conductivity of PAN fibers with different wt% of MWCNTs was determined experimentally. The results are given in Table 6-1

TABLE 6-1

THERMAL CONDUCTIVITY OF PAN FIBERS WITH DIFFERENT WT% OF MWCNTS

Wt% MWCNTs	**Thermal Conductivity (K) W/m-^{0}C**		
	Under 834.20 Kpa	**Under 333.67 Kpa**	**Under 166.67 Kpa.**
0	0.01968	0.0153	0.0127
1	0.0887	0.0553	0.045
2	0.1146	0.0589	0.0534
4	0.1185	0.06287	0.0587
8	0.179	0.0876	0.07832
15	0.2065	0.088	0.0798

Carbon nanotubes have excellent thermal and electrical conductivity, but the addition of MWCNTs to composites does not seem to increase the fiber's thermal conductivity to any significant extent. The reason for only a slight increase in thermal conductivity is the interfacial resistance among MWCNTS, air, and polymeric fibers. Nearly all polymers are insulators, and MWCNTs are excellent conductors. The thermal conductivity of MWCNT/composite fibers depends upon the characteristic of nanotubes, their alignment, and dispersion techniques [101]. Some researchers have reported the thermal conductivity of nanotubes as low as 30W/m-^{0}K, while others have reported the influence of size and shape of nanotubes drastically changing their thermal conductivity. In MWCNT/nanocomposite fibers, a larger number of phonons than electrons entering a nanotube/polymer composite have to travel through the matrix because the contrast in thermal conductivity $K_{nanotube}/P_{polymer}$ is around 10^4 in comparison to the electrical conductivity $K_{nanotube}/P_{polymer}$ of 10^{14} to 10^{19}[101]. Atomic vibrations or phonon interaction dominate the thermal conductivity of carbon materials leading to high interfacial thermal resistance between nanotubes [101]. The interfacial resistance comes from the constraint that the energy in the high-frequency phonon mode within the nanotubes must be transferred to the low-frequency mode through phonon-phonon coupling in order to be exchanged within the surrounding medium [101]. Huxtable et al. [101] has estimated that the thermal conductance is around 12MW/ m-^{0}K at the polymer-nanotube interface. Nanotubes with low surface area have a tendency to improve thermal conduction, because there is less phonon scattering at the interface of nanotubes and polymer and the existence of shielded internal layers promote the conduction of phonon and minimize the matrix coupling losses. Scientists and researchers are making efforts to reduce the interfacial resistance between nanotubes and polymer by covalent bonding functional groups onto nanotubes and by overlapping nanotubes.

The thermal conductivity of PVP fibers as a function of MWCNTs was determined, and the results are given in Tables 6-2. As can be seen, the behavior of these nanocomposite fibers is similar to that observed in PAN fibers.

TABLE 6-2

THERMAL CONDUCTIVITY OF PVP FIBERS WITH DIFFERENT WT% OF MWCNTS

Wt% MWCNTs	**Thermal Conductivity (K) W/m-^{0}C**		
	Under 834.20 Kpa	**Under 333.67 Kpa**	**Under 166.67 Kpa.**
0	0.1238	0.0302	0.0243
1	0.1421	0.0372	0.028
2	0.1452	0.08473	0.055
4	0.1472	0.091	0.077

6.8 Comparision Between MWCNTs Based Nanocomposite and NiZn Ferrites Based Nanocomposite

$Ni_{0.6}Zn_{0.4}Fe_2O_4$ (NiZn ferrites) were prepared by the usual co-precipitation technique as described in Chapter 3 having particle size of around 21.5 nm (Figure 3-8 a & b) and were encapsulated in PVP and PAN to fabricate nanocomposite fibers and a comparision was made between the thermal conductivities of NiZn ferrites and MWCNTs based nanocomposite fibers under 834.20 Kpa.

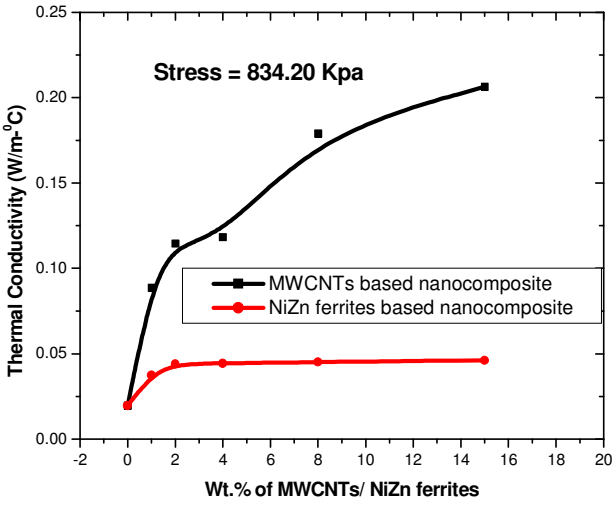

Figure 6-3. Comparison between thermal conductivity of PAN fibers with MWCNTs and NiZn ferrite nanoparticles.

Figure 6-3 shows that the thermal conductivity increases as the Wt% of MWCNTs increases in PAN fibers whereas, the addition of NiZn ferrites does not have any profound effect on thermal conductivity. The thermal conductivity of PAN fibers with NiZn ferrites improves from 1wt. % to 2 wt% and after 2 wt. %, there is no significant increase in thermal conductivity.

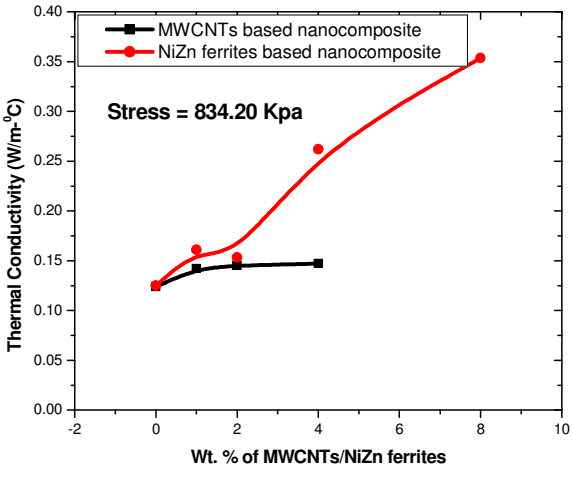

Figure 6-4. Comparison between Thermal conductivity of PVP fibers with MWCNTs and NiZn ferrite nanoparticles.

As is seen in Figure 6-4, the similar behavior was observed in MWCNTS based nanocomposite fibers. The thermal conductivity of NiZn ferrites based PVP nanocomposite fibers has shown some improvement as compared to PAN nanocomposite fibers. It is well known that, MWCNTs and NiZn ferrites are conducting and semicoducting materials, respectively, while PVP and PAN are insulators.

6.9 Conclusions

Comparative method is used to find out the thermal conductivity of nanocomposite fibers. According to the manufacturer's catalog the thermal conductivity of MWCNTs was 1600w/m-^{0}C, this led to the initial suggestion that these MWCNTs will certainly enhance the thermal characteristics of nanocomposite fibers to a significant extent. However, the thermal conductivity of nanocomposite fibers has failed to show any dramatic improvement. The factors that influence this low thermal conductivity of nanocomposite fibers are the interfacial resistance among carbon nanotubes, presence of air, alignment of nanotubes, dispersion technique and a sharp contrast in thermal conductivity of nanotubes and polymer. NiZn ferrites based nanocomposite fibers did not show any drastic changes in thermal conductivity due to semiconducting nature of these ferrites.

CHAPTER 7

ACOUSTICAL PROPERTIES OF ELECTROSPUN PVP AND PAN NANOCOMPOSITE FIBERS

7.1 Introduction

7.1.1 Interior Noise

Interior noise is becoming increasingly important to aircraft, spacecraft, and helicopter manufacturers for the comfort of their customers and air crew members during long flights [106]. This issue will also be more important for the new generation of subsonic and supersonic aircraft under development or construction. It is known that noise interferes with the crew's flight ability and health (e.g., hearing disorders, higher blood pressure, dizziness, headaches, exhaustion, etc.), sleep, work efficiency, and flight performances and safety over the long term. Furthermore, noise effects on seniors, children, and the unborn are more harmful than on adults [106, 109]. Therefore, a multidisciplinary research program is needed to achieve acceptable noise levels in aircraft, as well as other transportation vehicles (e.g., automobiles, ships, and trains) and infrastructures (e.g., hospitals, schools, business centers, roadside homes, and manufacturing facilities).

Aircraft interior noise is produced by aircraft during run-up, taxiing, take-off, over-flying, and landing. Studies on the interior noise of general aviation aircraft show that noise level varies based on the types of aircraft and engines used [110,111]. For a propeller-driven aircraft, the dominant noise sources are rotating propellers and striking pistons, which create periodic sound loads on the fuselage at known blade-passage frequencies. For jet engine-driven aircraft, including turbofan, turboprop, and turbojet, the primary source of noise is the roar of the jet exhaust and the high-pitched noise generated by the engine's turbo-machinery system,

compressors, and engine blades. The noise of the exhaust roar is created by the rapid expansion of high-velocity exhaust gases into the atmosphere. In most cases, the amount of noise generated by an aircraft engine is proportional to its exhaust stream velocity. Engine noise is also dictated by mid- to high-frequency engine tones with a blade passage frequency (BPF). During flights, the broadband characters of turbulent boundary layer excitations result in an interior noise, which dominates the overall sound pressure level (SPL) and speech interference level (SIL) inside the aircraft [108, 111].

As is known, the aircraft fuselage has a complicated structural system that faces turbulent boundary layer pressures, external acoustic sources, dynamic flows, and other factors at different locations. In addition, flight variables (e.g., pressure altitude, indicated air speed, wind, cabin pressure, lightening strikes, and other weather conditions) also increase the sound level and transmission into the fuselage [106,107]. It was reported that noise levels and frequencies of the aircraft fuselage vary, based on location and types of fuselage (composite, metal, or both), which makes the problem harder and more complicated in perdition and modeling [108].

7.2 Noise Absorbers

Noise mitigation involves a set of strategies to reduce unwanted noise inside aircraft. As is known, any material that allows air to pass through it will act as a sound absorber. The friction of sound energy moving through the absorber reduces sound by transferring it into heat energy [111]. Thicker absorbers usually offer greater resistance to air molecules because of the greater porosity and surface areas, so they are more efficient in absorbing sound. However, thicker absorbers will increase the overall weight of the aircraft and reduce fuel efficiency. Today, most noise absorbers that are used to control the aircraft's interior noise are porous membranes, cavities, perforated panels, and composite absorbers in the form of open- and closed-cell foams,

fiberglass, cloth, mineral wool, acoustic ceiling tiles, and wood fibers. Most of these materials used in aviation are flame resistant, which are also approved by the Federal Aviation Administration (FAA) [112,113].

7.2.1 Porous Absorbers

Porous absorbers with open-pore structures include all porous and filamentary materials, such as mineral wool, fiberboard, fabrics, fleece, carpets, cotton, and special acoustic plaster. These materials absorb sound energy when vibrating air molecules are forced through the pores to interact with the surface of the walls. These may be effective for high frequencies with short wavelengths [111].

Aramids are a family of nylons that are utilized to produce Kevlar and Nomex, which have complex chemical structures. Kevlar is a light and very strong fiber in the form of ropes or sheets of fabric, and can be used either as-is or in the construction of composite components for puncture-resistant panels, cloths, and bullet-proof vests. Nomex is produced in both fiber (10-100 μm) and sheet forms, and is used as a fabric (i.e., overframe blanket) wherever heat and flame resistance may be required. Recently, these materials/fibers (especially Nomex) have been used to reduce interior aircraft noise because of their pore structures and flame resistance, but all are on the microscale [111,112].

7.2.2 Membrane Absorbers

Absorptive membranes directly influence reverberation time (persistence of sound in a particular space after the original sound is removed) and reflected sounds, and are more effective at low frequencies. These membranes may be flexible, supporting panels mounted at some distance from the front of a solid wall. Conversion to heat takes place as a result of the resistance

of the membrane against sound waves of air molecules. They are effective at their resonant frequencies, which depend upon the surface density and width of the enclosed space [106].

7.2.3 Cavity Absorbers

These absorbers (known as Helmholtz resonators) are simply air containers with a narrow neck. The air within the cavity has a spring-like effect at the particular resonant frequency of the enclosed air volume. Helmholtz resonators are built to solve the noise problem around 500 and 1,000 Hz; therefore, these absorbers may give a high-absorption coefficient in a very narrow frequency band. This can be broadened slightly by placing a porous material in the system [106].

7.2.4 Composite Absorbers

Composite materials are commonly used as acoustic absorbers due to their wide range of applications and good acoustic properties. These composites are typically fire-retardant polyether absorbers with mass-loaded barriers (e.g., PVC). Therefore, they have been specifically designed to have a low-reflection upper surface and high-absorption lower mass. Some of the sound energy is captured and absorbed within the upper acoustic foam layer. The remaining sound energy reaching to the very dense mass layer at the base of the composite is then converted into thermal energy at molecular levels. Since this process occurs on a very small scale and involves very low levels of kinetic energy, it may not result in a noticeable increase in temperature [111].

7.2.5 Perforated Panel Absorbers

These absorbers are a combination of the above absorbers along with holes in different sizes and shapes. The absorptive panels are thin and flexible panels of plywood, hardboard, plasterboard, or metal, and act as a membrane absorber. Fiberglass and mineral wool can be placed inside the frame to help reduce the sound energy [106].

In this research study, electrospun fibers were suggested as a potential replacement for conventional noise absorbers. There are several advantages of using high surface area electrospun fibers in the interior noise reduction systems of aircraft [115]:

- Many of the polymeric materials, including flame-resistant polymers, can be electrospun.
- Surface area of the nanofibers is 100 to 10,000 times higher than conventional fibers such as fiberglass, mineral fiber wool, open-cell foam, acoustic ceiling tiles, and wood fibers.
- The noice absorption rate is expected to be exponentially higher because of the interaction of air molecules of sound waves with the fiber surfaces.
- The overall weight of the materials used for the noise absorption will be less.
- The porosity of the nanofibers is much higher compared to the fibers that are currently used in aircraft for noise reduction and insulations.
- Physical and chemical characterizations of nanofibers are well known.
- Nanofibers can enhance the physical properties of materials.
- Nanofibers can be electrospun on both composite and metal surfaces.
- Electrospinning is an economical and technologically mature method for a bulk production.

7.3 Motivation and Objectives

Electrospun fibers can be used as an appealing candidate for sound absorption in aircraft interior instead of conventional materials such as foams, cavities, viscoelastic, solids, and liquid structures. Electrospun nano- and microfibers have many advantages over conventional materials. The porosity of electrospun fibers is much higher than that of fibers currently used in aircraft for noise reduction. The production process via electrospinning is relatively easy and inexpensive. The weight of the electrospun fibers is much less than conventional materials.

7.4 Experiment

Polyvinylpyrrolidone (PVP), polyvinylchloride (PVC), and polystyrene (PS) with molecular weights of 130,000 g/mol, 150,000 g/mol, and 230,000 g/mol were separately dissolved in ethanol, dimethylacetamide (DMAc), and dimethylformamide, respectively. These chemicals were purchased from Sigma-Aldrich and used without future purification or processing. Figure 7-1 shows SEM images of PVP, PVC, and PS electrospun fibers with various processing parameters. Table 7-1 gives the electrospining process parameters of these three different electrospun fibers.

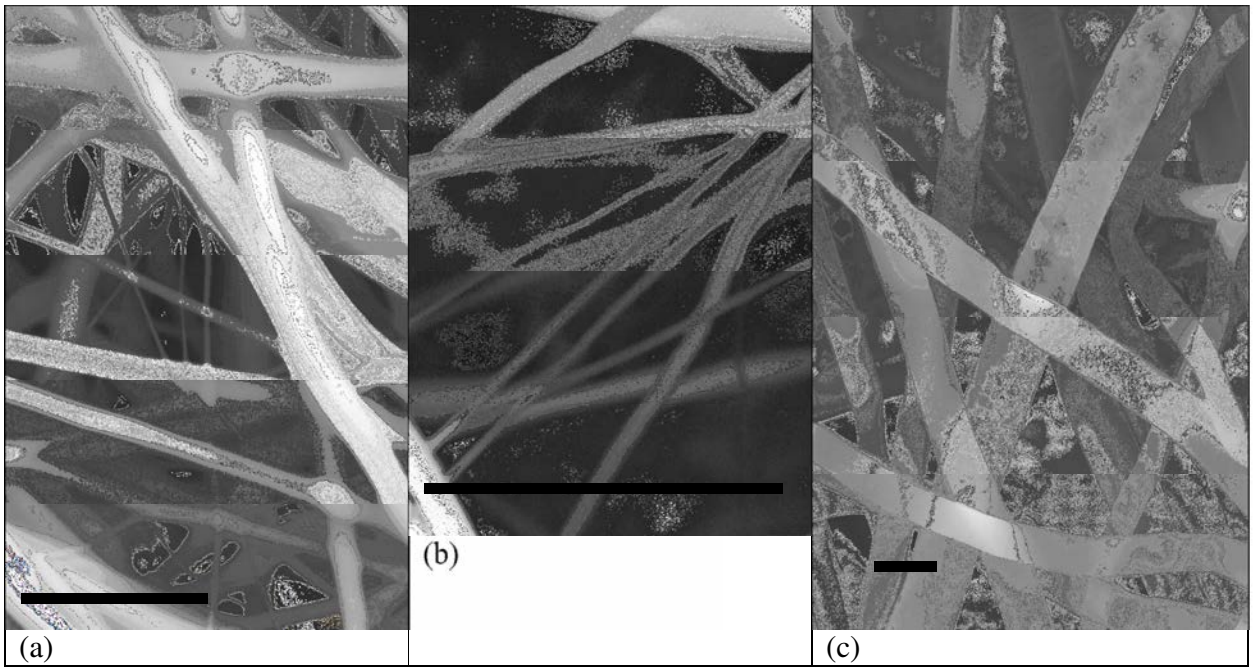

Figure 7-1. SEM images: (a) PVP, (b) PVC, and (c) PS electrospun fibers at various electrospinning conditions (scale bar is 10 μm).

TABLE 7-1
ELECTROSPINNING PROCESS PARAMETERS OF PVC, PVP, AND PS FIBERS USED FOR SOUND ABSORPTION TESTS

Polymers w/ Solvent Ratio	Spinning Voltage (kV)	Screen Distance (cm)	Pump Speed (ml/h)	Fiber Diameter (nm)
PVP/Ethanol (80:20)	15	20	3.0	~750
PVC/DMAc (80:20)	18	25	3.0	~250
PS/DMF (75:25)	25	25	1.5	~7000

7.4.1 Sound Absorption Tests

Sound absorption tests were conducted using the B&K impedance tube method shown in Figure 7-2. Generally, two different diameter tubes were used to cover the full frequency range. A 100 mm diameter tube was employed to cover measurements in the frequency range of 150 to 1,600 Hz, while a 29 mm diameter tube was utilized to cover measurements in the frequency range of 1,200 to 6,400 Hz [107]. The goal of the sound measurement was to determine the normal incidence sound absorption coefficient as a function of applied frequency. During tests, a loudspeaker was mounted at one end of an impedance tube, and a small sample of the fiber film was placed at the other end [114]. As the sound waves propagated in the tube, the air molecules hit the surface of the fiber film and were reflected back, resulting in a standing wave interference pattern. Sound absorption is described as the percent of sound energy being absorbed by the absorber. For these tests, the sound pressure at two or more locations was measured, and the complex transfer function was calculated. It was then possible to determine the complex reflection coefficient, the sound absorption coefficient, and the normal acoustic impedance of the fibers [107].

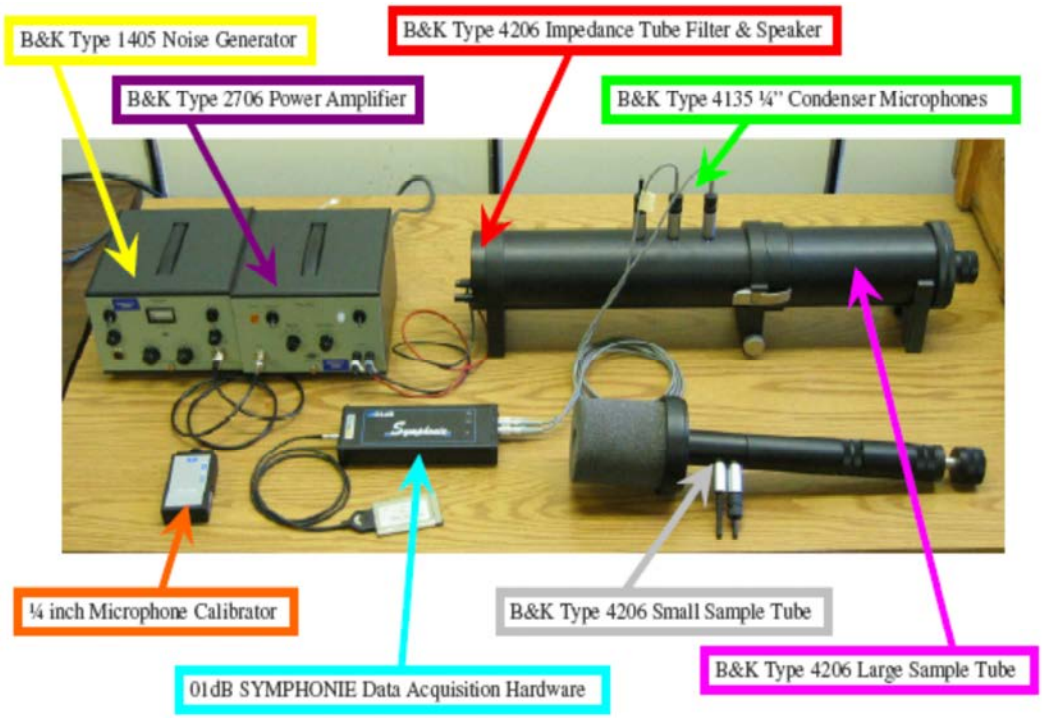

Figure 7-2. B&K type 4206 impedance tube for measuring sound absorption.

7.5 Results and Discussions

Table 7-2 gives the weight, thickness, and sound absorption coefficient values of each PVP, PVC, and PS sample at 2,000 and 6,000 Hz frequencies.

Figure 7-3 shows the results of the first sound absorption tests conducted on 0.5, 1, and 1.5 g of PVP fiber samples (A, B, and C, respectively). The fiber diameter of PVP obtained using DMAc solvent was between 500 and 900 nm. The sound absorption coefficients of Samples A, B, and C were 0.32, 0.61, and 0.65, respectively, at 2,000 Hz, and 0.93, 0.86, and 0.91, respectively, at 6,000 Hz. Surprisingly, the lighter-weight PVP samples gave the same absorption coefficient value, with heavier films at 6,000 Hz. However, as the weight of the nanofibers increased, the absorption peek shifted toward the lower frequency, which covers more frequency ranges.

TABLE 7-2

WEIGHT, THICKNESS, AND SOUND ABSORPTION COEFFICIENT VALUES OF ELECTROSPUN FIBERS SAMPLES

Sample	**Sample Weight (g)**	**Sample Thickness (cm)**	**Sound Absorption Coefficient at 2,000/6,000 Hz**
PVP Sample A	0.5	0.67	0.32/0.93
PVP Sample B	1.0	1.03	0.61/0.86
PVP Sample C	1.5	2.46	0.65/0.91
PVC Sample D	0.5	0.47	0.49/0.81
PVC Sample E	1.0	0.73	0.70/0.81
PVC Sample F	1.5	1.80	0.70/0.93
PS Sample G	0.5	0.45	0.45/0.47
PS Sample H	1.5	0.88	0.36/0.52
PS Sample I	2.0	1.33	0.51/0.73
PS+PVP Sample J	1.0+1.5	3.22	0.97/0.96
PS+PVC Sample K	1.5+0.5	2.04	0.59/0.85
PVP+PVC Sample L	1.5+0.5	2.52	0.98/0.99

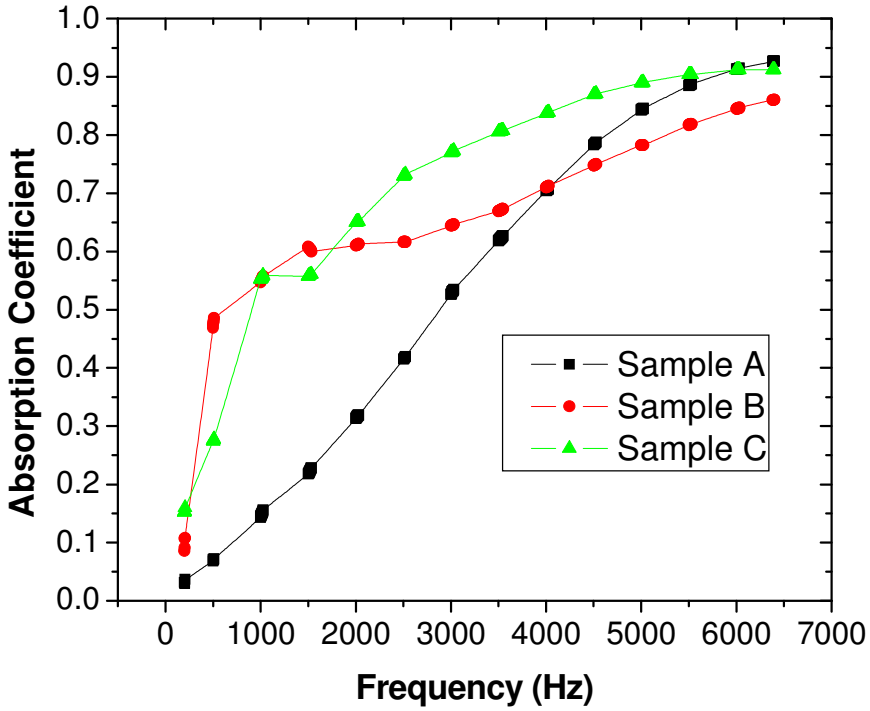

Figure 7-3. Sound absorption coefficient values of PVP fiber samples (A, B, and C) as a function of frequencies between 0 and 6,400 Hz.

The second set of sound absorption tests was conducted on PVC fiber samples with diameters ranging from 200 to 350 nm. Figure 7-4 shows the results of sound absorption tests conducted on 0.5, 1, and 1.5 g of PVC fibers (D, E, and F, respectively) as a function of frequency. As the diameters of the fibers were reduced, the sound absorption coefficient values drastically increased. Unlike the previous test, the sound absorption coefficient values also increased as the weight of the PVC fiber samples increased. This may be related to the high surface area of electrospun nanofibers and chemical structures of the polymer. Additionally, flow resistivity, tortuocity, porosity, viscoelastic changes, thermal characteristic length, surface impedance, and/or viscous characteristic length may be changed at nanoscale [106,115]. Future studies will focus on this issue to identify the real mechanism(s).

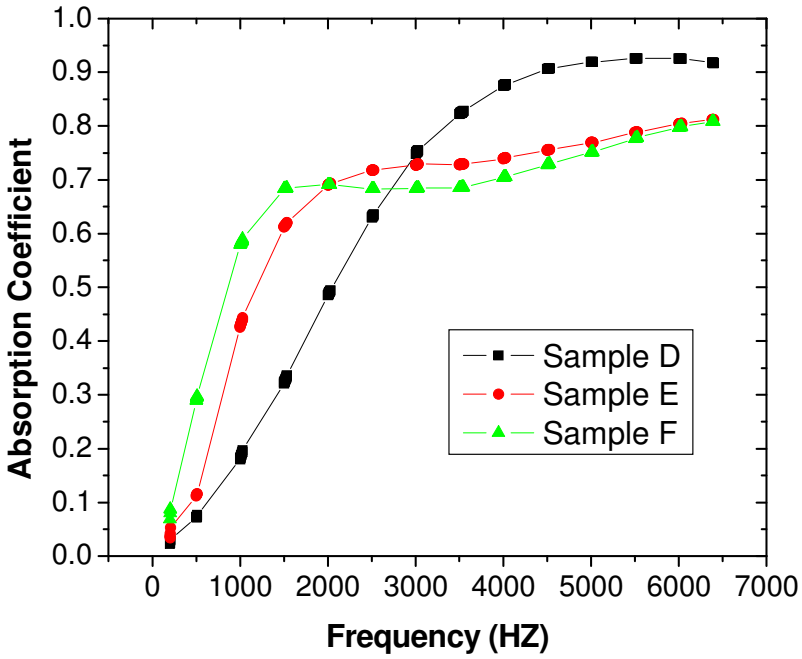

Figure 7-4. Sound absorption coefficient values of PVC fiber samples (D, E, and F) as a function of frequencies between 0 and 6,400 Hz.

The third set of tests was conducted on PS fiber samples (G, H, and I) that have larger fiber diameters (between 2 and 10 μm). Figure 7-5 shows the sound absorption coefficient values of 0.5, 1.0, and 1.5 g of PS fiber samples (G, H, and I) as a function of frequency. As shown, larger fibers have lower sound absorption coefficients. Additionally, samples H and I present the higher absorption coefficients at around 1,000 Hz and then are considerably reduced. The reason may be the reflection of the sounds at that frequency range, as well as change in air velocity and flow resistivity of the PS fibers. Overall, this may indicate that surface area and polymer type can be important parameters in sound absorption.

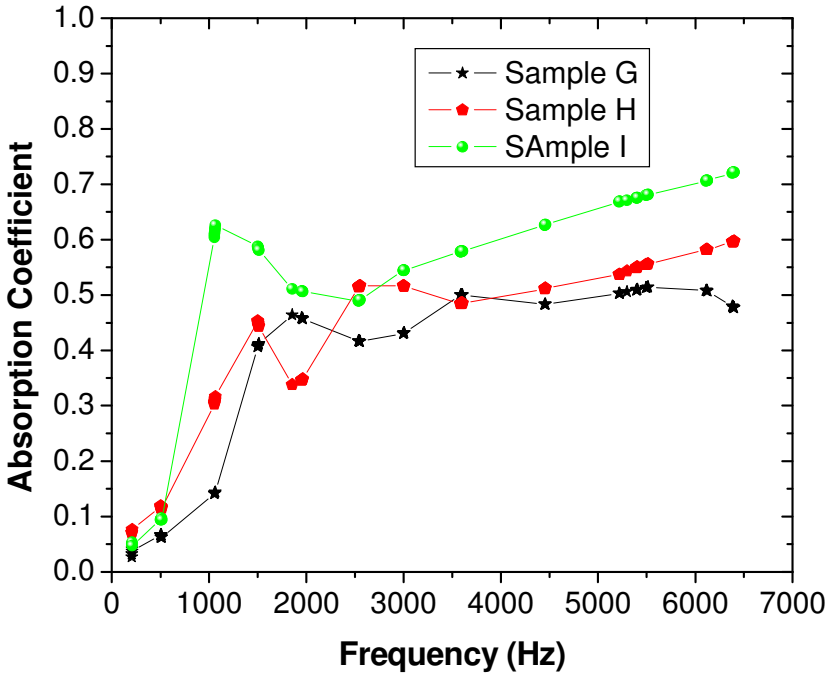

Figure 7-5. Sound absorption coefficient values of PS fiber samples (G, H, and I) as a function of frequencies between 0 and 6,400 Hz.

In the last series of tests, these three fibers were combined at different weight ratios in order to determine the polymer and weight effects on the sound absorption behavior of the fibers. Figure 7-6 shows the sound absorption coefficient values of electrospun fibers: Sample J (PS+PVP), Sample K (PS+PVC), and Sample L (PVP+PVC) as a function of frequencies between 0 and 6,400 Hz. As can be seen, heavier and thicker fibers significantly increased the sound absorption coefficient values of the samples. For example, sample L offered closer to 1.0 absorption coefficient values at 2.0 g weight of PVP+PVC and 2.52 cm thickness. Porosity is a physical property that depends on the numbers of pores, geometry, morphology, and size [111]. When sound waves or air molecules enter the high surface area porous medium, they dissipate energy as the result of friction between the surface of fibers and air molecules, which possibly increases sound absorption coefficients. As a result, the noise absorption coefficient is proportional to the weight, density, and thickness of the specimen. These initial studies will lead

to a comparative investigation of other polymers and their sound absorption properties at different conditions.

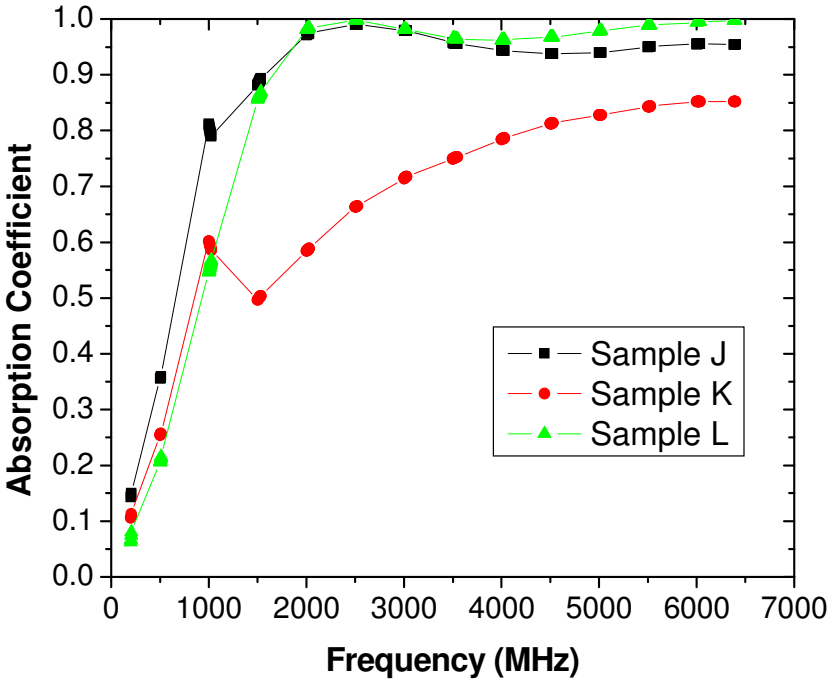

Figure 7-6. Sound absorption coefficient values of electrospun fibers: Sample J (PS+PVP), Sample K (PS+PVC), and Sample L (PVP+PVC) as a function of frequencies between 0 and 6,400 Hz.

Unwanted noise is one of the most widespread irritations in modern society and constitutes a real danger to human health [115]. For this reason, producing materials for noise/sound control has increased as a result of technological changes and product requirements in many areas, including aircraft and space craft, ground and marine transportation vehicles, buildings, and manufacturing facilities [106]. These materials include fibers, foams, cavities, composites, and other solid and liquid structures of various types and shapes. It has been reported that the absorption of sounds at various levels and frequencies is difficult using existing technologies [111]. Although significant progress has been made during the last few decades to improve the efficiency of sound absorption and weight reduction, the problems have not yet been

solved relative to higher sound absorption and cost-effective methods. This thesis proposes an alternative material that can be lighter and more efficient for sound absorption of interior noise of aircraft, as well as other modes of transportation and infrastructures.

7.6 Conclusions

A number of PVP, PVC, and PS fibers were produced using the electrospinning method for sound absorption purposes. SEM images show that the fiber diameters are usually between 200 nm and 10 μm. Impedance tube studies proved that high-surface-area and flexible fibers absorb the sound in larger frequency ranges, depending on the weight and thickness of the fibers. Sound energy loss increases as the surface friction between the fiber and air molecules increases, which in turn increases the sound absorption coefficient. Consequently, these high-surface-area fibers could be used as alternative materials in reducing the interior noise of aircraft, as well as many other noise-control applications.

CHAPTER 8

MAGNETIC PROPERTIES OF PVP AND PAN NANOCOMPOSITES FIBER

8.1 Introduction

The magnetic study of different materials is a major topic of material science today because of its broad industrial applications. With the advancement in technology and engineering, the need for specific magnetic materials will rise. The electrons are magnetic with an intrinsic magnetic dipole strength of one Bohr magneton (m_B) [116]

$$m_B = 9.27x\,10^{-24} A.m^2 \quad (8.1)$$

The motion of electrons in an atom resembles the flow of current in a circular path, which can be regarded as an orbital dipole moment. Orbital dipole moments are affected by external magnetic fields as well as the neighboring atoms' dipolar moments. All materials can be categorized as either paramagnetic, diamagnetic, ferromagnetic, antiferromagnetic, or ferrimagnetic [116].

The atoms of paramagnetic materials have permanent magnetic dipole moments. These dipole moments are not aligned to create a strong magnetic field. These materials have positive magnetic susceptibility such that their magnetic dipole domains try to align in the presence of an applied external magnetic field but cannot achieve perfect alignment due to randon thermal motion of the domains. These materials do not retain magnetic properties when the external magnetic field is removed. Paramagnetic materials include magnesium, molybdenum, lithium, and tantalum. They lack strong ferromagnetic effects, and their susceptibilities are low, ranging from 10^{-5} to 10^{-3}.

Ferromagnetic materials have a large positive susceptibility and are the most magnetically active materials. Their magnetic susceptabilities ranges from 10^3 to 10^6. They

display strong attraction to magnetic fields, and they are capable of retaining their magnetic properties even after the external field is removed. Ferromagnetic materials have atoms with permanent dipole moments. When these atoms are combined in a structure, their bond lengths allow the electrons to be in a lower energy state because of the alignment of dipoles between neighboring atoms. The alignment is not uniform inside the material, since the alignment of a dipole through the sample would certainly lead to a strong magnetic field and consequently high energy states. If the structure is broken into microscopic regions, each region has an internal alignment of dipoles, but the interregional alignment is randomly oriented, thus making the overall magnetic field weak. These domains are termed magnetic domains. The behavior of domains under the influence of a magnetic field is the fundamental aspect of the construction of permanent magnets. When a ferromagnetic material is placed under the influence of a magnetic field, the domains are combined into large domains, and they align themselves with the external field. As the external field is removed, the alignment of domains and consequently magnetic field does not disappear completely. This is called magnetic hysteresis [116]. The residual magnetization depends upon the microstructure or phase-purity. The magnetic memory is represented by a curve called the magnetic hysteresis curve, as shown in Figure 8-1.

The retentivity is the magnetization after the external field is removed. Coercivity is the reverse field needed to change the magnetization to zero after being saturated. The materials with high retentivity and high coercivity are called hard magnets, and materials with low retentivity and low coercivity are called soft magnets. Although retentivity and coercivity play an important role in determining the strength of permanent dipoles, the actual magnitude is determined in terms of the amount of stored energy during the magnetization process. The stored energy is called the energy product and is denoted by $(BH)_{max.}$

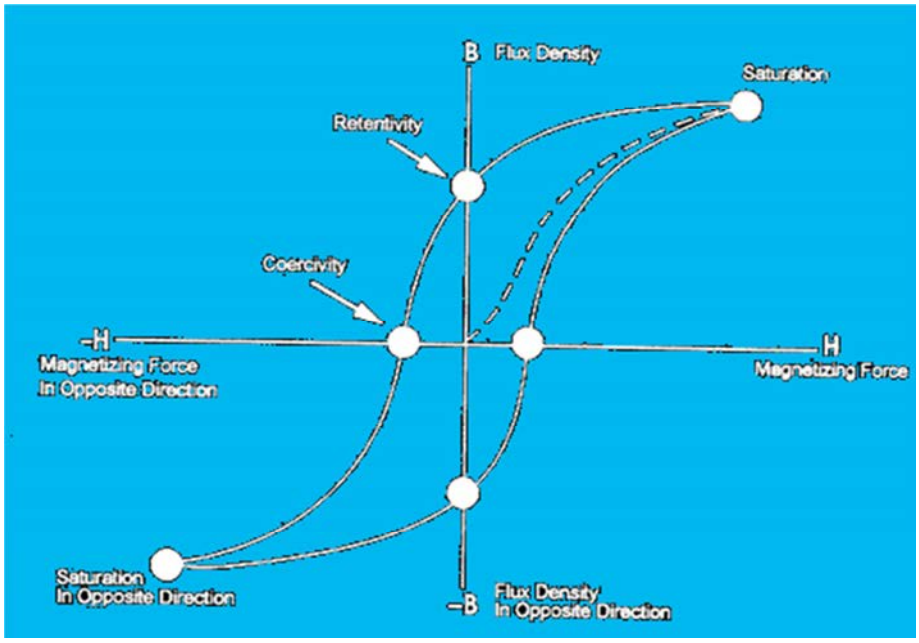

Figure 8-1. Magnetic hysteresis loop [116].

8.2 Evaluation of Magnetic Materials

Before the mid-1930s, the only permanent magnets were special steels. During the 1930s, some improvements in the magnetic strength of these materials were made. The major developments in this field came in the 1940s and 1950s with the introduction of aluminum-nickel-cobalt alloys in the 1960s, the development of rare earth/cobalt alloys provided some advancement in this field. The real technological advancement came in the 1980s with the development of neodymium-based magnets. Today, permanent magnets have magnetic strength 100 times greater than those available in the 1930s. These magnetic materials are capable of making small, powerful motors.

Neodymium has excellent magnetic properties at room temperature and an intrinsic spin reorientation process at 150^{0}K, which makes it unacceptable for low-temperature applications. To overcome this problem, researchers around the globe replace neodymium with praseodymium [116].

8.3 Motivation and Objectives

In this chapter, magnetic properties of NiZn ferrite-based nanocomposite fibers were determined. From Mössbauer spectroscopy, it was determined that at 20^0K, the spectrum consists of well-defined sextants, but at 300^0K, the hyperfine field completely collapsed. This phenomenon is called superparamagnetic relaxation. The vibrating sample magnetometer study confirmed the superparamagnetic behaivor of nanocomposite fibers.

In squid analysis, magnetization of PVP and PAN containing different amount of ferrite nanoparticles was obtained at 1,000 G. The split between zero-field-cooled (ZFC) and field-cooled (FC) curves for each set corresponds to the blocking temperature (T_B) (20^0K) of the magnetic nanoparticles. In the ZFC curve, magnetization increases as temperature increases and reaches the eqilibrium value of magnetization at some temperature known as T_B. This behavior is referred to as superparamagnetism, which is the main feature of magnetic nanoparticles.

8.4 Mössbauer Effect

The Mössbauer effect can be defined as the recoilless emission of gamma rays by some radioactive nuclei of crystalline solid and subsequent absorption of gamma rays by other nuclei. This phenomenon was first discovered by German physicist Rudolph Mössbauer in 1958, a Nobel laureate in 1961. The Mössbauer effect [116] is the foundation of Mössbauer spectroscopy, which can be applied to derive valuable information about nuclei and their electromagnetic environments. Mössbauer spectroscopy is a versatile technique that is used to provide information in many areas of science such as physics, chemistry, biology, material science, and metallurgy. It can give very precise information about the chemical, structural, magnetic, and time-dependent properties of a material.

It is known that a nucleus consists of protons and neutrons arranged in different energy levels. In radioactive nuclei, either neutrons and/or protons are in high energy levels from which they decay and emit different kinds of radioactivity. Energy levels in the nucleus come in certain sizes. For example, a ^{57}Fe nucleus emits or absorbs a gamma ray with energy of 14.4 Kev [117]. A gamma ray with energy of 17 Kev is useless to this nucleus. If a nucleus emits a gamma ray of 14.4 Kev, the energy of this gamma ray is not exactly 14.4 Kev, because the nucleus recoils back while emitting gamma rays. If a nucleus builds into a solid, then it will not recoil while emitting or absorbing gamma ray provided the coils are strong enough to hold the nucleus in its place.

According to the laws of momentum, final and initial momentum should be equal. However, in Mössbauer analysis, gamma rays are absorbed and emitted by nuclei without recoil (without momentum). This contradiction can be understood by viewing the large structure of materials and quantum mechanical properties of nuclei.

The nucleus and atoms are treated the same in quantum mechanics. However, there is a significant difference between nuclear binding and Coulomb binding of atoms: both atom and nucleus are a system of particles subject to the same quantum mechanical interactions. The nucleus has quantized energy levels. However, the nucleus generally occupies a ground state energy level, but it can be excited to higher energy levels and take the transition back to lower levels. During this process it emits or absorbs photons. Similar to electronic transitions, the transitions between nuclear states takes place through emission and absorption of radiation, both of which require recoil. In the case of emissions from a nucleus, the nucleus recoils in the opposite direction of the emitted radiation with equivalent momentum. The emitted energy is less than the total transition energy of states. Similarly, the absorption of gamma rays should have higher energy than the actual state transition energy because part of the energy will be lost due to

recoiling of the nucleus, which will be in the direction of momentum of the gamma rays and equal in magnitude [116].

$$E_0 = E_r + E_\gamma \tag{8.2}$$

$$E_r = \frac{1}{2} M v^2 = \frac{P_n^2}{2M} \tag{8.3}$$

where "E_0" is the excitation energy of the nucleus, "E_r" is the energy of the emitted gamma rays, and "E_r" is the total recoil energy.

Generally, the transition occurs within a range of energies and is determined by the width of transition line defined by the lifetime of the state according to the Heisenberg uncertainty relation:

$$\Delta E \Delta t = \hbar \tag{8.4}$$

There is no internal re-absorption between the same two nuclei since the recoil energy loss during emission and extra energy needed for absorption will lead to minimal overlap between required and produced gamma rays energies. The lattice structure of the crystalline solid is considerably larger than a single nucleus. Its recoil kinetic energy and, as a result, recoil moment are zero. Therefore, emission and absorption lines of nuclei overlap, and the produced gamma rays for every process carry the exact transition energy. The emitted gamma particles from one nucleus can excite another identical nucleus. This process of internal re-excitation of the nucleus is called the resonant absorption, the fundamental aspect of Mössbauer spectroscopy [116].

The resonant absorption is not only possible for a single value of energy but a range defined by the absorption line width. These line widths can be determined by examining the energy profiles of nuclear transitions.The energy of incident gamma particles can be shifted by miniscule increments by inducing Dopper shift [116]. By changing the Doppler velocity, a range

of energies can be scanned, revealing the natural line width of nuclear transitions as well as temperature shifts and hyperfine structure. The Doppler broadening of line width can be given by

$$\overline{D} \cong 2\,\frac{v_0}{c}\,E_0 \tag{8.5}$$

Figure 8-2 shows the emission and absorption lines of a free atom with excitation energy E^*, recoil energy E_1, and Doppler shift D.

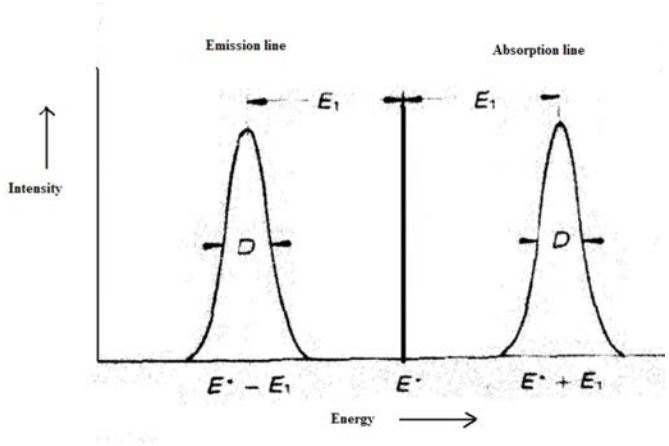

Figure 8-2. Emission and absorption lines of free atom with excitation energy [116].

Figure 8-3 shows emission and absorption lines of an isolated atom with excitation energy, resonance energy E_r, recoil effect R, and Doppler width δ.

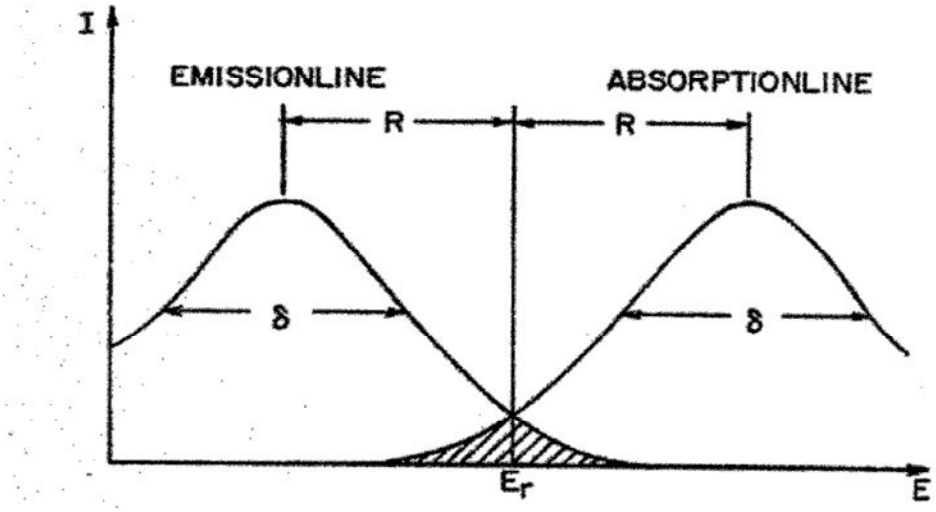

Figure 8-3. Overlap of emission and absorption nuclei energy distribution of free atom [116].

8.5 Mössbauer Spectrum

A number of factors influence the shape and numbers of absorption lines in a Mössbauer spectrum. All of these factors must be understood in order to develop a comprehensive understanding of it.

8.5.1 Recoil-Free Fraction

The depth of Mössbauer resonance absorption lines can be determined by the fraction of recoilless emission of gamma rays in the source and resonant absorption cross-section in the absorber. Although there could be some fractions due to Compton scattering and the photoelectric effect, they have minor influence. Recoil-free fraction is a term that is used to define the processes of both the source and the absorber. In case of the source, it is used to define the fraction of gamma rays that is emitted without recoil. For the absorber, it signifies the fraction of gamma rays absorbed without recoil. The structure of an atom in the crystal lattice plays a role in the process that distributes the momentum of the absorbed particles throughout the lattice. In solid-state physics, the absorption of momentum is defined by the lattice vibration. These lattice vibrations are termed phonons. In solid-state physics, the recoil-free fraction is determined by the phonon spectrum in crystals, or Debye theory [116]. This fraction is defined as the Debye-Walker factor:

$$f = exp(-\frac{E_\gamma^2}{\hbar c^2}\langle x\rangle^2) \tag{8.6}$$

where "E_γ" is the energy of gamma particles, and "$\langle x\rangle^2$ " is the mean square displacement of the atom in its thermal vibrations about its origin [116]. According to Debye theory, a large f, or recoil-free fraction, would be possible only for small gamma ray energy, or tightly bound atoms.

The thickness of the absorber is also very important. If the absorber is made too thin, there would not be enough absorbed nuclei in the path of the gamma rays to ensure interactions.

However, the increased thickness of the absorber would lead to an increase in the probability of interaction with recoil. Therefore, if the thickness of the absorber is taken into account, the fraction of the recoil-free interactions at the absorber is not equal to that of the source. It is necessary to apply a correction for thickness to the Debye model for the lattice apparatus that has significant thickness.

8.5.2 Natural Line Width

Since the nuclear decay at the source is exponential, it is possible to show that the energy distribution of the gamma particles produced is Lorentzian, as shown in Figure 8-4 [116]:

$$N(E) = \frac{N_0}{(E-E_\gamma)^2+(\frac{\Gamma}{2})^2} \tag{8.7}$$

where "E_γ" is the peak of energy distribution, and "Γ" is the full width at half maximum of the emission line and can be defined as

$$\Gamma = \hbar/\tau \tag{8.8}$$

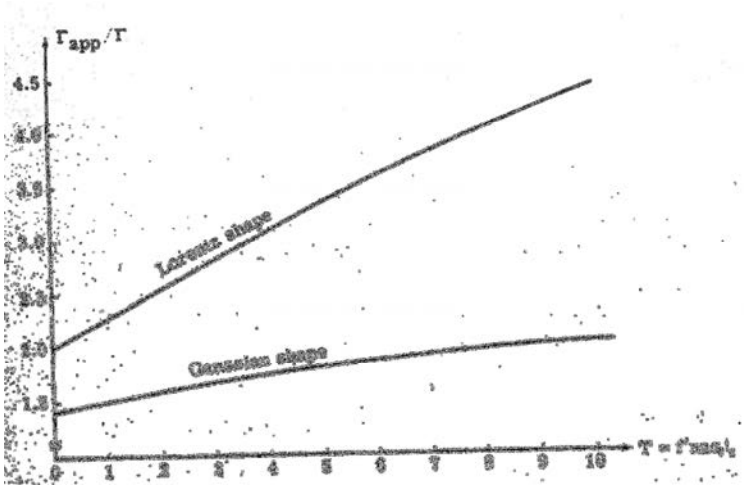

Figure 8-4. Lorentzian shape [116].

The absorption lines are also Lorentzian in shape with the same line width Γ (Figure 8-4). The emission from the source and absorber absorption lines is Lorentzian in shape, and so are the observed lines. The observed line width is not only influenced by the emission and absorption

process but also by the thickness of the absorber. The larger thickness would lead to higher re-absorption in the absorber and an increased percentage of non-resonant absorption as well. Both of these factors would result in broadening the natural line widths.

The lifetime of states also influence the spectral line width. If the lifetime is of the order of 10-^{10}_{S} or longer, an extra-nuclear field can widen the line. If the nuclear lifetime becomes shorter than the inverse of the Debye frequency, then it is impossible to distinguish the recoil-free transition from those with lattice take-up energy [116]. Figure 8-5 shows the emission, absorption, and transmission lines [116].

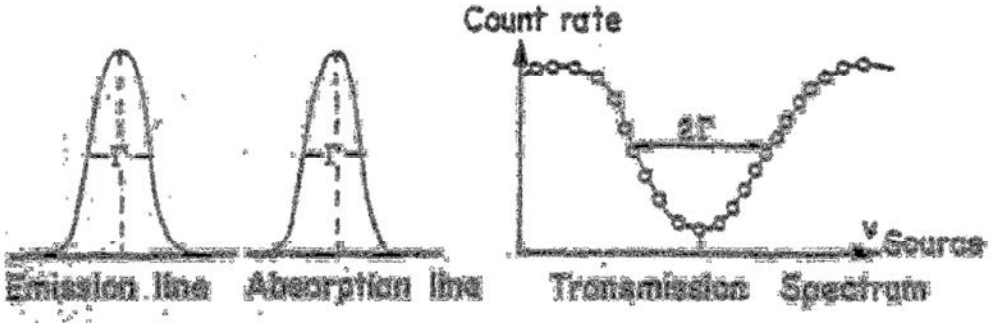

Figure 8-5. Emission, absorption, and transmission lines [116].

8.5.3 Isomer Shift (Chemical Shift)

The nucleus and its electrons interact in several ways, the most common being electrostatic interactions. In nuclear physics, nuclei and electronic systems of atoms are regarded as point charges. Therefore, electronic wave functions do not overlap with the nucleus. Nevertheless, the reality of the wave mechanics of the electronic system of atoms is different. All electrons in general and s-electrons in particular have a small volume but finite possibility of being found within the nuclear volume. This overlap of nuclear and electronic wave functions leads to a correction in energy levels due to Coulomb interaction, which consequently changes the total energy of the system. If the ground and excited states of the nucleus have similar but

non-equal radii, then the overlap of electronic and nuclear wave functions would be different for the two states. If the ^{57}F nuclear charge distribution is the same for the I = 1/2 ground state and the I = 3/2 excited state, then the electrostatic energy of the system of electrons plus nuclear energy would be the same for both cases. In fact, the excited ^{57}Fe nucleus is 0.1% smaller in radius than the ground-state nucleus, which causes the Mössbauer transition energy to dependent on the electron density at the nucleus. This effect produces the so-called isomer shift of the Mössabuer spectrum. The difference between the overlaps of electronic and nuclear wave functions shows a shift in the position of the absorption lines from the resonance energyE_r. Since we know that all the atoms have some level of non-uniform overlap, Mössbauer spectra always show some degree of isomer shift, which can be seen as a shift in the velocity axis (Figure 8-6) [116].

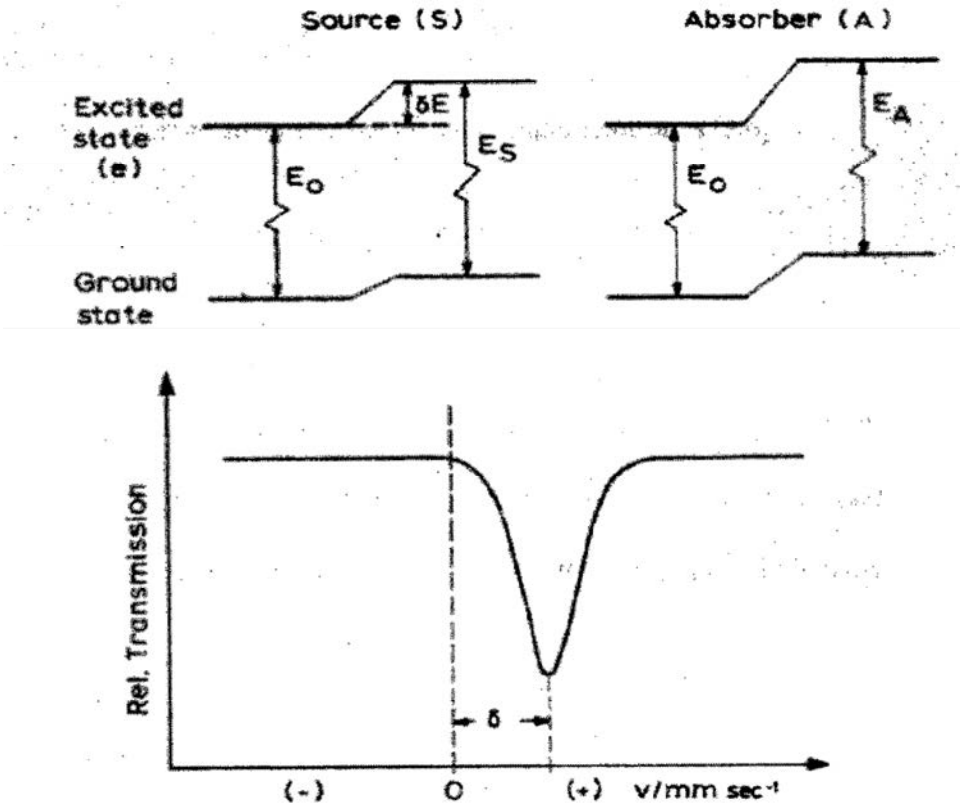

Figure 8-6. Isomer shift and resulting Mössbauer spectrum [116].

8.5.4 Magnetic Hyperfine Interaction and Zeeman Effect

Magnetic splitting of Mössbauer spectral lines are caused by hyperfine magnetic interaction, which is also called the Zeeman effect. Nuclei are composed of neutrons and protons. Nuclei always possess some nuclear charge with an angular momentum. During rotation, the nucleus is accompanied by a magnetic dipole moment. When a nucleus is placed under a magnetic field, the energy states are split, where energies are dependent on the orientation of the nuclear moment with respect to the field. A state with quantum number J splits into 2J + 1 sublevels represented by quantum number m_J. This splitting of energy level is termed as the Zeeman effect or magnetic hyperfine splitting. The hyperfine magnetic field (HMF) from a single electron can be given by [116]

$$H_g = -2\mu_B \left[\frac{8\pi}{3}\Psi^2(0)(s) + \left(\frac{1}{r^3}\right) + \left(\frac{3r(sr)-sr^2}{r^3}\right)\right] \tag{8.9}$$

where "Ψ" is the Fermi contact interaction. The splitting of energy levels brings the possibility of a transition between new states with different energies. As such, the transition spectrum of the nucleus would also be split. The splitting of the transition spectrum between the J = 1/2 and J = 3/2 levels under the influence of the magnetic field for ^{57}Fe is shown in Figure 8-7 [116].

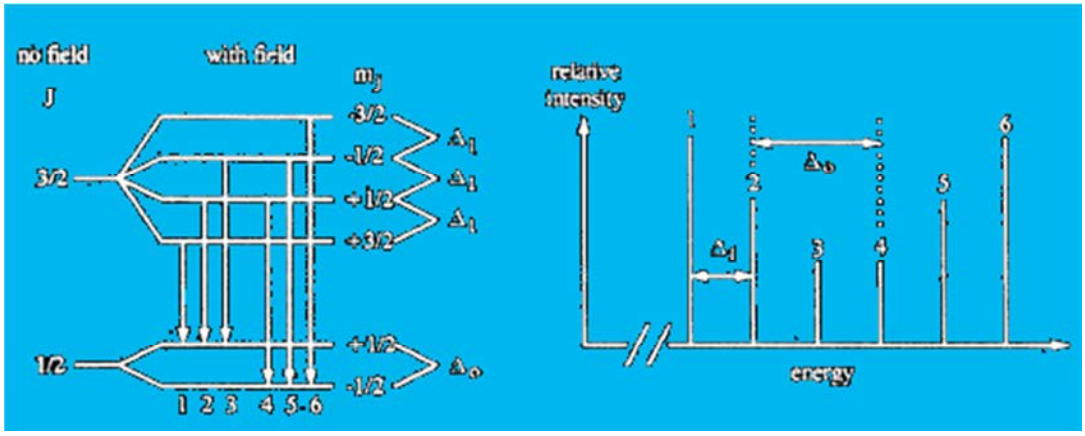

Allowed transitions between Zeeman split J = 3/2 and J = 1/2 levels

Relative energies and intensities for allowed transitions.

Figure 8-7. Zeeman effect [116].

In the above system, there are eight possible transitions. There are also magnetic dipole transitions, according to the selection rules $\Delta m_J = -1,\ 0,\ +1$. Therefore, two of the possible transitions can be excluded, thus leaving six possible transitions lines. The energy separations for these transitions can be given by [116]

$$\Delta_0 = g_0 \mu_N H = \mu_0 H / J_0$$

$$\Delta_1 = g_1 \mu_N H = \mu_1 H / J_1 \tag{8.10}$$

where "μ_N" is the nuclear magneton, g_0 and g_1 are g-factors for J = 1/2 and J = 3/2 levels, respectively.

8.5.5 Quadrupole Splitting

If the effects of thermal agitation are ignored and if there are no thermal vibrations present, the nucleus stays in its stationary position by Columba forces. This means that the electric field at the nucleus must be zero because a non-zero field would induce a nuclear motion. Even though the electric field is zero, there will be a gradient of the electric field due to the symmetry of atoms in a lattice. When a nucleus is in a particular spinning state, it has a slight spherical deformation, and the distribution of charges is no longer spherical. The nuclear quadrupole moment can be defined to siginify the derivative of the nuclear charge from spherical symmetry. The nuclear energy is affected by orientation with respect to the electric field gradient. As shown in Figure 8-8, the energy level with quantum numbers J and m_J is shifted from its original levels by [116]

$$\Delta E = e^2 q\, Q\, \frac{3m_J^2}{4J} \frac{-J(J+1)}{(2J-1)} \tag{8.11}$$

We can assume that the field gradient is axially symmetric. In equation (8.11), "q" is the measure of the field gradient and can be defined as [116]

$$q = \frac{1}{e} \frac{dE}{dZ} \tag{8.12}$$

In ^{57}Fe, the J = 3/2 state is split into two sub-states that are symmetric about the unsplit energy level. The J = 1/2 level will not split because it will conserve the spherical symmetry. Usually, the quadruple splitting is not zero for lower than cubic symmetry structures.

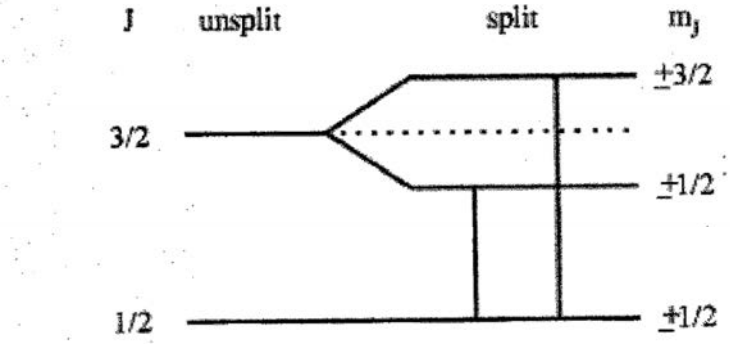

Figure 8-8. Quadrupole splitting [116].

8.5.6 Combined Effect of Quadrupole Splitting and Zeeman Effect

Quadrupole splitting has a weaker effect than the Zeeman effect; therefore, it is generally considered a perturbation of the hyperfine magnetic field. Energy splitting in the HMF due to quadruple moment can be given by [116]

$$|\Delta\varepsilon| = \frac{e^2qQ}{4(3Cos\theta^2-\frac{1}{2})} \tag{8.13}$$

The new spectrum profile due to combined Zeeman and quadrupole effects with non-symmetric splitting are shown in Figure 8-9.

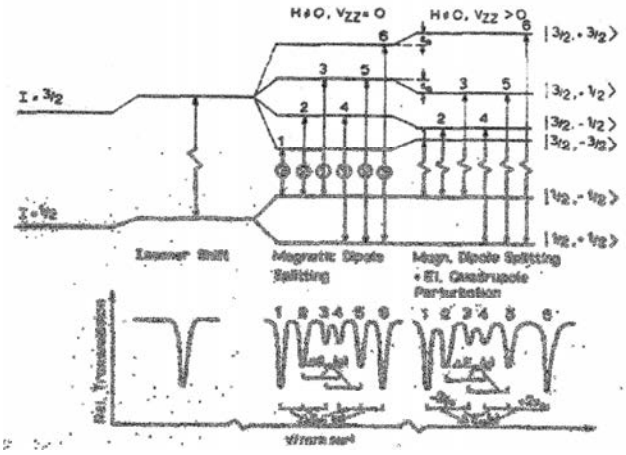

Figure 8-9. Combined effect of isomer shift and quadrupole splitting [116].

8.6 Mössbauer Spectroscopy

The experimental setup for the Mössbauer experiment is shown in Figure 8-10. Individual components, source, sample, detector, and interface are explained in this section.

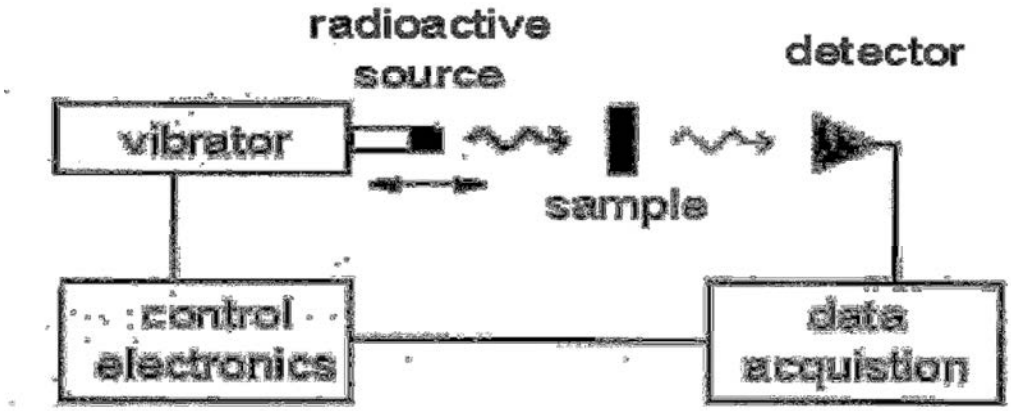

Figure 8-10. Mössbauer spectroscopy apparatus [116].

8.6.1 Radioactive Source

The Mössabuer spectra is a product of absorption and reemmission of gamma rays by radioactive nuclei. The experimental procedure required a radioactive nuclide that is capable of decaying into the required nuclear isomeric state. In this study, ^{57}Co was used as the radioactive source and was embedded in a rhodium matrix. This radioactive material has a 97.81 ns lifetime with 14.4 Kev isomeric state yielding a minimum 0.194 mm/s Heisenberg line width. It is well known that the isomer shift and quadrupole splitting observed in Mössbauer spectra usually fall between 0.2 and 3 mm/s. It was expected that the narrow line width of the cobalt source would yield reasonable resolution, which in turn would facilitate the simplicity of measurement for isomer shifts and quadrupole splitting of the experimental samples. The scheme of the decay of ^{57}Co is shown in Figure 8-11 [116].

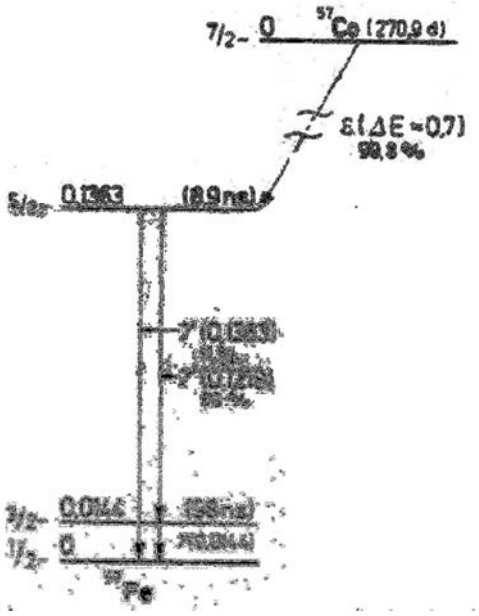

Figure 8-11. Decay of ^{57}Co [116].

8.6.2 Velocity Transducer

A velocity transducer was used to introduce the Doppler shift required for Mössbauer spectra [116]. In this study, the sample was stationary, and the source was set to move back and forth on the transducer. A Doppler Modulator (VT-1200) was used as a velocity transducer. As a results of the back-and-forth motion, the gamma rays produced by source were Doppler shifted both ways in the spectrum. The transducer is capable of producing a number of different functional velocity forms. In this experiment, a constant velocity of -10.6011 mm/s was used to introduce Doppler shift [116].

8.6.3 Detector

The detector consisted of a gamma ray detector and associated electronics. This experiment employed a detector with a Xe-CO_2 proportional counter, which has a beryllium window of diameter 1.5 inches. Once the gamma rays were detected, a signal was sent to a charge-sensitive preamplifier and then to a multifunctional analyzer through a spectroscope

amplifier. The multifunctional analyzer ran in the time mode, storing gamma counts at equal time intervals in each channel [116].

8.6.4 Interface and Data Sampling

A computer interface (Mössbauer Spectrometer MS-1200) was used to control the data sampling and detector operations. The interface (counter) recorded individual data points for each gamma particle observed by the detector, and a spectrum showing all non-interfered gamma rays as background noise and reemission gamma rays as broad emission lines was generated. As the Doppler shift was introduced in the source, the Mössbauer spectra showed two distinct but identical spectra for Mössbauer absorption lines. The two distinct spectra corresponded to the positive Doppler shift velocity as the source moved towards the sample, and the negative Doppler shift velocity as the source moved away from the sample. The computer interface must be programmed in such a way that it includes all velocities, either negative or positive, in its sampling channel in order to collect all data. The calibration of Mössbauer velocity was done with the hyperfine spectrum of a known absorber (pure iron), where the actual positions of absorption lines are known. Once the data was collected, the two sides of the spectrum (positive and negative velocities) were folded together on top of each other to create the actual Mössbauer absorption spectrum of the sample [116].

8.6.5 Absorber

The absorber thickness has significant impact on the quality of the resulting data and must be adjusted for optimum results [116]. If the thickness is too large, the Mössbauer spectra will be skewed by the internal reabsorption process, resulting in broadened absorption lines and reduced spectral resolution. Excessively thick absorbers generally increase the non-resonance scattering and generate increased noise at the detector level. However, thin absorbers reduce the

actual data-sampling rate due to reduced absorption and increase the required experimental time significantly. The ideal thickness would produce an optimum signal-to-noise ratio while completing the experiment in a reasonable time.

8.7 Results and Discussions

In this study, Mössbauer absorbers (sample) were prepared by dispersing the fine powder of NiZn ferrites and nanocomposite fibers of PVP and PAN between two pieces of plastic tape. Figures 8-12 to 8-25 show the Mössbauer spectra recorded for NiZn ferrite powder, PVP, and PAN fibers measured over the temperature range of 20^0K–300^0K. From the results, the spectrum at 20^0K consisted of well-defined sextets with broadened lines. It became broader with increasing temperature until a pronounced central peak appeared at 300^0K and the hyperfine field completely collapsed at 300^0K. This phenomenon is known as superparamagnetic relaxation. Superparamagnetism usually occurs in very small magnetic particles (between 20 nm and 30 nm). This phenomenon can be comparable to paramagnetism but on a much larger scale. Paramagnetism is a feature of magnetic substances, ferromagnetic and ferrimagnetic, above their Curie temperatures, and for antiferromagnetic substances above their Néel temperature. It is also categorized for a class of substances having paramagnetic behavior at all temperatures. These substances show magnetic ordering only with an applied field, although their atoms have magnetic moments. This is because the thermal energy is larger than the anisotrophic magnetic energy, which is responsible for the orientation of the moments, resulting in a random orientation. The paramagnetic materials do not have spontaneous magnetization.

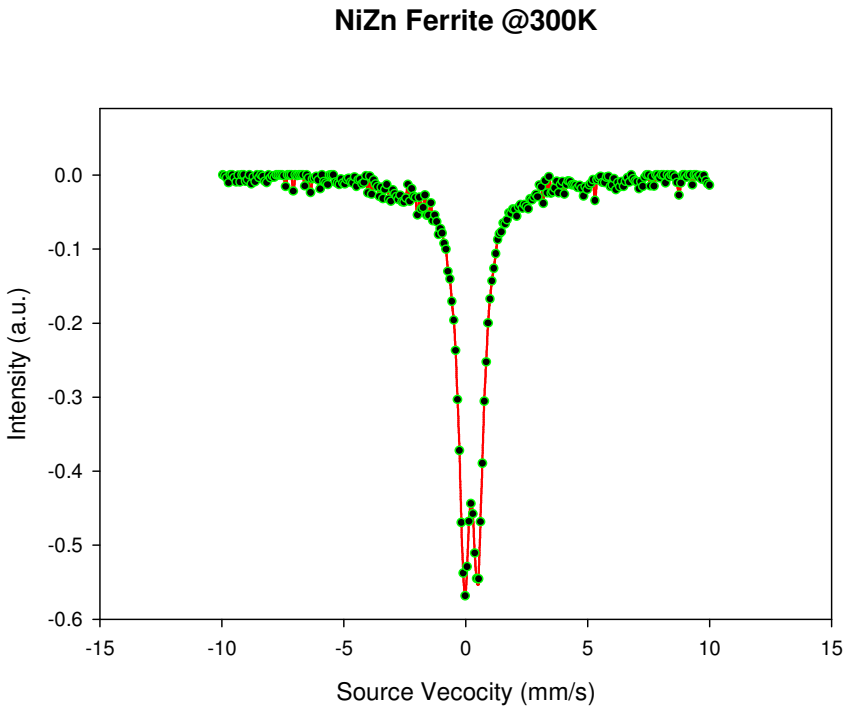

Figure 8-12. Mössbauer spectra for NiZn ferrite at 300^0K.

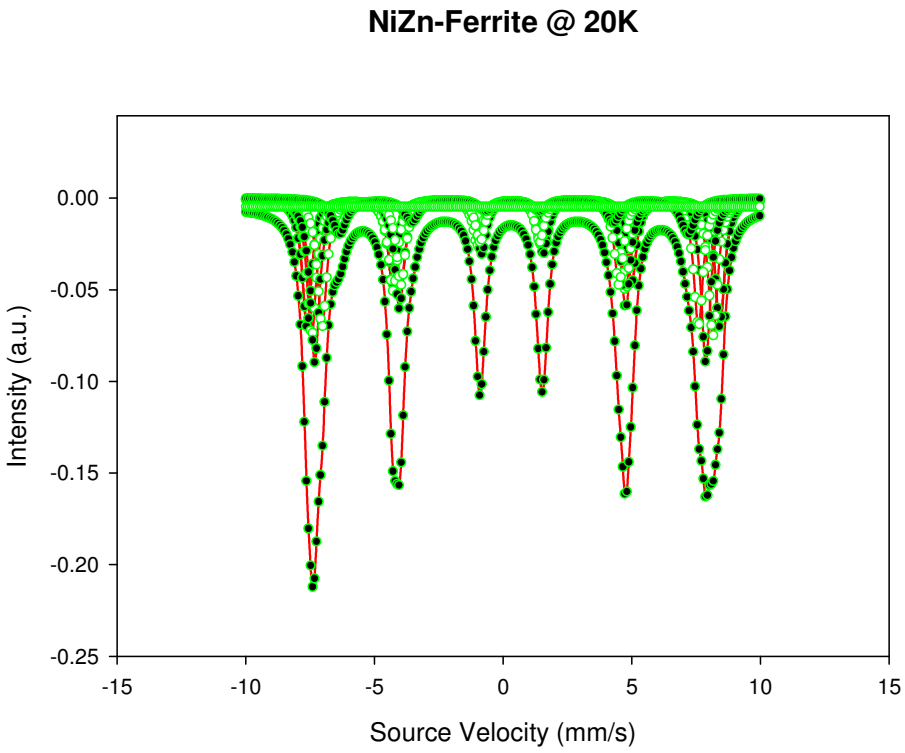

Figure 8-13. Mössbauer spectra for NiZn ferrite at 20^0K.

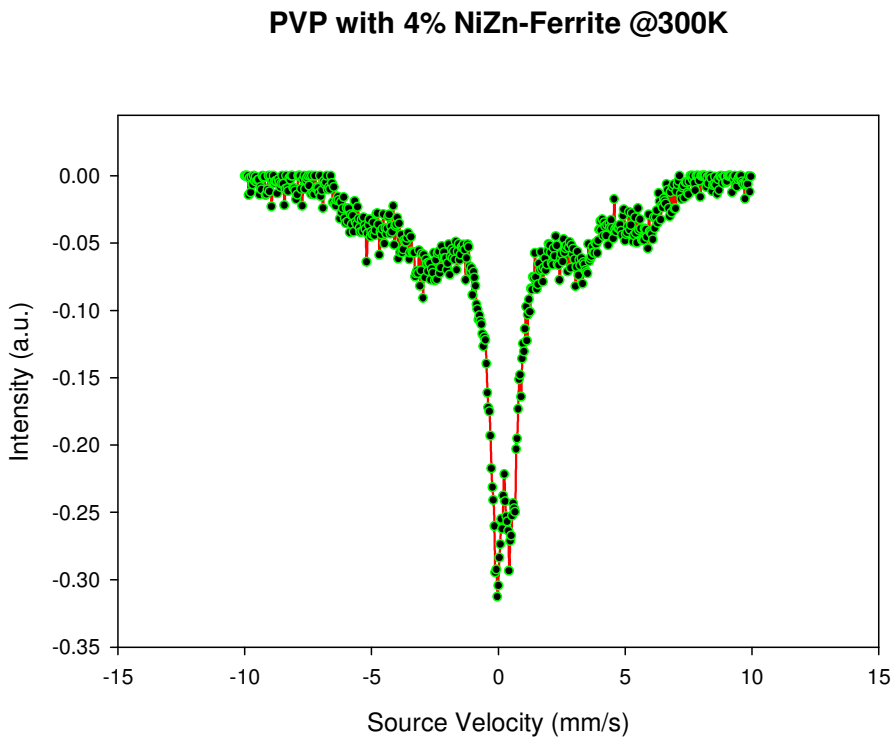

Figure 8-14. Mössbauer spectra for PVP with 4% NiZn ferrite at 300^0K.

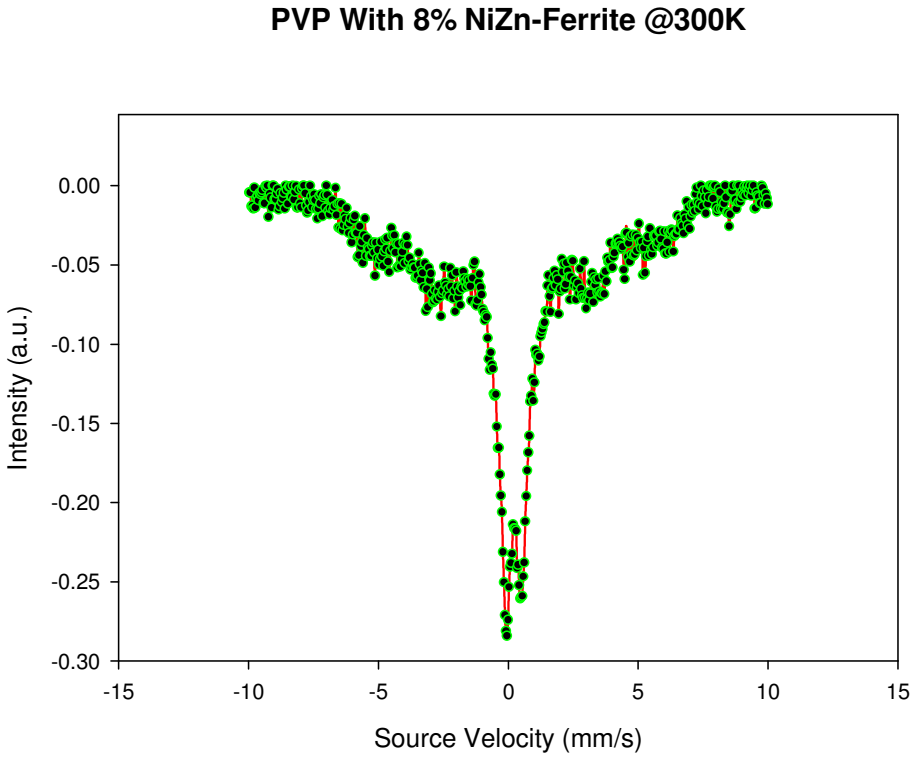

Figure 8-15. Mössbauer spectra for PVP with 8% NiZn ferrite at 300^0K.

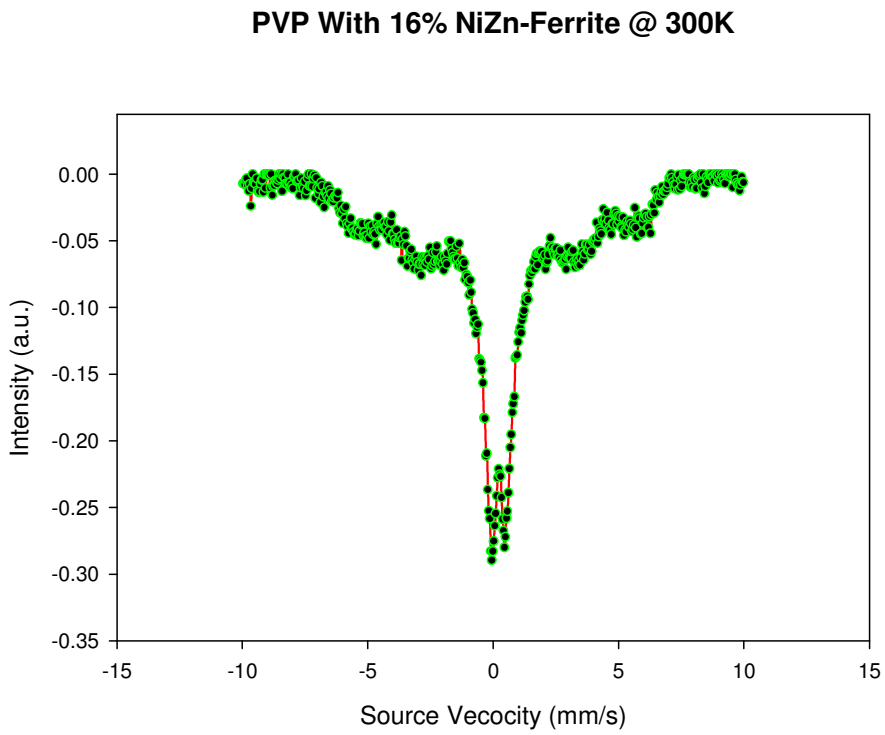

Figure 8-16. Mössbauer spectra for PVP with 16 % NiZn ferrite at 300^{0}K.

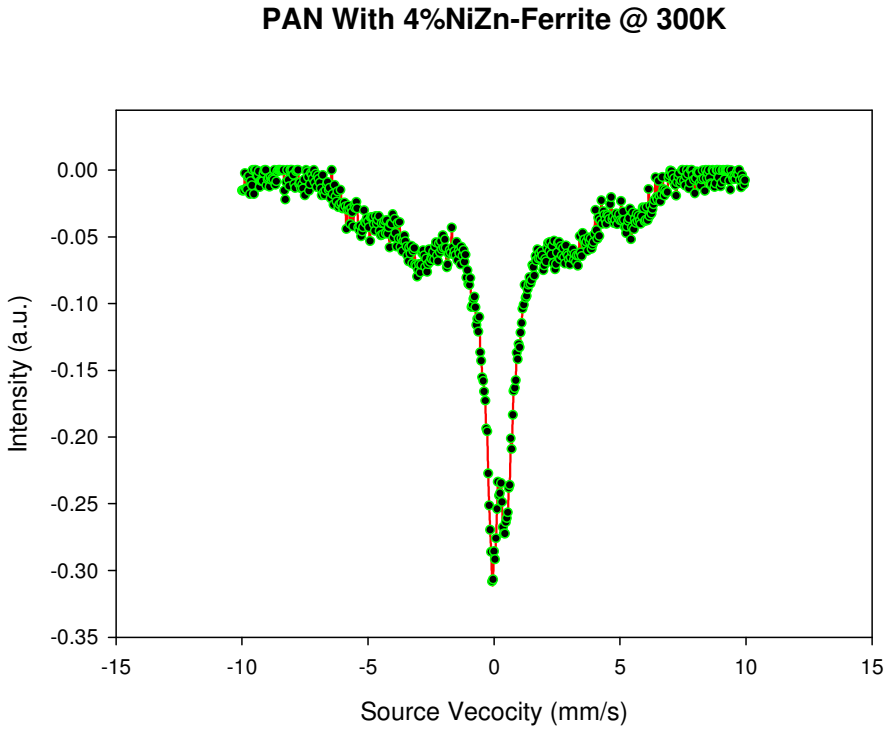

Figure 8-17. Mössbauer spectra for PAN with 4% NiZn ferrite at 300 ^{0}K.

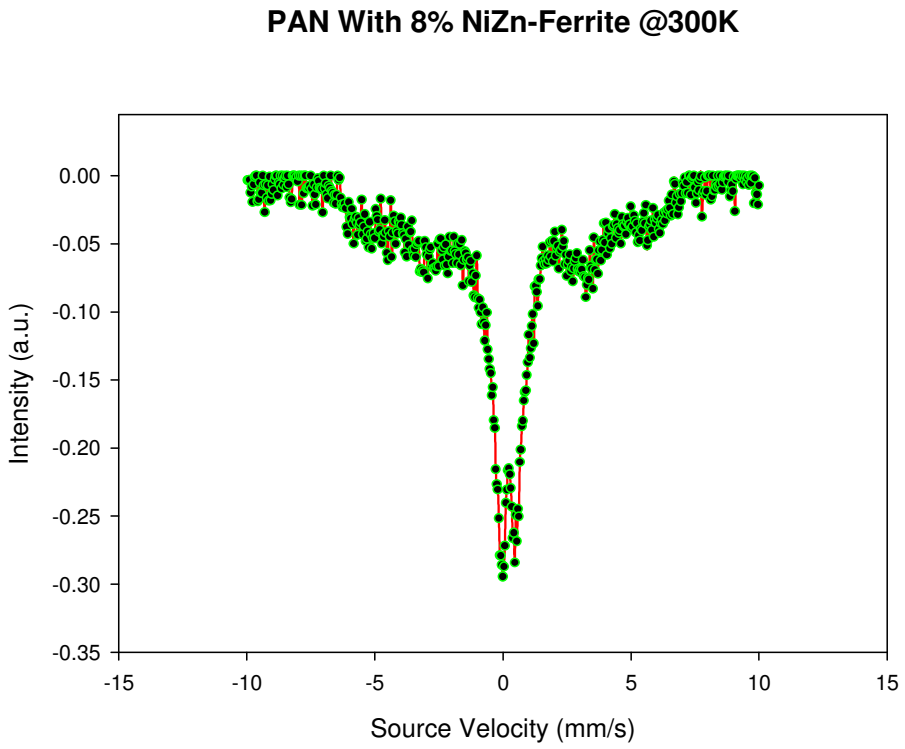

Figure 8-18. Mössbauer spectra for PAN with 8% NiZn ferrite at 300^0K.

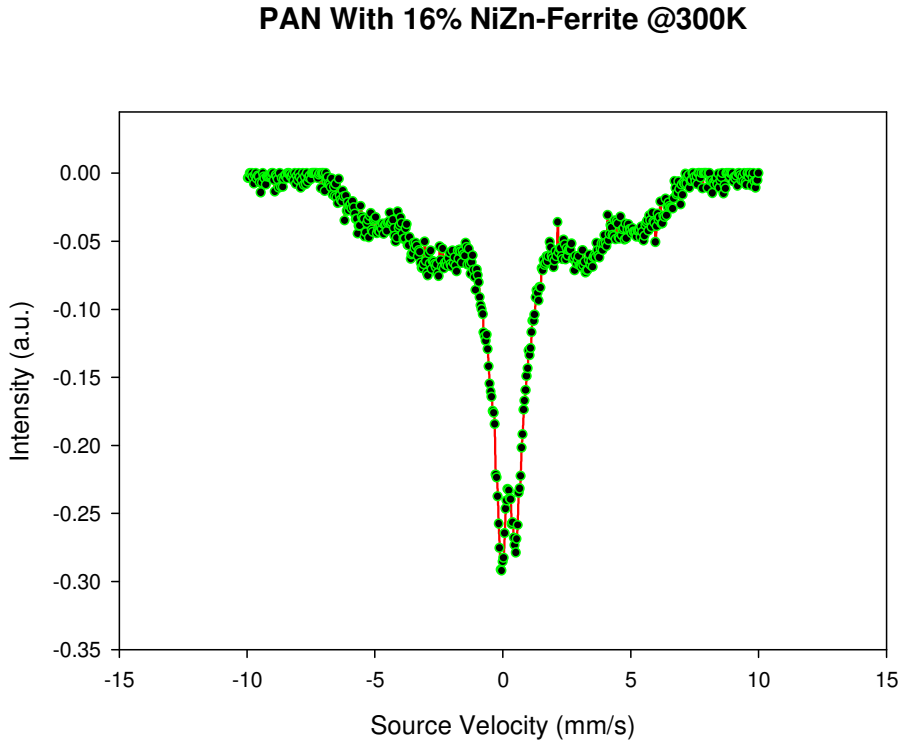

Figure 8-19. Mössbauer spectra for PAN with 16% NiZn ferrite at 300^0K.

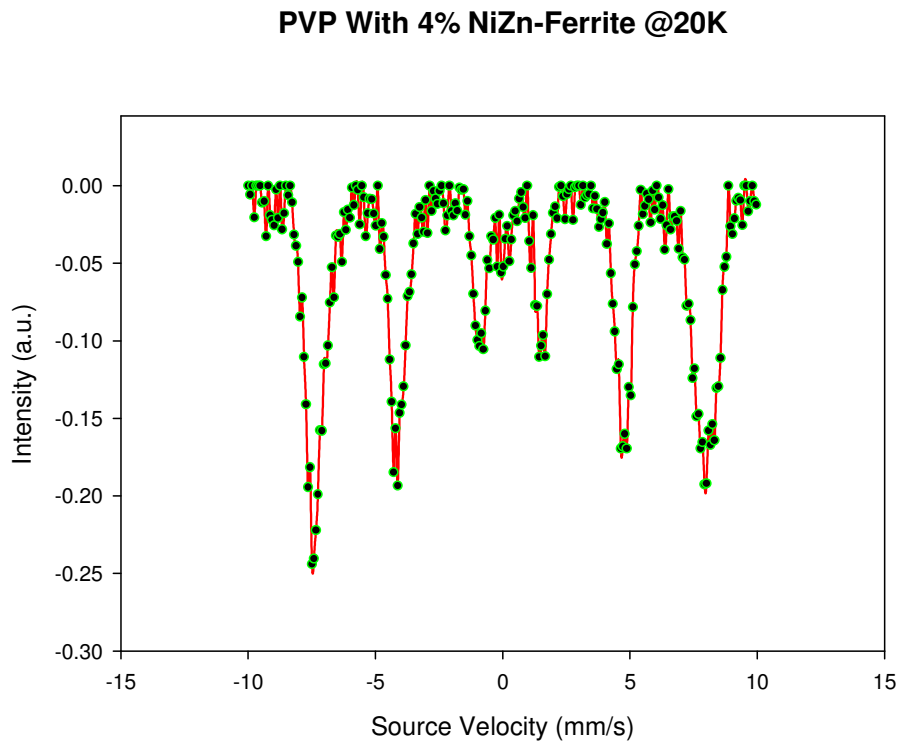

Figure 8-20. Mössbauer spectra for PVP with 4% NiZn ferrite at 20^0K

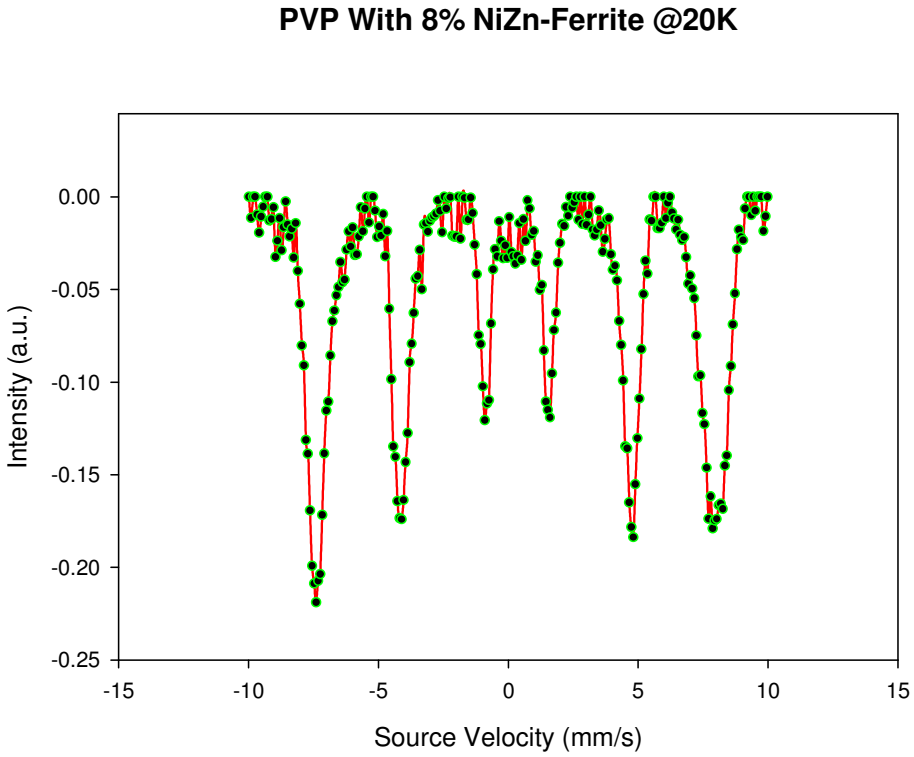

Figure 8-21. Mössbauer spectra for PVP with 8% NiZn ferrite at 20^0K.

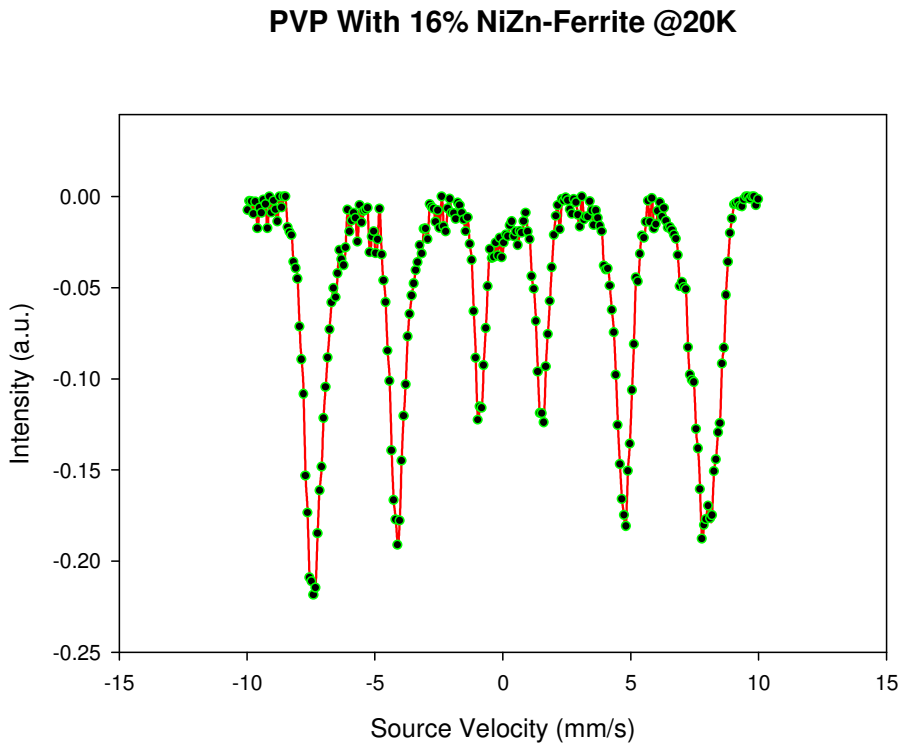

Figure 8-22. Mössbauer spectra for PVP with 16% NiZn ferrite at 20^0K.

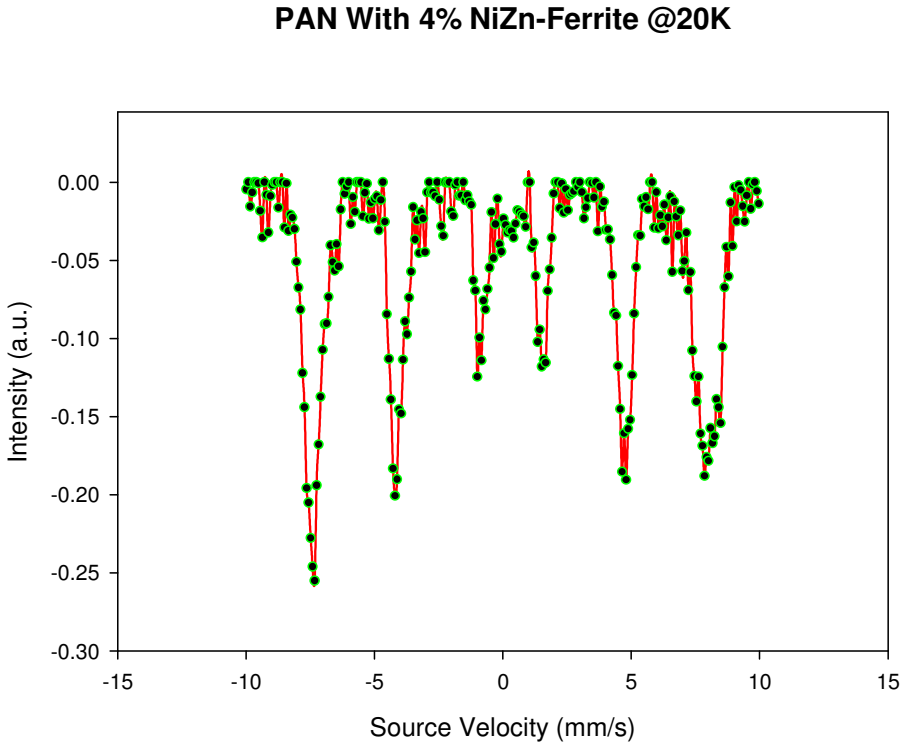

Figure 8-23. Mössbauer spectra for PAN with 4% NiZn ferrite at 20^0K.

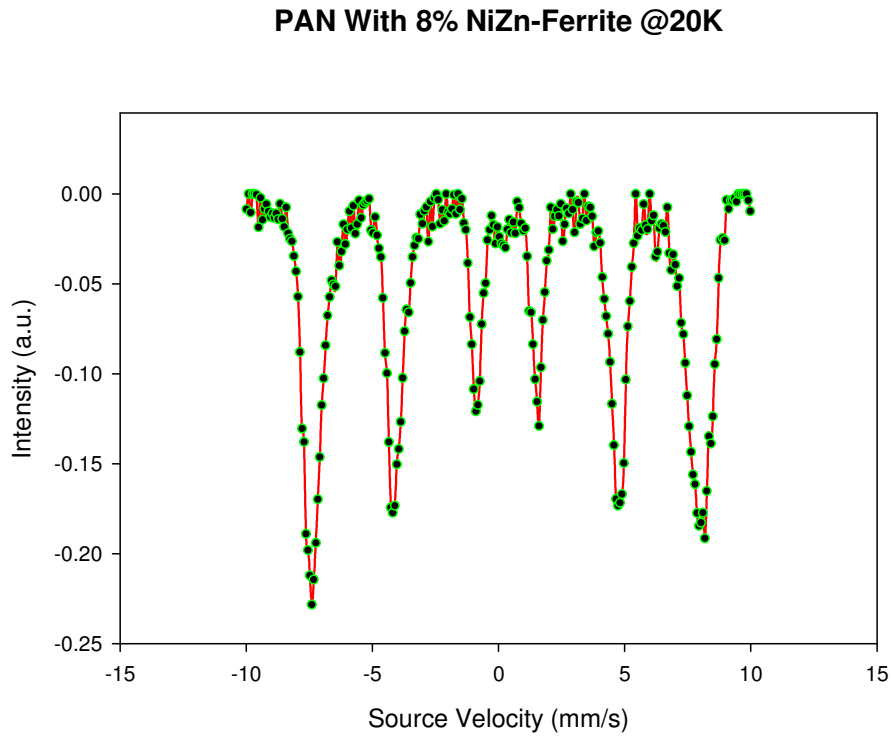

Figure 8-24. Mössbauer spectra for PAN with 8% NiZn ferrite at 20^0K.

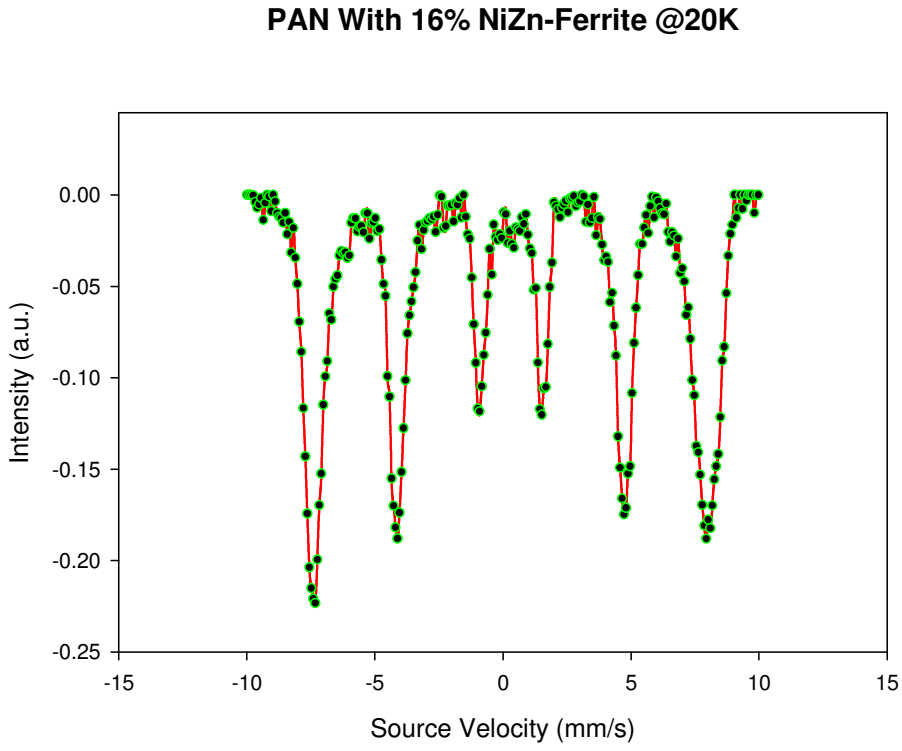

Figure 8-25. Mössbauer spectra for PAN with 16% NiZn ferrite at 20^0K.

The fitting results of hyperfine parameters from the different sites of all samples are listed in Tables 8-1 to Table 8-3. The room temperature Mössbauer spectrum for all samples is typical single-magnetic-domain fine particles with a superparamagnetic state. Superparamagnetism results in the collapse of the outer Mössbauer magnetic sextet toward a singlet or doublet. The temperature above which superparamagnetism behavior appears into six lines is known as the blocking temperature. Below the blocking temperature, magnetic splitting is observed. The room temperature (300^0K) spectra show a broad peak quadruple splitting. The spread of the ^{57}Fe sites can be described by the width of the hyperfine magnetic field distributions at the highest temperatures. The broader distributions at high temperatures can be related to the difference in temperature dependence of hyperfine magnetic fields at different ^{57}Fe environments. When the thermally induced fluctuations in the direction of magnetization are faster than the Mössbauer measurement time, these fluctuations collapse the sextet structure of the ^{57}Fe spectrum. Fine powders usually do not have uniform size distribution and thus do not have a single relaxation time. Therefore, the experimental Mössbauer spectrum is a collection of sub-spectra with different relaxation times. However, the nearly uniform collapse of the spectrum indicates that the distribution of the relaxation time and the associated particle size are narrow.

At 20^0K, thermal excitations dominated and the features of the spectra reflected the chemical distribution on A and B sites of the spinel structure. The spectra were plotted as 5 sextets or doublets in the case of NiZn ferrites, and up to 5 sextets in the case of dispersion of ferrites in polymers. The doublet might be due to impurities in the ferrites. Apparently, the addition of NiZn ferrites has affected the hyperfine parameters of the particles because ferrites are very similar. In the spinel structure, Fe ions occupy either the A site (tetrahedral) or B site (octahedral), which resulted in one sextet from the A site and multiple sextets from the B site,

which was due to the random chemical distribution. The sextet with zero hyperfine magnetic field was due to impurities.

TABLE 8-1

VALUES OF HYPERFINE MAGNETIC FIELD (HMF), QUADRUPOLE SPLITTING (QS), AND ISOMER SHIFT (IS) FOR NiZn FERRITES AT 20^0K

Site	HMF (KOe)	QS (mm/s)	IS (mm/s)	Fraction
1	472.5	-.0.047	0.212	0.33
2	446	- 0.027	0.2966	0.1624
3	479.29	0.102	0.344	0.23
4	475.2	0.0376	0.421	0.272

TABLE 8-2

VALUES OF HYPERFINE MAGNETIC FIELD (HMF), QUADRUPOLE SPLITTING (QS), AND ISOMER SHIFT (IS) FOR PVP FIBERS WITH DIFFERENT WT% OF NiZn FERRITES AT 20^0K

	Site	HMF (KOe)	QS (mm/s)	IS (mm/s)	Fraction
4% NiZn Ferrite	A	501.57	0.0552	0.3457	0.17
	B_1	478.11	0.018	-0.583	0.32
	B_2	422.69	0.025	0.264	0.133
	B_3	458	-0.181	0.326	0.16
	B_4	484	0.026	0.4166	0.188
	6 (Impurities)	0	0.2886	0.0854	0.0294
8% NiZn Ferrite	A	476	0.032	0.041	0.28
	B_1	416.13	-0.044	0.038	0.053
	B_2	500.65	0.032	0.3207	0.2256
	B_3	472	-0.091	0.197	0.295
	B_4	444.9	-0.0747	0.299	0.032
	6 (Impurities)	0	0.052	0.19	0.016
16% NiZn Ferrite	A	476.63	0.058	0.41	0.27
	B_1	475	-0.09	0.21	0.33
	B_2	422.69	-0.07	0.27	0.14
	B_3	411.7	-0.003	0.34	0.05
	B_4	502	0.052	0.35	0.19
	6 (Impurities)	0	0.6	0.22	0.02

TABLE 8-3

VALUES OF HYPERFINE MAGNETIC FIELD (HMF), QUADRUPLE SPLITTING (QS), AND ISOMER SHIFT (IS) FOR PAN FIBERS WITH DIFFERENT WT% OF NiZn FERRITES AT 20^0K

	Site	HMF (KOe)	QS (mm/s)	IS (mm/s)	Fraction
4% NiZn Ferrite	A	473.67	-0.0177	0.211	0.3
	B_1	473.67	0.023	0.383	0.227
	B_2	448.45	-0.261	0.3489	0.131
	B_3	500.29	0.0459	0.361	0.239
	B_4	437.23	0.243	0.3776	0.0761
	6 (Impurities)	0	0.434	0.1385	0.0256
8% NiZn Ferrite	A	478.11	-0.0337	0.1936	0.239
	B_1	481	0.0296	0.41	0.28
	B_2	454.5	-0.10038	0.257	0.1729
	B_3	501.72	0.0502	0.331	0.163
	B_4	426.46	0.0399	0.335	0.132
	6 (Impurities)	0	0.098	0.095	0.013
16% NiZn Ferrite	A	476.63	-0.031	0.218	0.267
	B_1	479.58	0.0267	0.417	0.243
	B_2	454.1	-0.067	0.286	0.16
	B_3	426.46	0.0694	0.33	0.1347
	B_4	501.72	0.0537	0.3356	0.1878
	6 (Impurities)	0	0.53	0.121	0.012

8.8 Vibrating Sample Magnetometer Study of NiZn Ferrite-Based Nanocomposite Fiber

The vibrating sample magnetometer (VSM) is a helpful instrument, which works on the principle of electromagnetic induction. In this instrument, the sample is placed in a uniform external applied magnetic field of an electromagnet. When the sample is vibrated, an electromagnetic field (EMF) proportional to the magnetic moment of the sample is induced in a pickup coil configuration consisting of four coils connected in series, pairwise, and the pair in turn is connected in series opposition. This arrangement of the coil will add the induced EMF because at any time, the sample can recede from one coil while approaching the other coil. By processing the output from the pickup coils, the magnetic moment of the sample can be obtained. The VSM consists of two separate systems: electrical and mechanical. The sample whose

magnetic moment is to be determined is vibrated by a mechanical means in a vertical direction between a pickup coil assembly, which is placed in a uniform magnetic field of an electromagnet. The sample is magnetized in the presence of a uniform magnetic field of the electromagnetic. The dimension of the sample is usually small compared to the signal pickup coil system; therefore, the sample can be considered an oscillating point dipole. If the pickup coil system is placed between the pole pieces of the electromagnetic, an EMF is induced in the coils when the sample is in motion. This induced EMF is proportional to the magnetic moment of the sample. The signal pickup coils consist of four separate coils. The upper two coils are connected in series pairwise, and the two lower coils are connected in the same way. The upper and lower pairs of coils are then connected in series opposite to each other, as shown in Figure 8-26 [118].

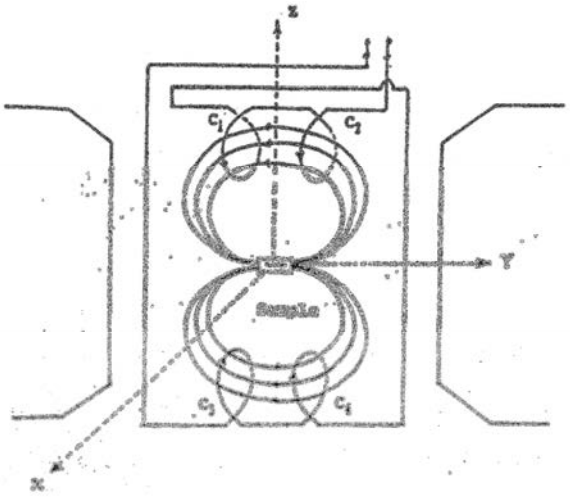

Figure 8-26. Connecting procedure of four pickup coils [118].

The coil configuration is generally called a “transverse” coil geometry. The magnetic flux lines of the oscillating magnetic dipole thread the coils, as shown in Figure 8-27, thus inducing an EMF in the coils. At any instant, the oscillating sample can move away from one pair of coils when it reaches another pair of coils. The upper and lower pairs of coils are connected in series opposition. The resulting EMF in the coils adds up, providing an enhanced signal. This signal is

then recovered for processing. The induced EMF is proportional to the amplitude of vibration and frequency of vibration [118].

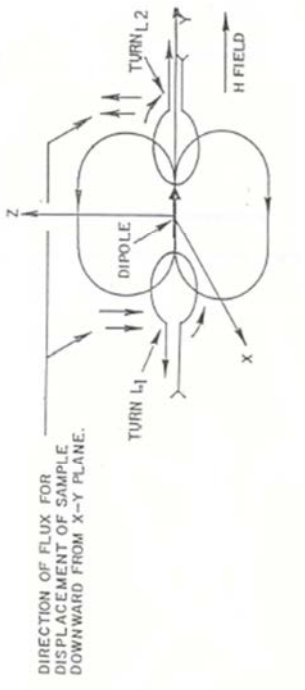

Figure 8-27. Field pattern around vibrating sample [118].

A coil winding with a DC current is placed on the upper half of the sample rod to produce a reference signal. A coil arrangement is placed axially with the vibrating rod and two parts of the coil are wound in series opposition for the same reason as the transverse coils. These coils are used to pick up the reference signal. The sample and reference moment vibrate with the same frequency; therefore, the induced EMF would have the same form. The vibrating sample magnetometer used in this study is shown in Figure 8-28 [118]. The block diagram of the VSM is shown in Figure 8-29 [118].

Figure 8-28. Vibrating sample magnetometer [118].

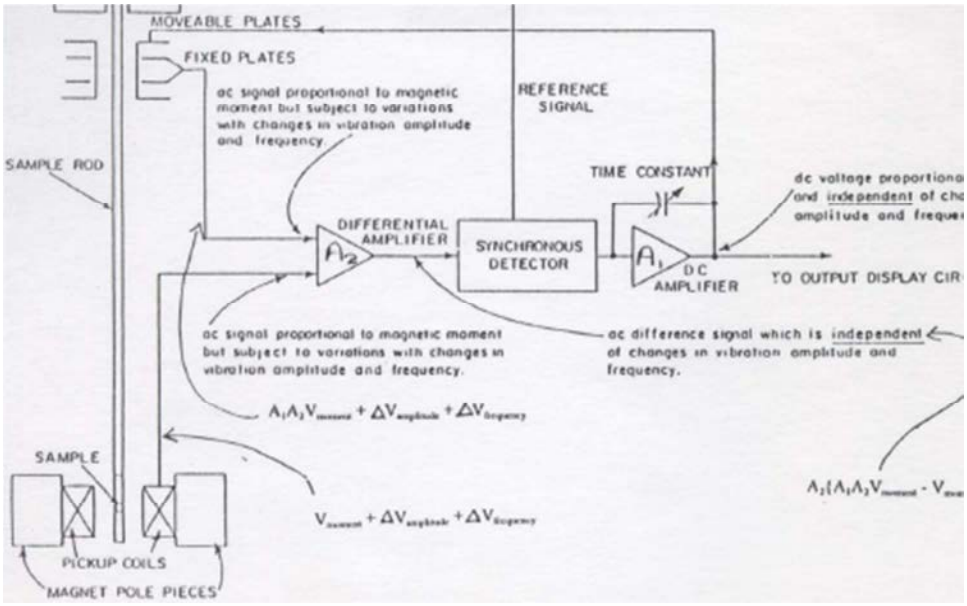

Figure 8-29. Schematic view of vibrating sample magnetometer [118].

It is clear from the block diagram of the vibrating sample magnetometer that the signal from the pickup coil is applied to one of the inputs of a differential amplifier, which has another input from the fixed plate assembly of the vibrating capacitor. A DC voltage is applied to the moving plate assembly of the capacitor. An AC signal is applied to the fixed plate assembly of the vibrating capacitor and from there to the other input of the differential amplified. The capacitor output signal varies with the changes in frequency and amplitude of vibration approximately in the same manner as does the signal from the pickup coils, because the capacitor and sample were vibrated by the same transducer [118].

The variation of frequency and vibration amplitude have nearly the same effect on signals from the pickup coil and fixed plate assembly of the vibrating capacitor applied to the input of the differential amplifier. The differential amplifier possesses the differences between the two input signals, and the effect of variation of frequency and vibration amplitude are cancelled. Therefore, the moment determines the amplitude of the output signal from the differential amplifier. Then this signal is applied to a synchronous detector, where it is compared with a reference signal from the same oscillator, which provides the transducer drive signal. A DC signal which is proportional to the amplitude of moment is applied at the output of the synchronous detector. This DC signal is used in two different ways: part of it is fed back to the movable plate assembly of the vibrating capacitor, and part of it is fed to the output display circuits. The effect of this feedback system is to adjust the DC signal to the degree required to maintain the capacitor output signal at the same degree as the pickup coil signal. For samples having weak moments, the feedback DC voltage is low and for samples having high moments, the DC voltage is high. Now, after calibrating, the moment of the sample can be measured [118].

The magnetic moment was recorded on an X, Y recorder. The X-input of the X, Y recorder was connected to the output of the Gauss mater, and the Y-input was connected to the recorder output on the front panel. A hysteresis loop of a sample can develop when the magnetic field is swept from zero to positive maximum, then to negative maximum, and then back to positive maximum. The magnetic field was swept from 8,000 Gauss to -8,000 Gauss, and back to 8,000 Gauss over a period of 30 minutes. The magnetic moment of each magnetic sample was measured. The specific magnetic saturation values of the nanofiber composite was calculated for each electrospun sample by dividing the saturation magnetization with its mass [118].

8.8.1 Experiment

Magnetic properties of nanocomposite fibers were characterized by utilizing a vibrating sample magnetometer. A sample of nanocomposite fiber was placed between two coils of an electromagnet that produced a uniform magnetic field gradient. The applied magnetic field induced the magnetic domains to directionally align along the magnetic field. During this induced alignment of the domains, the motion of the ferrite particles produced an electrical signal in a set of pickup coils that was proportional to the magnetic moment, vibration amplitude, and vibration frequency of the ferrite particles. Figure 8-30 shows the superparamagnetic behavior of polyvinylpyrrolidone nanocomposites fibers as a function of the applied field.

At 16 wt% of NiZn ferrites, the magnetic saturation was significantly high, which is because NiZn ferrite particles have high magnetic permeability. NiZn ferrite does not exhibit the cooperative phenonmenon of ferromagnetism found in bulk, since the thermal vibrations are sufficient to reorient the magnetization direction of the magnetic domains [119,121]. As a result, such nanoparticles display superparamagnetic behavior [120,121]. The higher wt% of NiZn

ferrites results in agglomeration of the nanoparticles in the texture of fibers. However, agglomeration of these nanoparticles generally affects the overall magnetization.

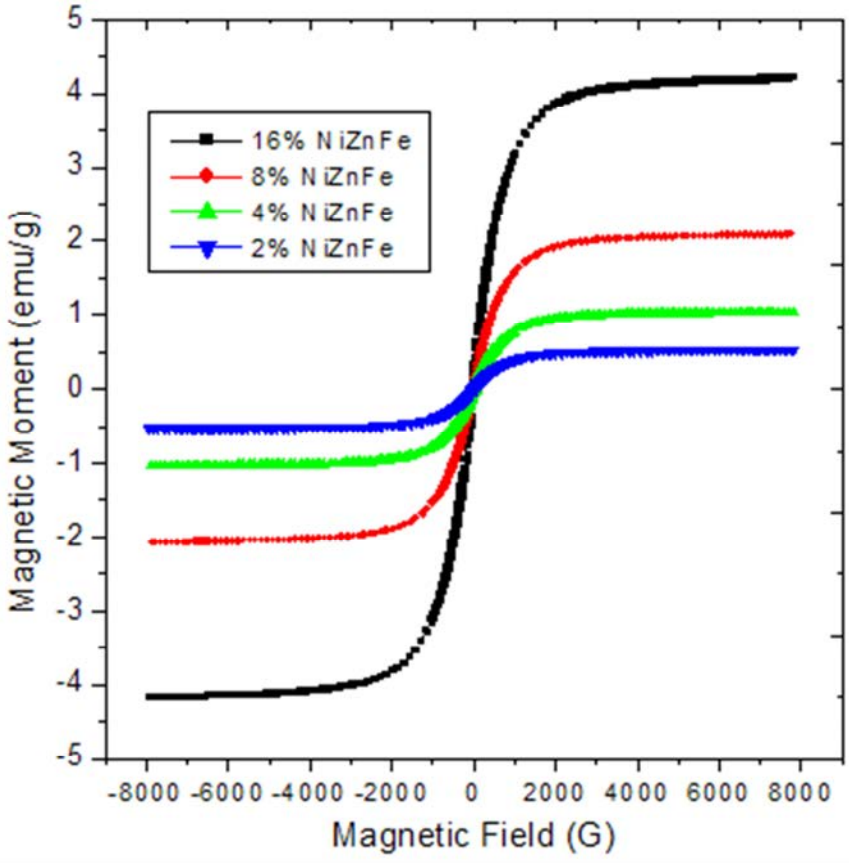

Figure 8-30. Magnetic moment of polyvinylpyrrolidone nanocomposite fiber.

Figure 8-30 shows magnetization curves indicating superparamagnetic behavior of these samples. The magnitude and direction of the applied magnetic field had a direct effect on the magnitude and direction of the induced specific magnetization, which varied according to the applied magnetic field. To better observe any magnetic hysteresis, the region close to the origin in Figure 8-30 should be observed. It can be clearly seen that these flexible samples have very little magnetic hysteresis, with a small residual magnetization at zero magnetic field. As expected, the specific saturation magnetization increased with increasing wt% loading of the nanoparticles [120]. Figure 8-31 shows the superparamagnetic behavior of polyacrylonitrile

nanocomposite fibers as a function of applied field. The NiZn ferrite in nanosacle did not exhibit the ferromagnetism that was found in bulk, since the thermal vibrations werfe sufficient to reorient the magnetization direction of the magnetic domains [119]. As a result, such nanoparticles displayed superparamagnetic behavior [120].

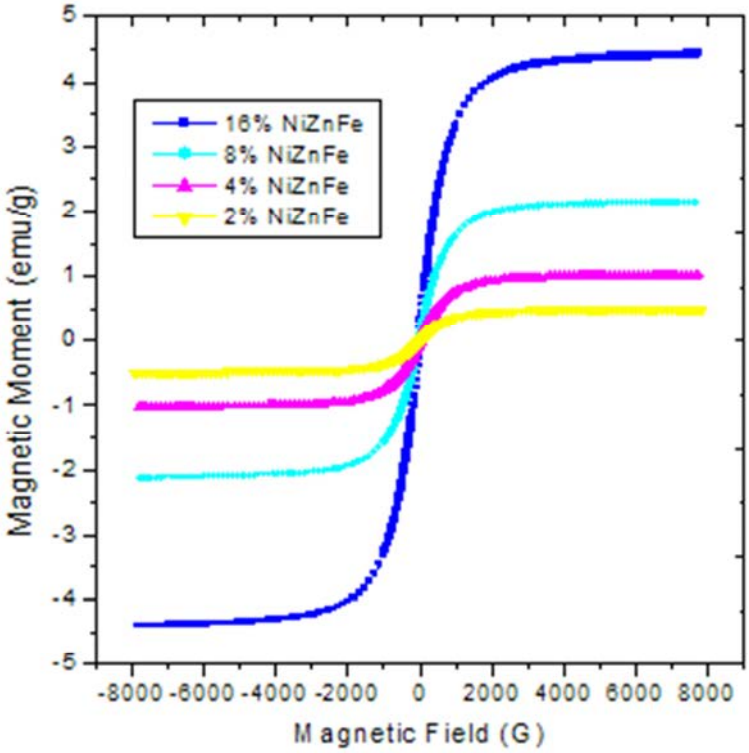

Figure 8-31. Magnetic moment of polyacrylonitrile nanocomposite fiber.

Ferrite nanoparticles become unstable when the particle size is reduced below a certain size, since the surface energy provides a sufficient energy for domains to spontaneously switch polarization directions. As a result, ferromagnetic becomes paramagnetic. However, nanometer-sized ferromagnetics turn into paramagnetics behave differently from the conventional paramagnetic and is referred to as superparamagnetics. In superparamagnetic materials, an interaction of magnetic dipole is also possible. As is known, superparamagnetism is the property of nanosize-noninteracting particles. An agglomeration of nanoparticles leads to magnetically

large particles that are no longer superparamagnetic. For a material to be superparamagnetic, the particles should be isolated. In superparamagnetic materials, coercivity and retentivity rapidly approach zero as the magnetic field is applied and removed. Figure 8-32 shows the magnetic moment of pure NiZn ferrite nanoparticles as a function of the applied field.

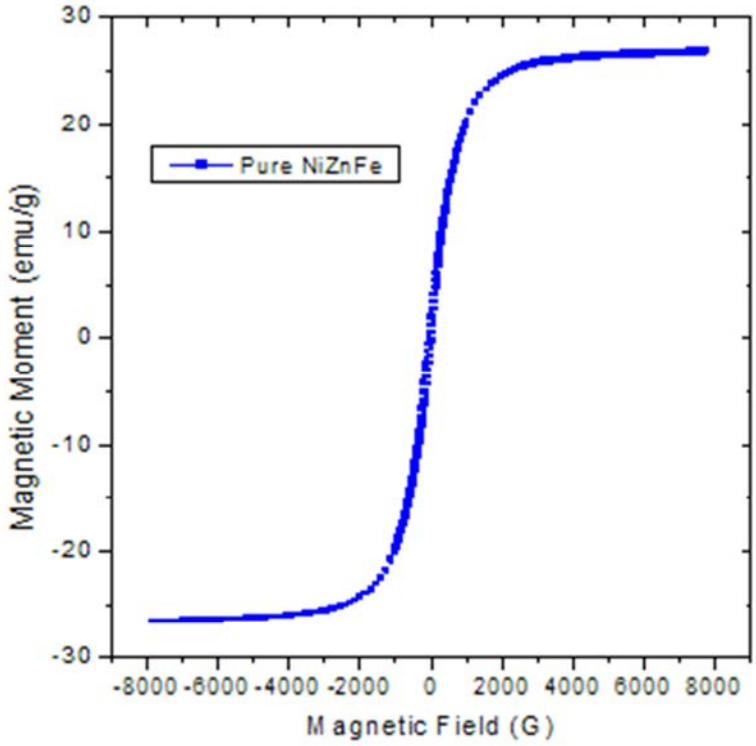

Figure 8-32. Magnetic moment of pure NiZn ferrite nanoparticles.

From the AFM images of NiZn ferrites (Chapter 3), it is clear that the size of the particles is around 21.5 nm. Decreasing the particle size leads to a sudden decrease in coercivity and retentivity to zero, as shown in Figure 8-32. The magnetic properties of nanoparticles are heavily dependent on particle size. Ferromagnetic or ferrimagnetic materials retain orientation of magnetization by their magnetic anisotropy. The most influential effect can be observed when the thermal energy of the particle is higher than the energy of anisotropy, at which point a thermal instability is observed. In superparamagnetic materials, interactions of the magnetic dipole, which are actually nanoparticles, also take place. For a superparamagnetics material, the

nanoparticles should not touch each other or agglomerate. The most common applications of superparamagnetic materials are in medicine, electronic and computer fields, and biology.

8.9 Superconducting Quantum Interface Devices

8.9.1 Experiment

Magnetization measurements were also taken using a superconducting quantum interference device (SQUID). Each sample was first characterized in terms of its temperature dependence of magnetization between 4^0K and 300^0K, with the measuring field (1,000 G) applied prior to cooling (i.e., field-cooled) or after cooling (i.e., zero-field-cooled). Basically, ferrites become ferrimagnetically ordered below a Curie temperature. However, at nanoscale and ideally without interaction among themselves, nanoparticles exhibit a single domain for each particle, and the tendency to align with the applied field is always balanced by the thermal agitation at a given temperature, as in a paramagnet. Consequently, in the case of ZFC, the randomness of particle alignment yields a practically zero magnetization at 4^0K. After a field is applied and the temperature rises, magnetization rises with increasing temperature and reaches the equilibrium value, as revealed by the ZFC curve at a blocking temperature. Such behavior is generally referred to as superparamagnetism.

Another set of experiments at a fixed temperature but changing fields, between +2 and -2 Tesla, determined the saturation magnetization and magnetic hysteresis. In principle, the saturation moments of different samples should be proportional to their ferrite content. Deviations from this would reflect the lack of homogeneity in nanoparticle distribution.

Magnetization of PVP fibers containing different amount of ferrite nanoparticles were obtained using SQUID at 1,000 G (Figure 8-33). The split between ZFC and FC curves for each set corresponds to the blocking temperature (20^0K) of the magnetic nanoparticles.

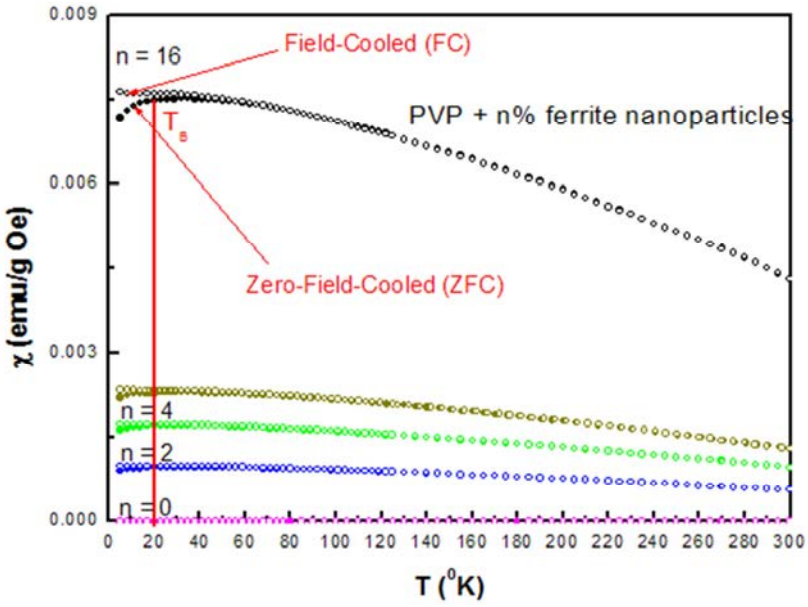

Figure 8-33. Zero-field-cooled and field-cooled magnetization curves for PVP fibers with different wt% of NiZn ferrites.

The 300^0K magnetization of ferrite nanoparticles in PVP fibers approached saturation below 5,000 G (i.e., 0.5 Tesla). No magnetic hysteresis was observed, as can be seen in Figure 8-34. The 5^0K magnetization of ferrite nanoparticles in PVP fibers approached saturation below 5,000 G. Some magnetic hysteresis was observed at this low temperature (Figure 8-35).

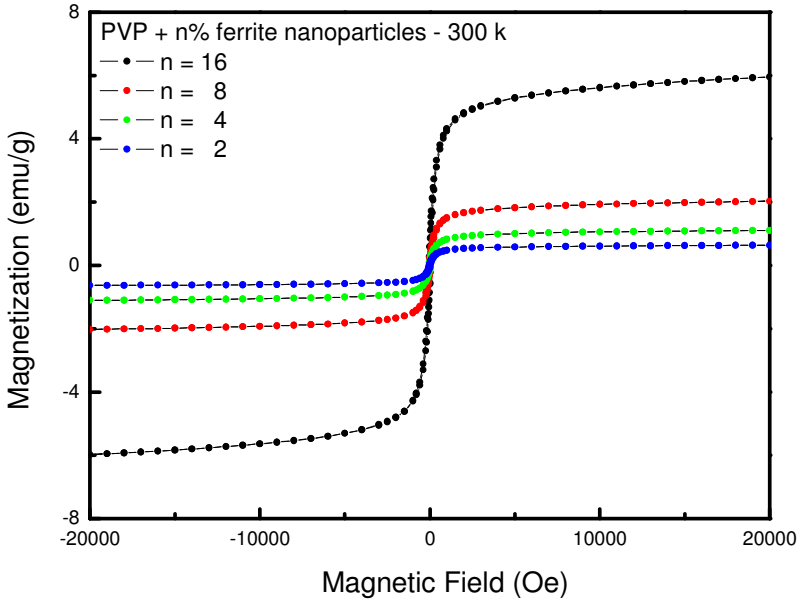

Figure 8-34. Magnetization loop for PVP fibers with different wt% of NiZn ferrite at 300^0K.

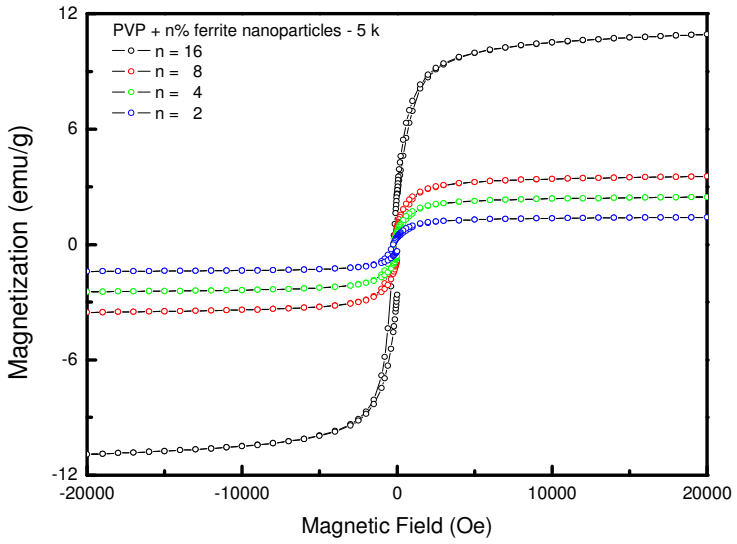

Figure 8-35. Magnetization loop for PVP fibers with different wt% of NiZn ferrite at 5^0K.

Magnetization of PAN containing different amount of ferrite nanoparticles was obtained using SQUID at 1,000 G. The split between ZFC and FC curves for each set corresponds to the blocking temperature (below 50^0K) of the magnetic nanoparticles (Figure 8-36). The 16% sample appears to yield a somewhat lower magnetization than expected, judging from the relative magnitude for other samples. This is likely a consequence of non-homogeneity of nanoparticle distribution.

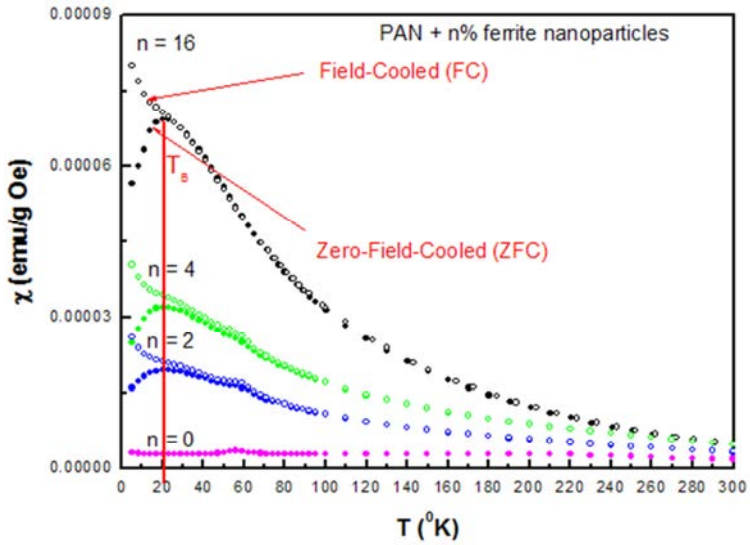

Figure 8-36. Zero –field- cooled (ZFC) and field- cooled (FC) magnetization curve for PAN fibers with different wt% of NiZn-ferrites.

The 300^0K magnetization of ferrite nanoparticles in PAN clearly contains two components (Figure 8-37). A paramagnetic one saturates below 5,000 G (i.e., 0.5 Tesla). Meanwhile, a large diamagnetic effect of PAN fibers, which yields a negative magnetization linear with the field, leads to a rather different overall behavior as compared to that in PVP-based materials. No appreciable magnetic hysteresis was observed. The diamagnetic effect of PAN fibers was less at 5^0K than at 300^0K. An appreciable magnetic hysteresis became visible at this low temperature (Figure 8-38).

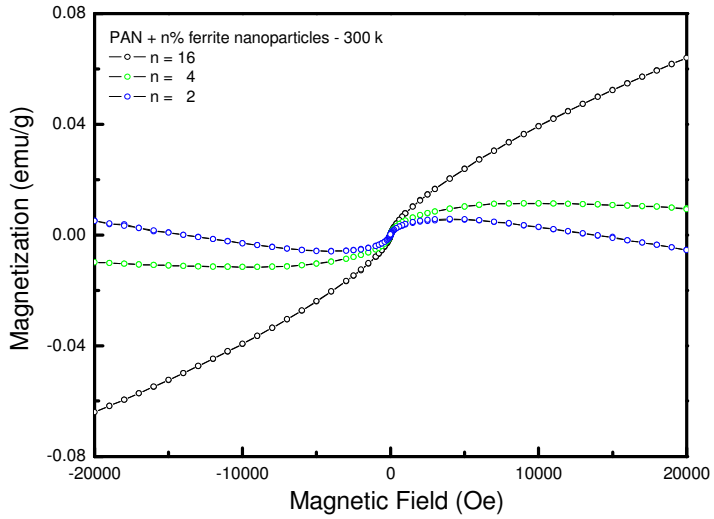

Figure 8-37. Magnetization loop for PAN fibers with different wt% of NiZn ferrite at 300^0K.

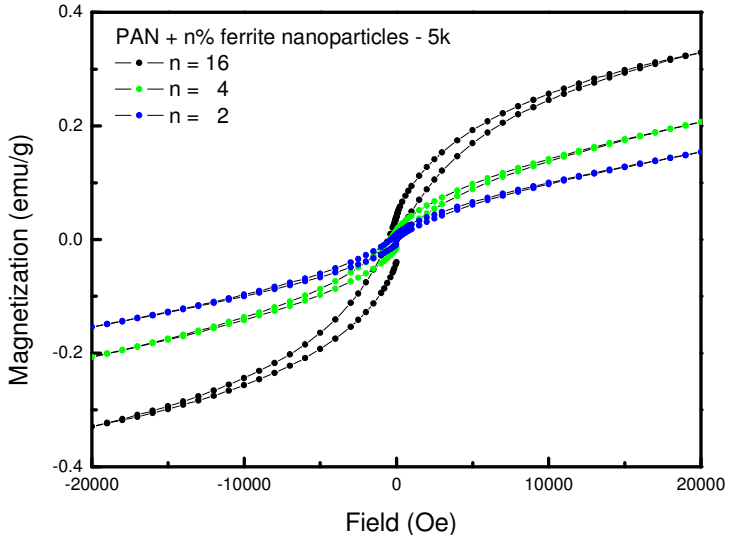

Figure 8-38. Magnetization loop for PAN fibers with different wt% of NiZn ferrite at 5^0K.

As verification of the diamagnetic behavior of PAN-based material is associated with, PAN itself, pure PAN without ferrite inclusions shows a linear dependence of negative magnetization with field (Figure 8-39). The source of the paramagnetism, which appears to saturate below 5,000 G, has yet to be clarified.

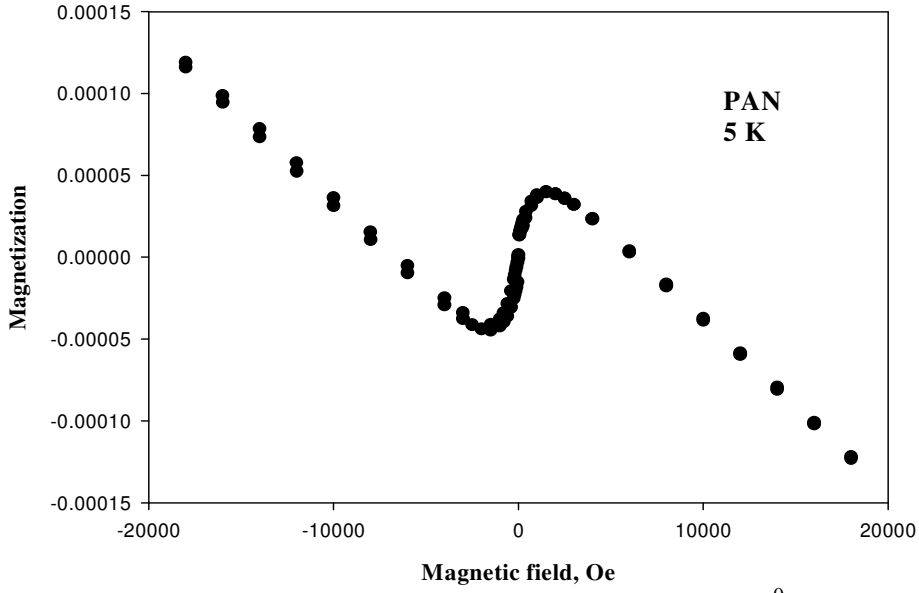

Figure 8-39. Magnetization loop for PAN fibers at 5^0K

8.10 Conclusions

The Mössbauer experiment was performed over the temperature range of 20^0K–300^0K. From the results, it was obvious that the spectrum at 20^0K consists of sextets with broadening lines. It became broadening with increasing temperature, and a central peak was observed at room temperature (300^0K). This behavior is known as superparamagnetic relaxation. In superparamagnetism, the sextet collapses into a singlet or doublet. The temperature above which superparamagnetism appears as a sextet is known as the blocking temperature. Mössbauer spectroscopy revealed a blocking temperature of 20^0K for ferrite nanoparticles containing both PVP and PAN. The same blocking temperature (20^0K) was observed in ZFC and FC curves in ferrite nanoparticles containing PVP and PAN fibers. At 300^0K, SQUID analysis shows that the

magnetization of ferrite containing PVP fibers reached saturation below 5,000 G. A hysteresis loop was not observed, and similarly at 5^0K, no hysteresis loop was observed.

At 300^0K, SQUID analysis showed that the magnetization of ferrite nanoparticles containing PAN fibers consisted of two parts: a paramagnetic part that saturates below 5,000 G and a diamagnetic part. The diamagnetic behavior of ferrite-containing PAN was small at 5^0K, compared to that at 300^0K. Some magnetic hysteresis was obsered at 5^0K in ferrite-containing PAN fibers. In order to study the behavior of PAN fibers, pure PAN fibers were analyzed. These fibers showed a linear dependence of negative magnetization with the field.

In the vibrating sample magnetometer study, no hysteresis loop was observed, either in pure ferrite nanoparticles or in ferrite nanoparticles containing PVP and PAN. As was expected, the saturation magnetization increased as the ferrite content increased.

CHAPTER 9

CONCLUSIONS AND FUTURE WORK

Electrospinning is a process of fabricating microfibers and nanofibers by utilizing an electrostatic field, instead of mechanical and shearing forces, which are used in conventional fiber-forming techniques. Electrospinning utilizes electrical charges that are applied to the polymeric solution to provide a force for stretching the fiber jet until the jet is finally collected on a collector screen. Electrospinning is basically the drawing process of a polymeric solution by electrostatic forces.

9.1 Conclusions

In this research, the electrospinning process and its historical background were discussed extensively, and a comparison was made between conventional fiber-forming techniques and nanofiber-forming techniques. The polymers used in this research were PVP and PAN, and the nano inclusions were MWCNTs and NiZn ferrites. All process and system parameters were discussed, and their effects on fiber diameter were investigated. Atomic force microscopy and scanning electron microscopy were used to determine the surface morphology of electrospun fibers.

The dielectric constants of nanocomposite fibers containing both MWCNTs and NiZn ferrites were determined at room temperature and at high temperature. All factors (temperature, frequency, structure of the polymer, and addition of inclusions) that influence the dielectric constant of the polymer were outlined. It was determined that the dielectric constant increases with the increase in wt% of inclusions, and the dielectric constant of the polymer (PVP and PAN) increases after glass transition temperature.

This research outlined the effects of load and temperature on the resistance of nanocomposite fibers and all factors (porosity, charge-carrier concentration, and polarizability) that influence the resistance of nanocomposite fibers. The addition of MWCNTs and NiZn ferrites decreased the resistance due to charge-carrier concentration and polarizability. In the temperature vs resistance study of PVP fibers, a phase transition in the temperature range 40^0K–56^0K was observed, and this phase transition was confirmed by differential scanning calorimetry.

This research also included the thermal characterization of nanocomposite fibers using a comparative method. In PAN fibers, thermal conductivity increased with the increase in wt% of MWCNTs, but no significant increase in thermal conductivity was observed in NiZn ferrite-based PAN fibers. This could be attributed to the semi-conducting behavior of NiZn ferrites and non-conducting behavior of PAN. In PVP fibers, thermal conductivity increases with the increase in wt% of MWCNTs and NiZn ferrites.

Electrospun fibers can be used as an alternative material for sound absorption in aircraft interiors. Electrospun fibers have numerious advantages such as porosity, high surface area, and high aspect ratio. In this research, electrospun fibers were proposed as sound-absorption material in aircraft interiors. It was determined that polyvinylpyrrolidone plus polyvinylchloride, and polystyrene plus polyvinylpyrrolidone can be used in combination for sound absorption. These materials have a sound-absorption coefficient of around 0.9 to 1 at high frequency (6,000 Hz).

This research highlighted the magnetic properties of NiZn ferrite-based nanocomposite fibers. Mössbauer spectroscopy revealed a blocking temperature of 20^0K for ferrite nanoparticles containing both PVP and PAN, and the same blocking temperature was confirmed by SQUID analysis. Mössbauer spectroscopy, SQUID, and vibrating sample magnetometer analysis revealed that ferrite nanoparticles containing both PVP and PAN are superparamagnetic.

9.2 Future Work

9.2.1 Superhydrophobic Behavior of Electrospun Micro- and Nanofibers

Hydrophobicity refers to the physical property of a surface on which hydrophobe molecules repel water molecules, causing higher water contact angles, θ, (over 90^0). In other words, water adsorption on the surface is thermodynamically impossible. Hydrophobic (hydro – water, phobic – fearing) molecules can be non-polar natural and synthetic materials, such as alkenes, oils, fats, and greasy substances. However, hydrophilicity is exactly the opposite of hydrophobicity, where a polar hydrophilic surface interacts with water molecules through hydrogen bonds and creates lower water contact angles (lower 90^0). Some materials can show both hydrophobic and hydrophilic parts on the surface. For example, soap is a surfactant that has a hydrophobic tail and hydrophilic head groups, which allows it to dissolve in both water and oil depending on the orientations of the molecules.

Superhydrophobicity is a physical property of a surface where a water contact angle exceeds 150^0. A water droplet can bounce on the superhydrophobic surface and also roll off with less than 10^0 contact angle. Because of the surface roughness and hydrophobicity of the solid surfaces, a superhydrophobic surface has an extremely high water-repellent behavior, is very difficult to wet, and is also called a elf-cleaning surface. Thus, bacteria, fungi, algae, and other parasites and microorganisms cannot grow on top of the superhydrophobic surfaces. Superhydrophobic properties of the polymeric fibers should improve significantly by changing the roughness, fiber size, shape, and surface hydrophobicity of the polymers.

Superhydrophilicity is the opposite of superhydrophobicity, in which water contact angle become less than 5^0 in 0.5 seconds or less. Superhydrophilic materials have several advantages, such as antifogging, antibacterial, and wettable surfaces. In future studies, the surface

hydrophobic behavior of electrospun micro- and nanofibers will be determined with and without nano inclusions such as carbon nanotubes and graphene. Electrospun superhydrophobic fibers can have various industrial applications, such as non-wettable fabric, antibacterial surface, low friction devices, micro-electro-mechanical systems, nano-electro-mechanical systems, microfluidics, and nanofluidics.

9.2.2 Vacuum-Assisted Resin Transfer Molding (VARTM) Using Electrospun Fibers for Composite Fabrication

Fibers are materials that have one very long axis compared to other. The other axes are often circular or near circular. These fibers have significantly more strength in the long direction than in the other directions. Most materials are stronger and stiffer in the fibrous form than in any other form. Thus, fibers are most commonly used for reinforcement in a softer matrix. Fibers usually have high stiffness and relatively low density. Some of the most common fibers currently used in composite materials include the following:

- Glass
- Boron
- Carbon
- Aramid
- Ceramic
- Metallic

Glass is by far the most widely used fiber, because of the combination of its low cost, corrosion resistance, and in many cases efficient manufacturing potential. It has relatively low stiffness, high elongation, and moderate strength and weight. It is used in applications where corrosion resistance is important, such as piping. Boron fibers offer very high stiffness, but are

also very costly. They have relatively high diameter, typically on the order of 200 microns, a high stiffness-to-weight ratio, and good comprehensive strength.

Carbon fibers are widely used in the aerospace industry and some applications of sporting goods, taking advantage of the relatively high stiffness-to-weight and high strength-to-weight ratios of these fibers. The high stiffness and strength combined with low density and intermediate costs have made carbon fiber second only to glasss fibers in use. Aramid fibers offer higher strength and stiffness relative to glass fiber coupled with lightweight, high-tensile strength but lower compressive strength. Ceramic fibers consist of metal oxides, which are used in high temperature applications. This class of fibers includes beryllia, magnesia, and alumina. Their main advantage is high modulus and strength. A manufactured fiber composed of metal-coated plastic, plastic-coated metal, or metal. Metallic fibers are generally used for decorative purposes.

Electrospun micro- and nanofibers can be recommended as potential candidates in composite fabrication in place of traditional fibers such as glass, carbon, aramid, and boron. Electrospun fibers have excellent corrosion resistance and high tensile strength, and are low in cost and lightweight. The fabrication of fibers via electrospinning is relatively easy and cheaper than conventional-fiber fabrication.

9.2.3 Acoustical Properties of Electrospun Carbon Nanotube-Based Nanocomposite Fiber

Electrospun nanofibers encapsulated with carbon nanotubes are appealing candidates for sound absorption in aircraft interiors instead of conventional materials such as foam, cavities, viscoelastic, solid, and liquid structures. Electrospun nanofibers have many advantages, such as high porosity, high surface area, and high aspect ratio. The production process via

electrospinning is relativey easy and inexpensive. The weight of the electrospun fibers is much less than that of conventional materials.

The sound absorption mechanism depends upon certain parameters such as size of pores, orientation of pores, and number of pores. The mechanism for absorption of sound energy in porous materials depends upon the fluid friction and energy dissipation between air and fiber surface. Air molecules oscillate in the interstices of porous materials with the frequency of existing sound. If carbon nanotubes are encapsulated in nanocomposite fibers, the nanofibers will act as springs. The fluid friction and energy dissipation will increase and therefore, sound absorption coefficient will increase.

LIST OF REFERENCES

REFERENCES

[1] G. Taylor, "Electrically driven jets," *Proc. R. Soc. London A*, vol. 313, 1969, pp. 453-475.

[2] Bharat Kumar Raghavan, *Forming of Integarted Webs of Nanofibers via Electrospinning*, Ph.D. dissertation, Dept. of Paper and Chemical Engineering, Miami University, Oxford, Ohio, 2006.

[3] Zheng-Ming Huang, Y. Z. Zhang, M. Kotaki, and S. Ramakrishna, "A view on polymer nanofibers by electrospinning and their applications in nanocomposite," *Composite Science and Technology*, vol. 63, no. 15, 2003, pp. 2223-2253.

[4] H.Fong, I.Chun and D.H.Reneker, "Beaded nanofibers formed during electrospinning," *Polymer*, vol. 40, 1999, pp. 4585-4592.

[5] J.H. He, Y.Q. Wan, and Jy Yu, "Application of vibrating technology to polymer electrospinning," *International Journal of Nonlinear Sciences and Numerical Simulation*, vol. 5, no. 3, 2004, pp. 253-262.

[6] Yuris A. Dzenis, "Electrospinning of polymer nanofibers: a review of recent accomplishments in process Analysis," *Proc. International Conference on Applied Mechanics,* Durban, South Africa, January 11-13, 2000, pp. 18-23.

[7] Leslie Y.Yeo and James R.Fried, "Electrospinning carbon nanotubes polymer composite nanofibers," *Journal of Experimental Nanoscience*, vol.1, June 2006, pp. 177–209.

[8] Veli E. Kalayci and Prabir K. Patra, "Fundamental investigations on electrospun fibers," *Journal of Advanced Materials*. vol. 36, no. 4, Oct. 2004, pp. 43-47.

[9] Woraphon Kataphinan, *Electrospinning and Potential Applications*, Ph.D. dissertation, Dept. of Polymer Science, University of Akron, Akron, OH, 2004.

[10] A.L.Yarin, S. Koombhongse and D.H. Reneker, "Bending instability in electrospinning of nanofibers*," J. Appl. Physic*. vol. 89, no. 5, March 2001, pp. 3018-3026.

[11] Seeram Ramakrishna, *An Introduction to Electrospinning and Nanofibrs*, World Scientific Publishing, 2005, pp. 307-309.

[12] W.Simm, "Fiber fleece of electrostatically spun fibers and method of making same," U.S. Patent No. 4143196, 1979.

[13] Seungsin Lee and S. Kay Obendorf, "Use of electrospun webs for protective textile materials as barriers to liquid penetration," *Textile Research Journal*, vol. 77, 2007, pp. 699-702.

REFERENCES (Continued)

[14] Mung-Seob Khil and Dong-II Cha, "Electrospun nanofibrous polyurethane membrance as wound dressing," *Journal of Biomedical*, vol. 67B, no. 2, 2003, pp. 675-679.

[15] Jyh-Ping Chen and Go-Yun Chang, "Electrospun Collagen/Chitosan nanofibrous membrance as wound dressing," *Nanoscience and Nanotechnology*, vol. 313-314, 2008, pp. 183188

[16] Zuwei Ma, Masaya Kotaki and Tomas Yang, "Surface engineering of electrospun polyethylene terephthalate (PET) nanofibers towards development of a new material for blood vessel engineering," *Nanoscience and Nanotehnology*, vol. 2, no. 2, 2005, pp 2527-2536.

[17] Levy, "Segmented polyurethane surgical buttressing pledgets," U.S Patent No. 5, 549,545, Oct. 1985.

[18] David Ziegler, Kris J Senecal and Chris Drew, "Electrospun fibrous membranes of photovoltaic and conductive polymers," *The Fiber Society: Nonwoven Cooperative Research Center: Book of Abstracts,* Lowell, USA, 2001. http://www.tx.ncsu.edu/jtatm/volume1specialissue/posters/posters_part1.pdf [accessed in April 2010]

[19] Ko, F.K. Laurencin, C.T. Borden.M.D,Attawia, M.D. and Renekar, D.H.,"The dynamic of cell- Fiber Architecture Interaction, Transaction of the Society for Biomaterials,"*The proceeding of 24th Annual Meeting of the society for biomaterials,* vol. XXI, San Diego, C.A.,USA, April 22-26, 1998.

[20] L. Roy Xu and Lang Li., "Mechanical characterization of nanofiber-reinforced composite Adhesives," *Journal of nanoscience and technology*, vol 7, 2007, pp. 2546-2548.

[21] Jong-Sang Kim and D.H.Keneker, "Polybenzimidazole nanofiber produced by electrospinning," *polymer Engg. and Science*, vol. 39, no. 5, May 1999, pp. 849-854.

[22] Peter Jared Goldstein., *Electrospinning of Ceramic and Nanocomposite Nanofibers*, Master's thesis, University of Florida, 2004.

[23] Dong II Cha, Hak Yang Kim, Keun Hyung Lee and Yang Chae Jung, "Electrospun nonwovens of shape-memory polyurethane block copolymer," *Journal of Applied Science*, vol. 96, no. 2, April 2005, pp. 460-465.

[24] www.eng.nus.edu.sg/EResnews/9702/feb97p10.html [accessed in April 10, 2010]

REFERENCES (Continued)

[25] Keyur Desai, *Electrospinning and Phase Characterization of Polyaniline/poly Methylmethacrylate Blends,* Master's thesis, University of Massachusetts lowell, 2000.

[26] www.weizmann.ac.il/.../Lyotropics/lcp.html [accessed in April 10, 2010]

[27] www.polymerprocessing.com/.../dspin/dfig1.gif [accessed in April 10, 2010]

[28] www.precisionliftinc.com/polyrope.shtml [accessed in April 10, 2010]

[29] Bharath Kumar Raghavan, *Forming of Integral Webs of Nanofibers via Electrospinnning,* Master's thesis, Miami University, Oxford, 2006.

[30] P. Heikkilä and A. Harlin, "Electrospinning of polyacrylonitrile (PAN) solution: Effect of conductive additive and filler on the process," *eXPRESS polymer Letters*, vol. 3, no. 7, 2009, pp. 437-445.

[31] Lord Rayleigh, "Equilibrium of liquid conducting masses charged with electricity,"*London Edinburgh and Dublin Phil. Mag. Journal*, vol 44, 1982, pp. 184-186.

[32] Liu Yingjun, *Morphology Dependence of Hybrid Nnaofibers Incooprporated with Nanoparticles on Electrspinning and Post-Conditions*, Dept. of Mechanical Engineering, National University of Singapore, 2008.

[33] G. Taylor, "Disintegration of water drops in an electric field," *Proc. R. Soc. London A*, vol. 280, 1964, p. 383.

[34] G. Taylor, "The force exerted by an electrical field on a long cylindrical onductor," *Proc. R. Soc. London A*, vol. 291, 1965, pp. 145-158.

[35] A. Formhals, "Artifical thread and method of producing same," U.S Patent No. 2, 187, 306, Serial No. 156,167, July 1937.

[36] J. P. Bery, "Method and apparatus for manufacturing electrostatically spun structure," U.S Patent No. 5, 024, 780, Jun 18, 1991.

[37] A. Formhals, "Method and apparatus for the production of fibers," U.S Patent No. 2, 123, 991, Serial No. 88,431, July 1938.

REFERENCES (Continued)

[38] Baumgarten, P.K., "Electrostatic spinning of acrylic micro fibers," *Journal of colloid and interface Science*, vol. 36, May 1971, pp. 71-79.

[39] Thandavamoorthy Subbiah, G S Bhat and R W Tock, "Electrospinning of nanofibers," *journal of applied polymer science*, vol. 96, no. 2, 2005, pp. 557-569.

[40] Doshi J N, *The electrospinning Process and Application of Electrospun Fibers,* Ph.D. dissertation, Dept. of Polymer Science, University of Akron, Akron, OH, 1994.

[41] J. Doshi and D. H. Renekar, "Electrospinning process and applications of electrospun fibers," *J. Electrost*. vol. 35, no. 2 and 3, 1995, pp. 151-160.

[42] Srinivasan, G, *Structure and Morphology of Electrospun Polymer Fibers,* Ph.D. dissertation, Dept. of Polymer Science, University of Akron, Akron, OH, 1994.

[43] Srinivasan, and G., Renekar, D.H., "Structure and morphology of small diameter electrospun aramid fibers," *Polym.Int*. 1995, pp. 195-201.

[44] Chun I, *Effect of Molecular Characteristic on Strength of Elastomer*, Ph.D. dissertation, Dept. of Polymer Science,University of Akron, Akron, OH, 1997.

[45] H. Fong, I. Chun and D. H. Reneker, "Beaded nanofibers formed during electrospinning," *Polymer*, vol. 40, no. 16, 1999, pp. 4585-4592.

[46] R. Jaeger, M. M. Bergshoef, M. Ibatlle, H. Schönherr and G. J. Vanso, "Electrospinning of ultra-thin polymer fibers," *Macromolecular Symposia*, vol 127, 1997, pp. 141-150.

[47] G. J. Vanso, H. Schönherr and D. Snetivy, *Morphology, Chain Packing and Conformation in Uniaxially Oriented Polymers Studied by Scanning Force Microscopy*, American Chemical Society, 1998, pp. 67-93.

[48] Fong X, *The Study of Electrospinning and Physical Properties of Electrospun Nanofibers,* Ph.D. dissertation, Dept. of Polymer Science, University of Akron, Akron, OH, 1999.

[49] H.Fong, Weidang Liu, Chyi-Shan and Richard A. Vaia, "Generation of electrospunfibers of nylon 6 and nylon 6-montmorillonite nanocomposite," *Polymer*, vol. 43, no. 3, 2002, pp. 775-780.

[50] Stenoien et al. "Method of making a silicone composite vascular graft," US Patent. No. 5, 840, 240, Nov. 24, 1998.

[51] Zarkoob S, *Structure and Morphology of Regenerated Silk Nanofibers Produced by Electrospinning*, Ph.D. disertation, Dept. of Polymer Science, University of Akron, 1998.

REFERENCES (Continued)

[52] S. Zarkoob, R. K. Eby, D. H. Reneker, S. D. Hudson, D. Ertley and W. W. Adams, "Structure and morphology of electrospun silk nanofibers," *Polymer*, vol. 45, no. 11, 2004, pp. 3973-3977.

[53] Lei Huang, R. Andrew, McMillan, R. P. Apkarain, B. Pourdeyhimi, Vincent P. Conticello and E. L. Chaikof, "Generation of synthetic elastin-mimetic small diameter fibers and fiber network," *Macromolecules*, vol. 33, no. 8, 2000, pp. 2989-2997.

[54] N. J. Pinto, "Electrospun polyaniline/polyethylene oxide nanofiber field-effect transistor,"*Applied Physics Letters*, vol. 83, no. 20, 2003, pp. 4244-4246.

[55] I. D. Norris, M. M. Shaker, F. K. Ko and A. G. MacMiarmid, "Electrostatic fabrication of ultrafine conducting fibers: polyaniline/polyethylene oxide blends," *Synthetic Metals*, vol. 114, no.2, 2000, pp. 109-114.

[56] Daoheng Sun, Chieh Chang, Sha Li and Liwei Lin, "Near-field electrospinning," *Nano. Letters*, vol. 6, no. 4, 2006, pp. 839-842.

[57] Bognitzki, M., Frese, T., Wendorff, J.H. and Grenier, A., Book of Abstract, *219th ACS National Meeting,* San Francisco, CA, March 26-30, 2000, *PMSE-173*. Publisher, American Chemical Society, Wasington, D.C.

[58] Zaicheng Sun, Eyal Zussman, Alexander L. Yarin, J. H. Wedroff and A. Greiner, "Compound core-shell polymer nanofibers by co-electrospinning,"*Advanced Materials*, vol 15, no. 22, 2003, pp. 1929-1932.

[59] C. Drew, X. Wang, K. Senecal, Schreuder-Gibson, H., He, J., Tripathy and S., Samuelson, L.*, Proceeding of Annu. Tech. Conference. – Soc.Plast. Eng*., 2000, 58th, vol. 2, pp. 1477-1481.

[60] Anil Suthar and George Chase, "Nanofibers in filter media," *Chemical Engineer*, no. 726, 2001, pp. 26-28.

[61] Wessling B, "Dispersion as the link between basic research and commercial application of conducting polymer (polyaniline)," *Synthetic Metals*, vol. 9, 1998, pp. 143-154.

[62] Kataphinan W, Dabney S, D.H. Reneker, Smith D and Akron Uo, "Electrospun Skin masks and uses thereof," Patent WO0126610. University of Akron, 2001.

[63] P. Gibson, A. McManus, C. Meel et al. "Electrospun fibers and apparatus thereof," Patent WO0127365. University of Akron, 2001.

REFERENCES (Continued)

[64] C. Li, H. Jin, G. D. Botsaris, D. L. Kaplan, *Abstract of papers, 226th ACS National Meeting*, *PMSE- 257*, *American Chemical* Society, New York, USA, 2003.

[65] Darrell H.Renekar, "Bending instability of electrically charged liquid jets of polymer Solutions in electrospinning," *Journal of applied physic*, vol. 87, no. 9, 2000, pp. 4531-4546.

[66] Chen-Ming Hsu, *Electrospinning of poly (ε-Caprolactone),* Master's Thesis, Worcester Polytechnic Institute, 2003.

[67] Y. M. Shin, M. M. Hohman, M. P. Brenner and G. C. Rutledge, "Electrospinning: A whipping fluid jet generates submicron polymer fibers," *Applied Physics Letters*, vol. 78, no. 8, Feb. 2001, pp. 1149-1151.

[68] G. C. Rutledge and Sergey V. Fridrikh, "Formation of fibers by electrospinning," *Advanced Drug Delivery Reviews*, vol. 59, no. 14, Dec. 2007, pp. 1384-1391.

[69] Y. M. Shin, M. M. Hohman, M. P. Brenner and G. C. Rutledge, "Experimental characterization of electrospinning: the electrically forced jet and instabilities," *Polymer*, vol. 42, no. 25, Dec. 2001, pp. 09955-09967.

[70] A. F. Spivak, Y. A. Dzenis and D. H. Reneker, "A model of steady state jet in electrospinning process," *pregamon: Mechanical Research Communication*, vol 27, no. 1, 2000, pp. 37-42.

[71] A. F. Spivak and Y. A. Dzenis, "Asymptotic decay of radius of a weakly conductive viscous jet in an external electric field," *Applied Physic Letters*, vol 73, no. 21, Nov. 1998, pp. 3067-3069.

[72] Yarin, A.L.S.Koombhongse and D.H.Renekar, Taylor cone and jetting form liquid droplets in electrospinning of nanofibers, *journal of applied physic*, vol. 90, no. 9, 2001, pp. 4836- 4846.

[73] Sergey V.Fridrikh, Jian H.Yu, Michael P.Brenner and Gregory C.Rultedge, "Controlling the Fiber diameter during Electrospinning," *Physic review Leters*, vol. 13, no. 14, April 2003, pp. 144502(1)-144502(4).

[74] J.J. Feng, "The stretching of an electrified non-Newtonian jet: A model for electrospinning," *Physic of Fluids*, vol. 14, no. 11, Nov. 2002, pp. 3912-3926.

[75] Sphurti Bharagava, *Submicron size Structures, Electrospinning and Filters*, ph.D dissertation, Dept. of Polymer Science, University of Akron, Akron, Ohio, May 2007.

REFERENCES (Continued)

[76] J.M.Deitzel, J.Kleinmeyer, D.Harris and N.C.Beck Tan, "The effect of processing variables on the morphology of electrospun nanofibers and textiles," *Polymer*, vol. 42, no. 1, 2001, pp. 261-272.

[77] J.M.Deitzel, J.D.Kleinmeyer, J.K.Hirvonen, N.C.Beck, "Controlled deposition of electrospun poly (ethylene oxide) fibers," *polymer*, vol. 42, 2001, pp. 8163-8170.

[78] Waseem khan, M. Ceylan, and R. Asmatulu, "Dielectric properties of MWCNTs reinforced polyacrylonitrile (PAN) nanofibers at varying temperatures,"*Proceeding of 5th annual symposium on graduate research and scholary project*, Wichita State University, KS, USA, 2009.

[79] Noral E. Hill, Worth E. Vaughan, A.H.Price and Mansel Davies, *Dielectric Properties and Molecular Behavior,* Van Nostrand Reinhold, 1st edition, 1969, pp. 1-4.

[80] Tony Blythe and David Bloor, *Electrical Properties of Polymers*, 2nd edition, Cambridge, 2005, pp. 28-29.

[81] M. Ali Omar, *Elementary Solid-State Physics*, 2nd edition, Addison- Wesley, 1993, p. 415.

[82] Zhiping Jiang, Ming Li, and X.-C. Zhang, "Dielectric constant measurement of thin films by differential time-domain spectroscopy," *Appl. Phys. Lett*., vol. 76**,** 2000, pp. 3221-3223.

[83] D.V.Blackham and R.D.Pollard, "An improved Technique for Permittivity measurement using coaxial probe," *IEEE Trans. Meas*., vol. 46, no. 5, Oct 1997, pp. 1093-1099.

[84] Waseem khan, R. Asmatulu, M. M. Eltabey, "Dielectric properties of electrospun PVP and PAN nanocomposite fibers at various temperatures," *ASME*, vol.1, Nov.2010.

[85] Charles Phelps Smyth, "Dielectric Behaivors and Structure," *Journal of Electrochem.Soc*, vol. 103, no. 10, 1956, p. 232C.

[86] http://www.chemguide.co.uk/physical/basicrates/arrhenius.html [accessed in April 2010]

[87] James E. Mark and Adi Eisenberg "*Physical Properties of Polymers,"* United Book Press, 2nd edition, 1993. p. 67.

[88] John J. O'Dwyer, *The theory of electrical conduction and breakdown in solid dielectrics,* Clarendon Press (Oxford), 1973, pp. 1-6.

REFERENCES (Continued)

[89] Waseem Khan, R. Asmatulu, M. M. Eltabey, M. M. Ho and H. Hamdeh, "Electrical Properties of nanocomposite fibers under various loads and temperatires," *Proceedings of the ASME 2009 , International Mechanical Engineering Congress & Exposition, IMECE2009*, Lake Buena Vista, Florida, USA, November 13-19, 2009.

[90] Allen Miller and Elithu Abrahams, "Impurity Conduction at low Concentration," *Phys. Rev.*, vol. 1120, 1960, pp. 745-755

[91] R.Bartnikas and R.H.Eichhom, *Engineering Dielectric*, ASTM, 1983, pp. 239-339.

[92] Andrew K.Galwey and Michael E.Brown, "Application of the Arrhenius equation to solid state kinetics: can this be justified?, *Thermochimica Acta Mat. Scie**nce,*** vol. 386, no. 1 2002, pp. 91-98.

[93] R. Asmatulu, W Khan and M. B. Yildirim, "CNT reinforced nanocomposite fiber fabrication for undergraduate students," *2008 ASEE Midwest Regional Conference*, September 18-19, Tulsa, OK, USA, 2008, pp. 1-7.

[94] Asmatulu R, Khan. W, Nguyen K.D, and Yildirim M.B, "Synthesizing Magnetic Nanocomposite Fibers for Undergraduate Nanotechnology Education," *International Journal of Mechanical Engineering Education*, 2008. http://www.asee.org/documents/sections/midwest/2007/ASEEMIDWESTSECTION2007_0018_8f50d3b62a83c8118932ab4a0a97d62d.pdf [accessed in Nov. 2010]

[95] F F Hatta, MZA Yahya, AMM Ali and RHY Subban, "Electrical Conductivity Studies on PVA/PVP-KOH Alkaline Solid Polymer Blend Electrolyte," *Ionics*, vol. 11, no. 5-6, 2005, pp. 418-422,

[96] Abraham Nitzan and Mark A. Ratner, "Conduction in polymers: Dynamic disorder Transport," *J. Phys. Chem.*, vol. 98, no. 7, 1994, pp. 1765–1775.

[97] P. Bahadur and N. V. Sastry, *Principles of Polymer Science*, 2nd ed., Alpha Science, 2005, pp. 97-102.

[98] D. W. Van Krevelen, *Properties of Polymers*, 3rd ed. Elsevier Science Pub Co, Dec. 1, 1990, pp. 129-150.

[99] M. Moss, J. A. Koski, and G. M. Haseman, "Measurement of thermal conductivity by Comparative technique," Sandia National Labs., Albuquerque, NM, USA, Report No. Sand 82-0109, March 01, 1982.

REFERENCES (Continued)

[100] J. N. Sweet, E. P. Roth, M. Moss, G. M. Haseman, and A. J. Anaya, "Comparative thermal conductivity measurement at sandia national laboratories," Sandia National Labs., Albuquerque, NM, USA, Report No.SAND 86-0840, 1986.

[101] Philip. E .Slade, Jr., Lioyd T. and Jenkis, *Thermal Characterization Techniques*, New York, Publisher, Marcel Dekker, vol. 2, 1970, pp. 247-289.

[102] Tony Blythe and David Bloor, Electrical *Properties of Polymers,* Cambridge university press, New York, 2005, pp. 22-24

[103] M. J. Biercuka, M.C. Llaguno, M. Radosavljevicb, J. K. Hyunc, and A. T. Johnsond, "Carbon nanotube composites for thermal management,"*Appplied Physic Letters*, vol. 80, 2002, p. 2767.

[104] R. Asmatulu, S.Davluri and W. Khan , "Fabrication of CNT based nanocomposite fibers from the recycled plastic"*, Proceedings of the ASME 2009 International Mechanical Engineering Congress & Exposition, IMECE2009*, November 13-19, Lake Buena Vista, Florida, USA.

[105] Edith A. Turi, *Thermal Characterization of polymer materials*, Academic Press 1997, pp. 845-906.

[106] Barber, *A Handbook of Noise and Vibration Control, seventh edition,* Elsevier, 2002.

[107] J. E. Locke, S. Sharma and C. Chan, "Construction of a database for the acoustical characteristics of fibers and foams used for aircraft interior noise treatment,"*NIS Report to National Institute for Aviation Research (NIAR),* Wichita State University, 2007.

[108] I. Dandaroy, D. Hartley and R. Hund, "Interior noise perdition of hawker horizon aircraft using statistical energy analysis," *Noise-Con*, Baltimore, Maryland, July 12-14, 2004, pp. 333- 342.

[109] J. Hileman, Z. S. Spakovszky, H. Drela and M. Sargeant, "Airframe design for silent aircraft," *AIAA Journal*, 2007, p. 453.

[110] A.Manneville, D. Pilczer, and Z. Spakovszky, "Preliminary evaluation of noise reduction approaches for a functionally silent aircraft", *AIAA Journal*, vol. 43, no. 3, 2006, pp. 836-840.

[111] Malcolm J. Crocker, *Handbook of acoustics*, Wiley & Sons, 1997, pp. 769-797.

REFERENCES (Continued)

[112] Westre, W.N., and Evans, D.W, "Integrated aircraft structural floor," U.S. Patent No. 7182291, Feb. 27, 2007.

[113] A. Wobben, "Reduction in the noise produced by a rotor blade of a wind turbine," U.S. Patent No.20060115362, June 1, 2006.

[114] J. J. Finnerman, "Active impedance control within a cylindrical waveguide for generation of low-frequency, underwater plane traveling waves,"Standard Designation E 1050-90, Standard Test Method for Impedance and Absorption of Acoustical Materials Using a Tube, Two Microphones, and a Digital Frequency Analysis System, *ASTM.* 1990.

[115] Waseem S Khan, "Fabrication and characterization of polyvinylpyrrolidone and polyacrylonitrile elctrospun nanocomposite fibers,"Ph.D dissertaion, Dept. of Mechanical Engineering, Wichita State University, Dec. 2010.

[116] Mehmet Tuncer Unver, *A Mosbauer Spectroscopy Study of Pr-Fe-B Nanocompsites,* Master's thesis, Dept. of Physic, Wichita State University, 2003.

[117] Yen-Min Churn, *Mossbauer Studies of Cobalt Ferrite Nanoparticles Synthesized by Hydrolysis*, Master's thesis, Dept. of Physic, Wichita State University, 2004.

[118] Saman M. Dharmatilleke, *Vibrating Sample Magnetometer: Installation, Calibration and Measurement*, Master's Thesis, Dept. of Physic, Wichita State University, 1997.

[119] M. Wang, H. Singh, T. A. Hatton and Rutledge, "Field-responsive superparamagnetic composite nanofibers by electrospinning," *Polymer*, vol.45, 21 July 2004, pp. 5505-5514.

[120] Pankaj Gupta, *Processing Structure Property Studies of 1) Submicron Polymeric Fibers Produced by Electrospinning and II) Films of Linear Low Density Polyethylene as Influenced by Short Chain Branch Length in Copolymer of Ethylene / I-Butene, Ethylene / I-Hexene and Ethylene / I-Octene Synthesized by a Single Site Metallocene Catalyst*, Ph.D dissertation, Virginia polytechnic Institute, 2004.

[121] Pankaj Gupta, Ramazan Asmatulu, Rick Claus, Garth Wilkes, "Superparamagnetic Flexible Substrates Based on Submicron Electrospun Estane® Fibers Containing MnZnFe–Ni Nanoparticles," Published online in *Wiley InterScience*, 2005.

[122] F. London, *Superfluids*, John Wiley and sons, New York, 1950, p.152

[123] John Clarke and Alex I.Braginski, *The Squid Handbook*, Wiley-Vch, 2004. pp. 43-44.

[124] B. S. Deaver and W. M. Fairbank, "Experimental Evidence for quantized flux in Superconducting Cylinders," *Phys. Rev.Lett.*, vol. 7, 1961, pp. 43-46.

REFERENCES (Continued)

[125] R. Doll and M. Näbauer, “Experimental proof of Magnetic flux quantization in a Superconducting Ring," *Phys. Rev. Lett*. , vol. 7, 1961, pp. 51-52.

[126] J. Bardeen, L. N. Cooper and J. R. Schrieffer, “Theory of Superconductivity,” *Phy. Rev*. vol. 108, 1957, pp. 1175-1204.